Force moyenne et fluctuations subies par un obstacle indéformable soumis à l'écoulement confiné d'un milieu granulaire

François Kneib

Communauté
UNIVERSITÉ Grenoble Alpes

THÈSE

pour obtenir le grade de

DOCTEUR DE L'UNIVERSITÉ GRENOBLE ALPES

Spécialité 2MGE : Matériaux, Mécanique, Génie-civil, Électrochimie

Arrêté ministériel : 25 mai 2016

Présentée par

François KNEIB

Thèse dirigée par **Thierry FAUG**, chargé de recherches, IRSTEA, et **Frédéric DUFOUR**, professeur, Grenoble INP

préparée au sein du laboratoire **IRSTEA de Grenoble**, dans l'école doctorale **I-MEP2 : Ingénierie - Matériaux, Mécanique, Énergétique, Procédés, Production**

Force moyenne et fluctuations subies par un obstacle indéformable soumis à l'écoulement confiné d'un milieu granulaire

Mean force and fluctuations experienced by a non-deformable obstacle subjected to the flow of a confined granular material

Thèse soutenue publiquement le **2 juin 2017**,

devant le jury composé de :

Monsieur Farhang RADJAI

Directeur de Recherche, Université de Montpellier, Rapporteur

Monsieur Philippe GONDRET

Professeur, Université Paris-Sud, Rapporteur et Président

Madame Evelyne KOLB

Maître de conférences, Université Pierre-et-Marie-Curie, Examinatrice

Monsieur Émilien AZÉMA

Maître de conférences, Université de Montpellier, Examinateur

Monsieur Thierry FAUG

Chargé de Recherche, Irstea, Co-directeur de thèse

Monsieur Frédéric DUFOUR

Professeur, Grenoble INP, Co-directeur de thèse

Monsieur Mohamed NAAIM

Directeur de recherche, Irstea, Co-encadrant de thèse

Remerciements

Je souhaite tout d'abord remercier mes directeurs de thèse pour leur accompagnement et leur soutien tout au long de ces trois années. Merci à Thierry Faug pour sa proximité et sa disponibilité malgré notre distance géographique pendant les dix-huit premiers mois. Son ambition et son ouverture d'esprit m'ont permis de trouver mon chemin lors de ces recherches, sans jamais nuire à mon autonomie. Merci à Frédéric Dufour de m'avoir fait partager sa grande expérience et de m'avoir aidé à prendre du recul à de nombreuses occasions. Merci également à Mohamed Naaim, encadrant de ma thèse, d'avoir cru malgré moi en mes capacités avant même le début de ces travaux.
Je vous suis reconnaissant à tous les trois d'avoir tout mis en œuvre pour que je puisse découvrir l'Australie en seconde année de thèse. En plus des rencontres enrichissantes à la School of Civil Engineering de l'Université de Sydney, le voyage fut inoubliable.

Je tiens également à exprimer ma gratitude aux membres du jury pour l'intérêt qu'ils ont porté à mon travail de thèse. Merci à Philippe Gondret et Farhang Radjai qui ont accepté de se prêter à l'importante tâche de rapporteur, et aussi à Évelyne Kolb et Émilien Azéma pour avoir participé au jury. Leurs remarques sur mes travaux et les nombreux échanges que nous avons eus à l'issue de ma présentation ont été très enrichissants.

J'ai eu l'occasion de faire de nombreuses rencontres durant ces trois années de thèse. Alors que certaines se sont révélées déterminantes dans l'issue de mes travaux, d'autres ont été enrichissantes d'un point de vue personnel.
Merci en particulier à Gilles Nicolet qui m'a accompagné dans ma découverte du domaine des statistiques, n'hésitant jamais à prendre de son temps pour m'aider. Camarades dès les premiers jours, notre collaboration et notre cohabitation m'a été fortement utile et agréable. Avec ton calme légendaire et ton sens de l'humour, tu as su être mon allier au quotidien et dans les moments difficiles. Merci également à Nicolas Eckert pour son œil expert de statisticien ainsi qu'à Guillaume Chambon pour son soutien et ses compétences sur le comportement des fluides complexes. Merci à Bruno Chareyre et Emanuele Catalano, car les outils qu'ils ont développés avant ma thèse on été le support à bon nombre de mes résultats de thèse.
J'ai également une pensée pour mes camarades de pause, indispensables à mon équilibre par le sentiment d'évasion qu'ils m'ont procuré. Merci donc aux « caillouteux » de l'équipe

PIER : Franck, Fred (grand gourou), Jean-Baba, David, Sylvain, J2M, Jérôme... Merci à Mélanie pour la bonne humeur que tu as disséminée dans notre bureau mais aussi pour tes légendaires gâteaux gourmands.
Enfin, merci à Fred Ousset dont la place dans ces remerciements ne peut être qu'à la transition entre mes camarades de boulot et mes amis. Ton esprit de jeune homme t'aidera — j'en suis sûr — dans les grands changements qui t'attendent pour l'année 2018, et j'espère que nos expériences de modélistes amateurs n'en seront que renforcées.

Merci à mes amis qui, parfois même sans s'en rendre tout à fait compte, m'ont soutenu pendant ces années en s'intéressant à mes travaux, mais surtout par tous les moments divertissants qu'ils m'ont procuré. Je pense à toute la « bande de Knäkes » et en particulier à mes acolytes Luc et Geoffrey. Merci également à Camille et Tudal nos chers Minimoys, sans oublier Damien le colonel ni William la panthère.
Merci à ma famille : mes parents qui m'ont permis d'arriver jusque là, mes sœurs Estelle et Marie, ainsi que Patrick et Nicole. Isabelle, Damien, Annabelle, Boris, merci pour vos encouragements sans faille, pour la « pensée » que vous avez eue pour moi le 2 juin qui m'a aidée — j'en suis convaincu, à obtenir de « Beaunes » remarques le jour J.

J'ai choisi de garder cette place de choix en conclusion de mes remerciements à celles qui me sont les plus chères, Noémie et Anne-Sophie. Noémie, même si certains détails de ce manuscrit t'échappent encore, sache que tu m'as donné beaucoup de courage dans sa rédaction en m'aidant à relativiser tous mes soucis et m'offrant un nouveau rôle à responsabilités : celui de papa. Ton arrivée a été un grand bonheur que nous ne sommes pas prêts d'oublier. Anne-Sophie, je te remercie pour tes sacrifices sans lesquels l'aventure de la thèse n'aurait pas même pu commencer. Merci aussi pour ton soutien quotidien, moteur de ma persévérance ; pour tes conseils, m'apportant confiance en moi ; et pour ton réconfort, renforçant ma motivation dans les moments de doute. Enfin, merci pour la joie que tu m'a procurée pendant ces trois années, et pour les années à venir.

Résumé

Les études existantes s'intéressant au dimensionnement des structures paravalanches s'appuient généralement sur des signaux de force lissés dans le temps. Cependant, le caractère hétérogène de la neige en écoulement est responsable de fortes fluctuations systématiquement observées. Cette thèse a pour objectif de caractériser les fluctuations de force exercées sur un obstacle surversé par un écoulement granulaire. Des modélisations numériques par la méthode des éléments discrets sont mises en œuvre pour simuler l'interaction entre la neige, représentée par un ensemble plan de particules sphériques, et un mur immobile et indéformable. Une particularité de ce travail réside dans l'étude d'une gamme très large de régimes d'écoulement, de quasistatique à collisionnel. Deux systèmes modèles sont développés dans le but de focaliser la zone d'étude en amont de l'obstacle, et de permettre le contrôle des variables macroscopiques de l'écoulement (vitesse de cisaillement, pression de confinement, tailles des systèmes). Le premier confine les grains entre quatre parois dont l'une impose un cisaillement à vitesse constante, alors que les signaux de force sont mesurés sur la paroi faisant face au cisaillement. Le second système confine les grains entre deux parois (dont une cisaillante) et une condition aux limites périodique dans la direction du cisaillement, alors que le mur est immergé dans les grains. Chaque système est étudié via une analyse moyenne puis les fluctuations sont caractérisées à partir des signaux de force instantanés.

Le nombre inertiel macroscopique construit sur la vitesse de cisaillement et la pression de confinement imposées au système s'avère être une variable de contrôle à la fois de la dynamique moyenne et des fluctuations dans les deux systèmes. Une loi empirique a été établie pour chacun des systèmes pour prédire la transmission de force moyenne sur l'obstacle en fonction du nombre inertiel macroscopique, et la mesure de grandeurs locales a révélé que la loi rhéologique $\mu(I)$ des milieux granulaires en écoulement est respectée quasiment partout. Les autocorrélations des signaux de force sur le mur à l'échelle mésoscopique ont révélé l'existence d'un effet mémoire des systèmes aux faibles nombres inertiels, disparaissant avec la transition vers le régime dense inertiel. Les distributions de forces à trois échelles spatiales différentes sont également contrôlées par le nombre inertiel macroscopique : aux régimes lents les distributions sont resserrées et approchent une forme Gaussienne, aux régimes rapides les distributions sont exponentielles. Des lois de probabilité log-normales tronquées à trois paramètres ont été établies afin de prédire de façon empirique les distributions de force sur l'obstacle.

Ce travail contribue à approfondir les connaissances sur la composante moyenne et les fluctuations de force subies par un obstacle soumis à un écoulement granulaire. Les résultats obtenus permettent d'envisager la modélisation de systèmes gravitaires s'approchant des conditions réelles d'écoulements, permettant ainsi la comparaison avec des expérimentations de laboratoire dans le but de mieux dimensionner les structures de génie-civil.

Mots clés : écoulement granulaire, obstacle, force, méthodes des éléments discrets, fluctuations, autocorrélation, distribution.

Abstract

The existing studies dealing with the design of civil-engineering structures against snow avalanches are generally based on force times series that are smoothed over time. However the strong heterogeneity of snow leads to systematic observations of a high level of force fluctuations. This PhD thesis aims at characterizing the force fluctuations exerted on an obstacle that is overflowed by a granular flow. Numerical simulations based on the discrete elements method are implemented to model the interaction between the snow, represented by an assembly of spherical particles, and a rigid motionless wall-like obstacle. A key feature of this work is the broad range of flow regimes investigated, from quasistatic to collisionnal. Two model systems are studied in order to focus on a zone restricted to the upstream of the obstacle, and to allow a full control of the macroscopic flow variables (shearing velocity, confinement pressure, system sizes). The first one confines the grains between four walls from which the top one imposes a constant shearing velocity while the force signals are measured on the wall facing the corresponding displacement. The second system confines the grains between a static bottom wall, a shearing top wall, and a periodic boundary condition in the shear direction, while the wall-like obstacle is fully immersed in the grains. Each system is studied through a time-averaged analysis then the fluctuations are characterized from the instantaneous force time series.

The macroscopic inertial number built from the shear velocity and the confinement pressure imposed to the system turns out to be the main control variable of both the mean dynamics and the fluctuations in the systems. An empirical law has been established to predict the mean force transmission on the obstacle as a function of the macroscopic inertial number for each of the two systems, and the measurement of local strain and stress tensors revealed that the granular flow $\mu(I)$-rheological law is respected nearly everywhere in the samples. The autocorrelations of force signals on the obstacle at the mesoscopic scale revealed the presence of a memory effect of both systems at low inertial numbers which vanishes with the transition from the quasistatic to the dense inertial flow regimes. The force distributions at three different spatial scales are also controlled by the macroscopic inertial number : for slow regimes the distributions are tightened and resemble Gaussian shapes, for fast regimes the distributions are rather exponential. Truncated log-normal probability density functions (with three parameters) have been established in order to predict empirically the force distributions on the obstacle.

This work contributes to advance the knowledge on both the time-averaged and the fluctuating components of the force exerted on a wall subjected to a granular flow. The results enable to look forward with the modeling of gravity-driven systems approaching real flow conditions, thus allowing a comparison with laboratory experiments and full-scale measurements, with the aim of better designing of civil engineering structures impacted by avalanches.

Keywords : granular flow, obstacle, force, discrete elements method, fluctuations, autocorrelation, distribution.

Table des matières

Chapitre 1

Introduction

1.1 Contexte

1.1.1 Avalanches de neige et ouvrages de protection

Avalanches : déclenchement et écoulement

Une avalanche neigeuse est définie comme une masse de neige qui se décroche puis s'écoule le long d'un versant montagneux. La masse de neige est soumise à la pesanteur—qui joue le rôle de force motrice, contre balancée par le frottement basal. La définition de trois phases correspondant à trois zones permet de décrire le déroulement d'une avalanche (Cf. Fig. 1.1).

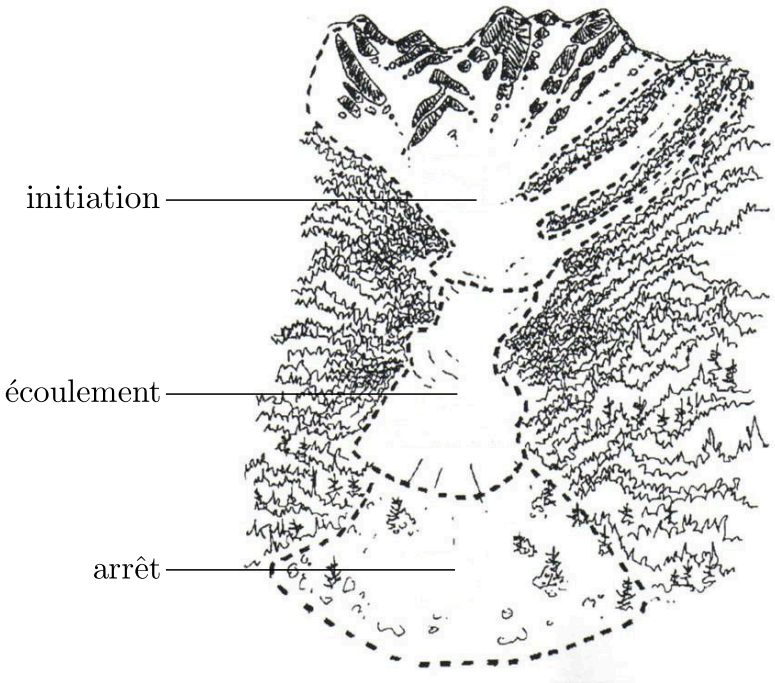

FIGURE 1.1 – Les trois phases de l'écoulement d'une avalanche : initiation, écoulement, arrêt (© 2014 Canadian Avalanche Center).

L'initiation du phénomène est appelé déclenchement, et s'explique par la rupture mécanique d'un équilibre dans le manteau neigeux. Cette rupture qui a lieu dans la zone de départ peut être due à une condition climatique particulière (perte de cohésion du manteau par réchauffement) ainsi qu'à une surcharge mécanique naturelle (animal, chute de corniche) ou artificielle (déclenchement préventif).

La phase de propagation correspond à l'écoulement de la masse de neige le long de la pente. La topographie, les conditions météorologiques, le type de neige formant le manteau sont autant de facteurs qui influencent grandement le phénomène de propagation. Il existe une classification différenciant les types d'avalanches selon les modes d'écoulements observables et la composition de la neige (voir Fig. 1.2).

FIGURE 1.2 – Deux types d'écoulements d'avalanches : en aérosol à gauche (©ANENA), dense à droite (photo Alain Duclos).

— L'avalanche en aérosol : c'est un nuage de neige sèche et froide, formé de particules de glace en suspension dans l'air, pouvant atteindre des vitesses de l'ordre de 100 $m.s^{-1}$.

— L'avalanche dense : la cohésion de la neige permet son aggrégation en grains de taille variable. Ces écoulements ont tendance à suivre le relief par la ligne de plus forte pente, et leur forte densité peut causer des dégâts importants, malgré des vitesses parfois faibles. Si la teneur en eau liquide est faible, le comportement peut être reproduit par un matériau granulaire sec (c'est l'objet de cette thèse, voir partie 1.1.2), mais si elle est forte le mélange est hétérogène et les modèles issus de l'hydraulique torrentielle sont plus adaptés.

— L'avalanche mixte : c'est la combinaison simultanée d'une avalanche en aérosol et d'une avalanche granulaire ou dense.

La phase d'arrêt de l'avalanche se produit lorsqu'elle rencontre un obstacle ou une pente moyenne suffisamment faible. Elle décélère puis s'arrête totalement, formant une zone de dépôt inerte.

Dispositifs de protection et dimensionnement

Face aux dangers pour la population que représentent les avalanches de neige en milieu alpin, deux types d'ouvrages de protection permanents sont mis en place :

— les ouvrages de défense actifs (voir Fig. 1.3), ils interviennent en amont de l'avalanche, en évitant le déclenchement : claies paravalanches, râteliers, filets, reboisements ...

— les ouvrages de défense passifs (voir Fig. 1.4), ils sont bâtis en aval de la zone de déclenchement pour dévier, freiner ou arrêter les avalanches pendant la propagation : étraves, digues ou murs d'arrêt, dents déflectrices, tunnels ...

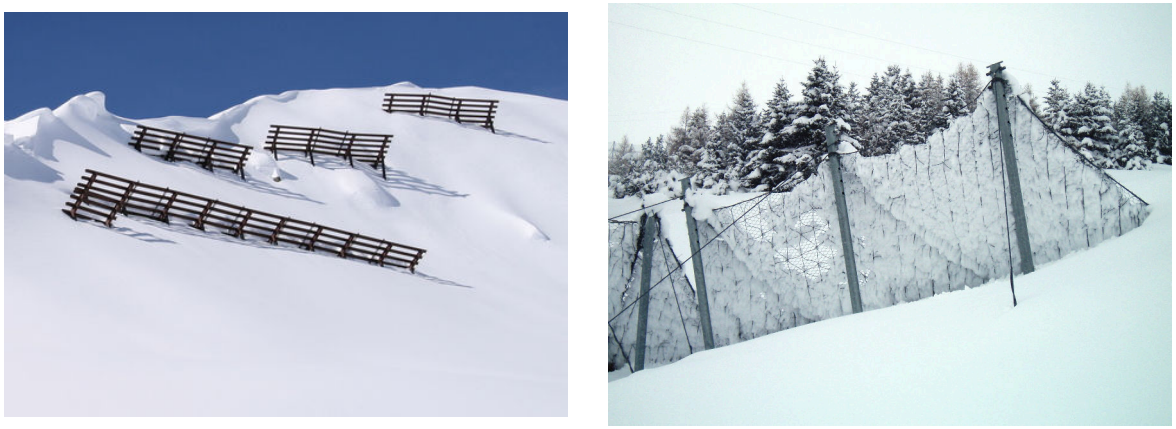

FIGURE 1.3 – Protections paravalanches actives : claie à gauche (photo Böhringer Friedrich), filet à droite (photo Irstea).

FIGURE 1.4 – Protections passives : mur d'arrêt à gauche (Bleie, Ullensvang, Norvège), tunnel ferroviaire à droite (©SMJ).

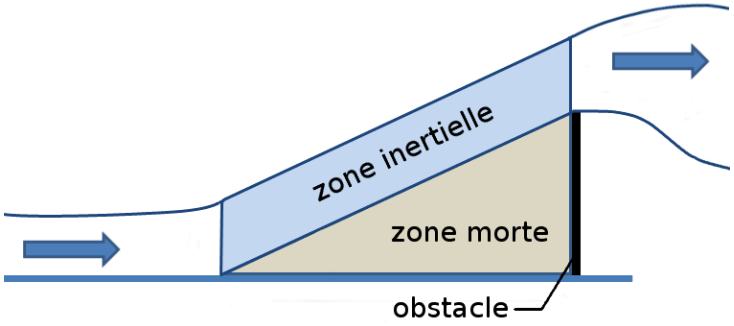

FIGURE 1.5 – Représentation schématique d'une avalanche surversant un obstacle, identifications des zones (image Chanut [21]).

L'objet de cette thèse concerne les ouvrages de protection passifs, et plus généralement l'interaction entre une avalanche en écoulement—lent ou rapide, et un obstacle (voir Fig. 1.5). Dans ce type de configuration, une partie de la neige se retrouve bloquée en amont de l'obstacle, formant une zone quasistatique appelée zone morte. L'obstacle perçoit alors par contact direct la force provenant du poids de la zone morte. En fonction des échelles mises en jeu lors de l'événement (volume de neige, hauteur de l'obstacle), l'ensemble zone morte - obstacle est susceptible d'être débordé par de la neige en écoulement plus ou moins rapide : on parle de zone inertielle. L'obstacle subit également la force dynamique provenant de la zone inertielle par transmission (et éventuellement altération) via la zone morte. Le système ainsi décrit implique la coexistence entre deux zones définies par un matériau identique mais des conditions d'écoulement différents. Une transition spatiale aux propriétés mécaniques complexes a lieu au sein de la neige entre l'état inerte et l'état d'écoulement. Cette transition est à l'origine de fluctuations de force sur l'obstacle d'amplitude et de fréquence élevées, tel qu'exposés dans la partie 1.1.3.

La caractérisation de la force subie par les structures passives de génie civil soumises aux avalanches est un élément majeur lors de leur dimensionnement. Elle passe par l'étude de deux types de données complémentaires. Le premier type est le résultat de lissages temporels, permettant le dimensionnement en terme de force moyenne, maximale et résiduelle, facilitant l'étude des avalanches malgré leur propriété transitoire. Le second type de données résulte des signaux bruts qui comportent des informations temporelles à échelles de temps courtes et permettent d'obtenir des informations sur les fluctuations de force sur l'ouvrage. Il intervient dans l'analyse du phénomène de résonance mécanique survenant à la fréquence propre des structures, élément critique lors du dimensionnement. C'est sur ce second type de données instantanées que porte cette étude.

1.1.2 Écoulements granulaires secs

Les avalanches de neige sont des événements dangereux et souvent rapides qui ont lieu dans des environnements hostiles et instables. Pour ces raisons, l'acquisition de données de terrain à l'échelle d'un versant ou même d'un couloir est très délicate. Afin d'observer ces phénomènes dans des conditions reproductibles et contrôlées et à des échelles acceptables, des expérimentations en laboratoire d'écoulements sur plans inclinés sont souvent réalisés par analogie aux écoulements in-situ. Dans ce contexte, le choix du matériau modèle est un point important qui nécessite une étude de terrain pour obtenir des informations sur la constitution de la neige en écoulement. Cette section vise à montrer que, comme souvent utilisés dans la littérature (voir [31, 85, 71, 70]), les écoulements granulaires secs sont adaptés à la modélisation des écoulements de neige dense sèche.

De la neige aux grains

Les zones de dépôt formées à la fin des événements avalancheux sont des terrains propices à l'étude du matériau qu'est la neige en écoulement. Elles sont en effet situées dans des zones plus facile d'accès, et présentent l'avantage de pouvoir être analysées a posteriori, réduisant ainsi considérablement la contrainte opérationnelle. De plus, par opposition au manteau neigeux avant l'avalanche, le matériau étudié est celui qui s'est réellement écoulé, susceptible d'avoir été transformé par l'écoulement lui-même.

La figure 1.6 montre quatre dépôts formés par des avalanches denses, constitués d'agrégats de différentes géométries. En fonction de la composition de la neige et des conditions d'écoulement, leurs formes peuvent être très angulaires, se rapprochant de polyèdres (voir (a)) ou plus arrondies voire quasi-sphériques (voir (b,c,d)). Dans ce cas, c'est l'érosion efficace par frottement inter-grains qui a tendance à les arrondir lors de l'écoulement. À l'origine, ce sont ces observations d'agrégats quasi-sphériques qui ont conduit la communauté scientifique à considérer les avalanches comme des écoulements granulaires. Ce constat a motivé une analyse réalisée dans [6], qui vise à quantifier la distribution des tailles de ces agrégats pour deux avalanches de neige sèche et deux avalanches de neige humide. Les agrégats sont le résultat de zones fortement cisaillées au sein de l'avalanche, la dynamique de l'écoulement a donc une forte influence sur leur formation.

L'assimilation des avalanches à des écoulement de grains secs a fait l'objet de validations récentes en se basant sur des mesures variées. En 1999, Pouliquen [77] a établi une loi entre épaisseur de dépôt et pente à partir d'écoulements de billes de verre dans un modèle réduit de canal. Cette loi est notamment basée sur l'existence de deux angles critiques θ_{min} et θ_{max}, qui correspondent respectivement aux pentes en-dessous de laquelle aucun écoulement n'est possible et au-dessus de laquelle aucun dépôt n'est laissé après le passage des grains. En 2008, Rognon et al. [83] ont confirmé l'existence de ces angles critiques pour la neige grâce à un canal expérimental situé au col du Lac Blanc. Les angles

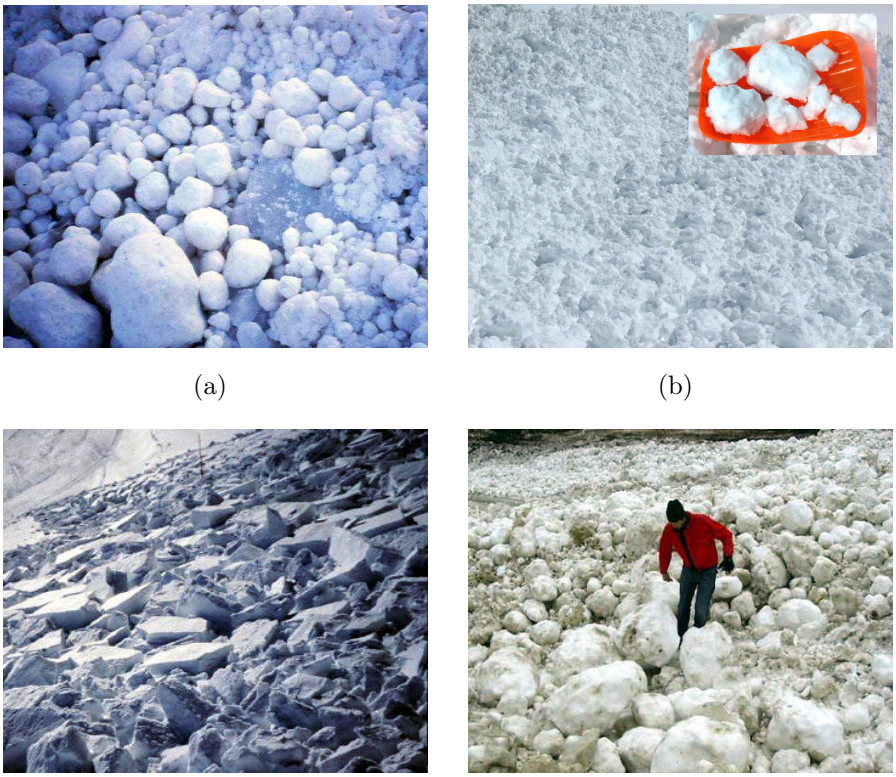

(a) (b)

(c) (d)

FIGURE 1.6 – Exemples de zones de dépôt d'avalanches denses, formation d'agrégats ((a) et (c) : tirées de [3], (b) : ©T. Faug, (d) : tirée de [6]).

obtenus ne sont pas identiques à ceux mentionnés dans [77], mais les différences pourraient être expliquées par les effets de bords qui ne sont pas identiques dans les deux études. Finalement, en 2010, Sovilla et al. [98] ont validé la loi obtenue dans [77] sur des mesures in-situ de pente et d'épaisseur de dépôt d'avalanches prises sur le site expérimental de la Sionne grâce à des données acquises par lidar aérien.

La comparaison des rhéologies des matériaux est un autre axe de comparaison entre avalanches et écoulements granulaires secs. Le cisaillement vertical $\dot{\gamma}$ est une donnée importante dans l'étude des avalanches de neige dense, car couplé à la composante de cisaillement τ du tenseur des contraintes, il permet d'avoir accès à la rhéologie de l'écoulement. Les profils verticaux de vitesse d'écoulement de la neige ont été mesurés sur de multiples dispositifs expérimentaux à échelle réelle (voir [47, 32, 56]) ou sur canal d'écoulement (voir [33, 11, 12, 57, 103, 83, 86]). Un point commun à ces études est la concentration du cisaillement dans une zone proche du fond, alors que les déformations au-dessus de cette zone sont bien plus faibles. Certains modèles permettent de reconstruire ce comportement (voir [33, 73, 72, 74, 31, 57]), et sont quasiment tous basés sur un seuil d'écoulement "artificiel" τ_0 ou un écoulement biphasique. Seule l'étude de P.Rognon prend uniquement en compte le caractère granulaire de l'écoulement (voir [83]) pour expliquer—de manière qualitative—l'existence de deux zones de cisaillement à partir d'une propriété mesurable et intrinsèque à la neige : le diamètre des grains d, non homogène dans la hauteur. En effet, cette étude met en jeu un ensemble bidisperse de grains et établit une relation de proportionnalité entre le cisaillement local et le diamètre local des grains : $\dot{\gamma} \propto 1/d$.

Le présent travail de thèse exploite ces similitudes entre les avalanches denses et les écoulements granulaires, et s'inscrit donc dans le cadre des écoulements de grains rigides, secs et sphériques tels qu'utilisés dans [77]. Le paragraphe suivant résume les résultats existants concernant ce type d'écoulements.

Régimes d'écoulement

Un matériau granulaire est défini comme un ensemble de grains de géométrie et de taille variables qui interagissent. Cette simple définition englobe des domaines d'études nombreux, qui n'ont pourtant de prime abord pas de points communs. Ainsi, l'industrie pharmaceutique, le génie civil, l'agriculture, la géophysique ou encore les chutes de blocs sont autant de domaines concernés par la compréhension de ce matériau complexe. La difficulté principale réside dans le fait qu'aucune loi constitutive universelle ne permet d'établir la rhéologie des milieux granulaires. À contrario, leur comportement dépend des sollicitations extérieures qui lui sont appliqués. Les chercheurs ont donc subdivisé les matériaux granulaires en catégories selon leur mode de sollicitation. Il en résulte trois régimes qui sont définis par la manière dont le milieu granulaire s'écoule (voir Fig. 1.7).

— Le régime quasistatique : les grains ont une inertie quasi nulle qui se traduit par

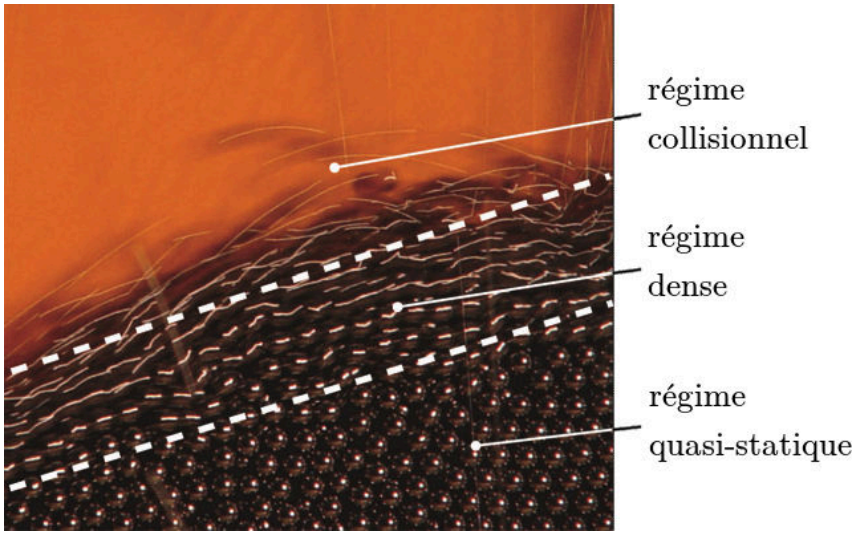

FIGURE 1.7 – Écoulement granulaire, identification des régimes quasistatique, dense et collisionnel (photo issue de [41]).

des contacts frictionnels persistants dans le temps. Les milieux granulaires quasistatiques sont souvent étudiés par les mécaniciens des sols qui utilisent la théorie de la plasticité pour en prévoir le comportement macroscopique (voir [84]).

— Le régime collisionnel : c'est l'opposé du régime quasistatique, les grains ont une inertie très forte qui se traduit par un milieu très agité où les grains sont très éloignés. Comme les temps de contact sont extrêmement courts, assimilables à des contacts binaires, une théorie dérivée de la théorie cinétique des gaz a été établie pour en déduire les équations constitutives (voir [51, 46]).

— Le régime dense : il se situe entre les deux régimes extrêmes, caractérisé par un comportement "liquide". L'inertie commence à avoir de l'influence sur la rhéologie, mais le réseau de contacts entre les grains peut toutefois percoler à travers le milieu de manière transitoire. La majorité des écoulements géophysiques sont concernés par ce régime, mais c'est aussi celui pour lequel l'établissement d'une loi constitutive est le plus difficile. C'est la raison pour laquelle de nombreuses études ont cherché à comprendre ce type d'écoulements complexes ces dernières années.

La recherche dans le monde des milieux granulaires étant caractérisée par un large panel d'applications et donc des systèmes physiques différents, le GDR MiDi a unifié le résultat de plusieurs travaux de recherches dans [44] en 2004. Six configurations bidimensionnelles différentes y sont présentées (voir Fig. 1.8), dont trois confinées et trois à surface libre. Le milieu granulaire (constitué de grains rigides) est cisaillé, soit par gravité, soit par le contrôle en déplacement ou en contrainte d'une paroi, et des mesures sont réalisées aux parois et au sein des grains afin d'extraire les propriétés mécaniques de l'écoulement. Une

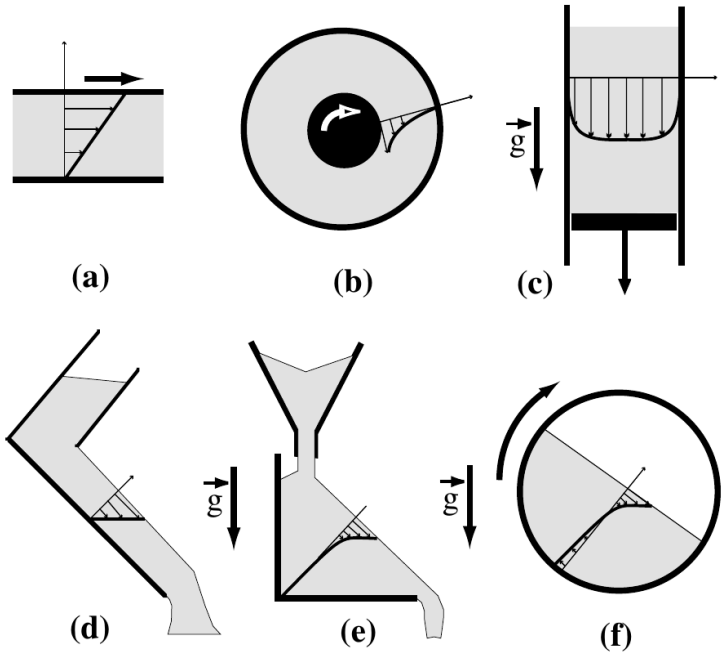

FIGURE 1.8 – Les six configurations d'écoulements granulaires testées par le GDR MiDi : cisaillement plan (a), cisaillement annulaire (b), chute verticale (c), plan incliné (d), entassement (e), tambour tournant (f) (illustration tirée de [44]).

grandeur est définie sur la base d'une analyse dimensionnelle pour quantifier le régime auquel les grains s'écoulent. Cette grandeur, appelée nombre inertiel I, doit refléter les effets antagonistes de la vitesse de cisaillement $\dot{\gamma}$ et de la pression de confinement P. Pour ce faire, deux temps caractéristiques sont définis (voir Fig. 1.9) :

$$T_\gamma = \frac{1}{\dot{\gamma}}, \tag{1.1}$$

le temps typique correspondant à la déformation par cisaillement, et

$$T_P = d\sqrt{\frac{\rho_p}{P}}, \tag{1.2}$$

le temps typique de confinement correspondant au réarrangement (à la relaxation) d'un grain sous la pression P (ρ_p est la masse volumique des grains). Le nombre inertiel I, grandeur adimensionnelle, est le rapport de ces deux temps :

$$I = \frac{T_P}{T_\gamma} = \frac{\dot{\gamma} d}{\sqrt{P/\rho_p}}. \tag{1.3}$$

Parmi les configurations étudiées par le GDR MiDi dans [44], le cisaillement plan sans gravité (voir Fig. 1.8(a)) met en valeur un comportement intéressant de l'écoulement vis-à-vis du nombre inertiel, à condition que les propriétés microscopiques des grains soient ordinaires (coefficient de restitution e inférieur à 1 et angle de frottement μ_p non nul).

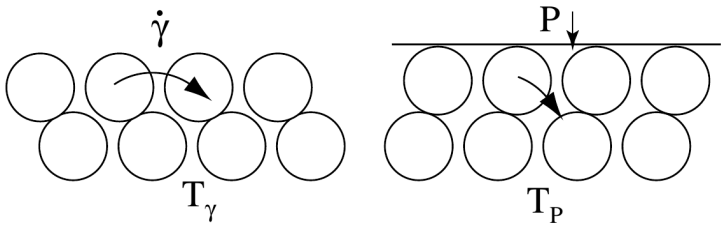

FIGURE 1.9 – Représentation schématique des deux temps caractéristiques, T_γ et T_P (illustration tirée de [44]). T_γ est le temps nécessaire à une couche de grains pour parcourir une distance d par rapport à une autre couche par le cisaillement $\dot{\gamma}$. T_P est le temps nécessaire à une couche de grains pour "retomber" dans une position basse lorsqu'elle a atteint une hauteur maximale en gravissant la couche inférieure.

En particulier, tant que le régime collisionnel (gazeux) n'est pas atteint, les propriétés intrinsèques à l'écoulement du milieu granulaire : vitesses, fraction volumique, frottement effectif $\mu_{eff} = \tau/P$, sont des fonctions univoques de I. Lorsque I est faible, le régime est quasistatique et la réponse du système est indépendante de la vitesse de cisaillement. Lorsque I augmente, le régime dense est atteint et l'inertie entre en jeu : le système devient dépendant à la vitesse de cisaillement. Lorsque I est élevé, l'écoulement est dans l'état collisionnel. I contrôle donc le régime d'écoulement, ce qui signifie qu'il y a deux façons d'effectuer une transition de régime : en modifiant soit la vitesse de cisaillement $\dot{\gamma}$, soit la pression de confinement P.

Ayant trouvé une relation rhéologique $\mu_{eff} = \mu_{eff}(I)$ (dite locale, car en un point donné elle ne dépend que des grandeurs locales) dans cette configuration simple, il est tentant de vouloir l'étendre à des systèmes plus complexes, pour savoir si la rhéologie locale de tout système d'écoulement granulaire répond à cette loi. Mais il s'avère que dans des systèmes plus complexes, la rhéologie en un point donné peut également dépendre de grandeurs qui ne sont pas localisées en ce point. En d'autres termes, il se peut que la rhéologie locale soit perturbée par des grandeurs lointaines, comme la vitesse de l'écoulement en un point géométrique différent, ou encore par des longueurs caractéristiques liées aux conditions au bord du système. Dans ce cas on parle de non-localité, phénomène étudié dans [54, 14].

Enfin, en 2006, Jop *et. al.* ont proposé une formule théorique reliant le coefficient de frottement local μ et le nombre inertiel I valable dans le régime dense, dans le cas où la non-localité n'a pas lieu (voir [52]). Ils établissant alors une loi rhéologique empirique reliant l'inertie de l'écoulement au rapport entre les composantes tangentielle et normale des contraintes appliquées aux grains :

$$\tau/P = \mu(I) = \mu_s + \frac{\mu_2 - \mu_s}{I_0/I + 1}. \tag{1.4}$$

C'est une fonction à double saturation, aux faibles et fortes valeurs de I : μ_s est le

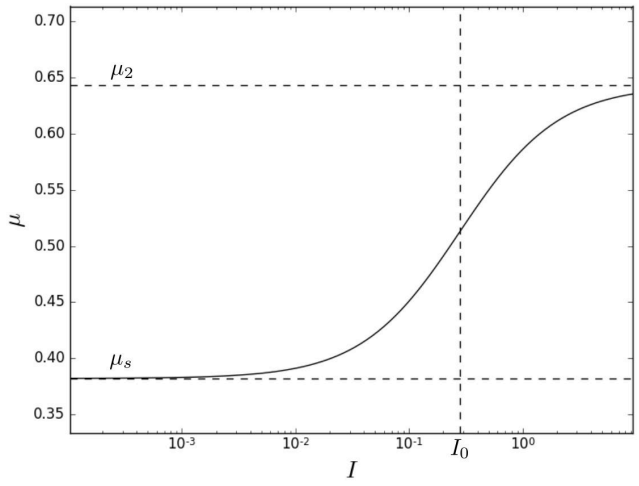

FIGURE 1.10 – La loi rhéologique $\mu(I)$, avec les trois valeurs de paramètres du cisaillement plan donnés dans [52] : $\mu_s = 0.382,\ \mu_2 = 0.643,\ I_0 = 0.279$.

frottement correspondant au seuil d'écoulement (asymptote lorsque $I \to 0$), μ_2 est la valeur de saturation aux grands I, et I_0 est une constante permettant de décaler la fonction par rapport à I (voir Fig. 1.10). Sous condition que les propriétés microscopiques des grains soient ordinaires (voir paragraphes ci-dessus) et que la non localité n'entre pas en jeu, ces trois paramètres ne dépendent que de la configuration géométrique du système (parois, type de sollicitation, dimensionnalité 2D ou 3D).

1.1.3 Interaction avalanche - obstacle : état de l'art

La force exercée par un écoulement granulaire sur un obstacle immergé constitue un domaine d'étude primordial, nécessaire au dimensionnement des structures de génie civil. En plus des ouvrages de protection paravalanches, les bâtiments et pylônes sont également concernés. La norme européenne Eurocodes concernant le risque lié à l'aléa avalanche de neige recommande la prise en compte de la moyenne temporelle de la pression exercée sur l'ouvrage $\langle P \rangle$. De cette façon l'écoulement de neige est vu comme une masse statique pesant sur l'obstacle à dimensionner et des coefficients de sécurité sont utilisés pour prendre en compte les composantes dynamiques.

Cependant, les signaux temporels de pression sur obstacles soumis à des avalanches ont été mesurés et se sont révélés complexes (voir Fig. 1.11). La pression commence par augmenter quasi linéairement dans le temps jusqu'à atteindre un maximum absolu P_{max}. Pendant cette phase de montée en charge correspondant à l'impact de l'avalanche, des maximums locaux de pression P_{peak} sont observés. Par la suite, la pression diminue rapidement avant d'atteindre une valeur de pression moyenne quasiment constante $\langle P \rangle$

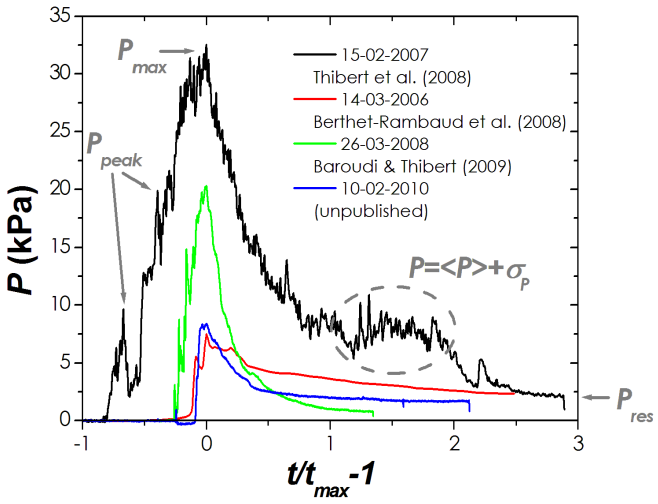

FIGURE 1.11 – Signaux de pression P d'avalanches impactant une plaque carrée de 1m^2 sur le site d'expérimental du Lautaret, en fonction du temps normalisé (t_{max} est le temps auquel le signal de force est maximal).

correspondant à un état permanent de l'écoulement, et perturbée par des fluctuations haute fréquence σ_P. Enfin, lorsque l'écoulement cesse, le dépôt en amont de l'obstacle y applique une pression résiduelle P_{res}.

De tels signaux peuvent—s'ils ne sont pas estimés a priori dans leur intégralité—conduire à l'endommagement ou la destruction des structures immergées. Une meilleure compréhension de l'interaction entre une avalanche et un obstacle est donc nécessaire pour les dimensionnements. Cela passe en particulier par la mise en évidence des liens entre les caractéristiques d'écoulement et les caractéristiques des signaux de force. Cette thèse porte essentiellement sur la compréhension de la composante fluctuante σ_P des signaux de force.

Force moyenne sur l'obstacle

Le calcul analytique complet de la physique des avalanches reste difficile à maîtriser, même en faisant des hypothèses fortes sur leur composition. En effet, les variables d'état au sein de l'écoulement sont à l'heure actuelle non mesurables dans des conditions réelles : les flux de quantité de mouvement et le tenseur des contraintes locaux. Aussi, la rhéologie du matériau, c'est-à-dire la relation locale entre contrainte et déformation ou vitesse de déformation, n'est pas établie de manière universelle (voir partie 1.1.2). Dans ce contexte, des mesures de laboratoire ont toutefois permis d'établir certaines relations entre les propriétés macroscopiques des écoulements granulaires secs en régime permanent et la force moyenne exercée sur un obstacle immergé. En adéquation avec la rhéologie des milieux

granulaires détaillée en partie 1.1.2, il faut distinguer deux régimes : celui où l'inertie est négligeable (régime quasistatique) et celui où l'inertie joue un rôle important.

Lorsque l'inertie de l'écoulement est faible, la pression moyenne sur l'obstacle est proportionnelle à la pression hydrostatique (pression de confinement du milieu granulaire), et la vitesse de l'écoulement n'a pas d'influence. Ce comportement a été vérifié dans plusieurs configurations : écoulement annulaire (voir [2]), écoulement gravitaire vertical (voir [22]), barreau immergé en rotation perpendiculaire à son axe (voir [16]). Pour un système constitué d'un écoulement gravitaire à surface libre rencontrant un obstacle le long d'une pente, la pression moyenne sur l'obstacle peut alors être estimée par (voir [40]) :

$$P_{hydro} = K\rho gh\cos(\theta), \tag{1.5}$$

où θ est la pente en amont de l'obstacle, ρ est la densité moyenne de l'écoulement, g est l'accélération de la pesanteur, h est la hauteur de l'obstacle et K est un coefficient adimensionnel qui dépend de la géométrie du problème et des propriétés du milieu granulaire.

Lorsque la force d'inertie est grande devant la force de pression hydrostatique, les grains sont très espacés et interagissent par des chocs rapides. Le milieu granulaire est collisionnel et peut être vu comme un fluide : la pression moyenne perçue par l'obstacle dépend du carré de la vitesse de l'écoulement. Cette loi, également vérifiée dans diverses configurations (voir [17, 22, 13, 16]), peut alors s'écrire :

$$P_{dyn} = C\frac{1}{2}\rho u^2, \tag{1.6}$$

où u est la vitesse de l'écoulement et C est un coefficient adimensionnel qui dépend de la géométrie du problème et des propriétés de l'écoulement.

Finalement, dans le cas d'étude d'une zone inertielle s'écoulant par-dessus une zone morte en amont de l'obstacle (voir Fig. 1.5), une approche basique consiste à sommer ces deux contributions pour obtenir la pression totale sur l'obstacle (voir [40]) :

$$P = K\rho gh\cos(\theta) + C\frac{1}{2}\rho u^2, \tag{1.7}$$

Hormis le caractère purement permanent de cette description, la limite à cette approche est la forte dépendance de K et C à la taille de l'obstacle, à la hauteur de l'écoulement et aux propriétés mécaniques du milieu granulaire. Ainsi, $K = 1$ est possible pour un écoulement similaire à un écoulement fluide, mais des valeurs supérieures à 10 ont été atteintes sous certaines conditions. C varie généralement entre 1 et 2, et se caractérise par une dépendance à la fraction volumique locale de l'écoulement granulaire et à la forme géométrique de la surface que l'obstacle présente à l'écoulement. Une calibration de ces coefficients en fonction du système étudié est donc souvent nécessaire. De plus, la simple

sommation des deux contributions ne permet pas de prendre en compte l'interaction complexe entre les deux zones d'écoulement. Cela revient à considérer que la zone morte "pèse" simplement sur l'obstacle, et transmet sans altération la force exercée par la zone inertielle.

Récemment, un modèle théorique plus complet a été établi par Chanut et al. [20] et validé expérimentalement par Faug et al. [39] pour mieux apprécier la force exercée par un écoulement granulaire sec à surface libre dans la configuration du mur surversé exposé dans la figure 1.5. Il est basé sur la conservation de la masse et de la quantité de mouvement dans un volume de contrôle correspondant à la zone inertielle surmontant la zone morte. Sa particularité est de prendre en compte la longueur de la zone morte et le caractère transitoire des signaux de pression présentés dans la figure 1.11. La force sur l'obstacle est décomposée en plusieurs contributions :

$$F = F_u^N + F_{h_0} + F_w^N - \overline{\mu}_{zm}\left[F_w^T + F_u^T\right] + F_{mv}, \tag{1.8}$$

où F_u^N est la force due à la déviation de la quantité de mouvement (en régime permanent) entre l'écoulement entrant et l'écoulement sortant, F_{h_0} est la force statique liée à l'écoulement incident, F_w^N est la force correspondant au poids de la zone de contrôle, et $\overline{\mu}_{zm}\left[F_w^T + F_u^T\right]$ est la force de frottement basal sous la zone morte. F_{mv} est la force liée à la variation de la quantité de mouvement à travers le temps pour permettre la prise en compte du caractère transitoire des avalanches. Ce modèle est particulièrement intéressant car ses paramètres d'entrée sont des grandeurs physiques mesurables exprimées en fonction de :

— θ, la pente en amont de l'obstacle,

— θ_{min} et θ_{max}, les angles limites définis dans la partie 1.1.2,

— τ, un temps caractéristique de formation de la zone morte,

— h, la hauteur de l'obstacle,

— h_0/h^*, le rapport entre l'épaisseur de l'écoulement inertiel entrant et l'épaisseur de l'écoulement inertiel au niveau de l'obstacle.

Fluctuations de forces sur l'obstacle

Les fluctuations de force dans les milieux granulaires, composantes notées σ_P dans la figure 1.11, ont fait l'objet d'un bon nombre d'études ces dernières années. Des données in-situ sur le site de la Sionne lors d'événements avalancheux en 1998 et 1999 ont permis d'établir un premier lien entre les propriétés granulaires de l'écoulement (tailles et vitesses des grains) et les fluctuations de force sur obstacle (voir [87]). En parallèle, des expérimentations de laboratoire ont vu le jour pour étudier le comportement fondamental des

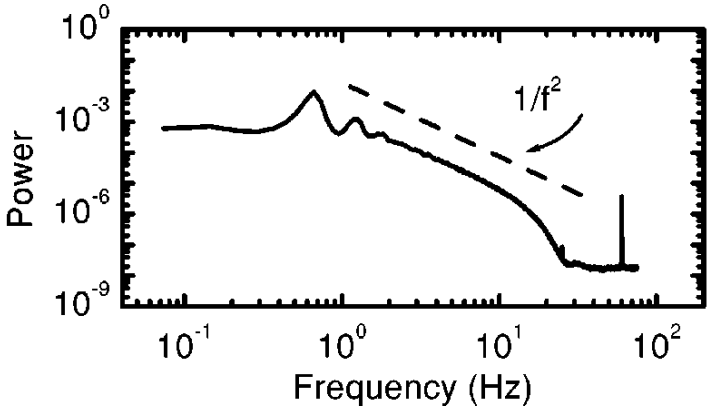

FIGURE 1.12 – Spectre de puissance de la force exercée sur une barre immergée dans un écoulement granulaire cisaillé (graphique issu de [1]).

matériaux granulaires. La majorité d'entre elles mettent en œuvre des écoulements lents et des mesures de force aux parois (voir par exemple [67]) ou sur un élément fixe immergé (voir [1, 45, 26]). Les configurations étudiées sont souvent des cisaillements dans des géométries annulaires de type Couette. Un nombre bien plus restreint d'expérimentations ont été réalisés dans le but d'étudier les fluctuations dans des écoulements granulaires rapides. Dans ce cas, c'est le plus souvent la gravité qui entraîne les grains : décharges de silos équipés de capteurs (voir [62, 42]) ou écoulements à surface libre sur plans inclinés (voir [92]). Dans les écoulements granulaires rapides, l'origine du phénomène de fluctuations est souvent expliqué par des impacts intermittents de particules à haute vitesse. Dans les régimes lents par contre, le système oscille entre des états "bloqués" (dus aux contraintes stériques des milieux granulaires), et des états de relaxation. Le phénomène mis en avant comme responsable des fluctuations est alors le cycle de formation et de rupture du réseau de forces fortes (Radjai et al. [79]).

La réalisation des spectres de forces dans les milieux granulaires a été faite dans la majorité des expérimentations, sur les parois et sur des capteurs fixes immergés. Malgré la variété des systèmes et conditions d'écoulement étudiés, il est saisissant de constater la convergence des spectres vers une loi générique (voir Fig. 1.12). Les spectres sont constants aux faibles fréquences, puis une décroissance en loi puissance d'exposant -2 jusqu'aux plus hautes fréquences est observée. Cette forme de courbe est généralement caractéristique de processus physiques aléatoires, et traduit la complexité et la richesse des phénomènes qui ont lieu à plusieurs échelles dans les matériaux granulaires.

Afin de révéler les propriétés mécaniques des milieux granulaires, les distributions de forces sont souvent utilisées—en particulier dans les études mentionnées ci-dessus. Plusieurs choix sont possibles concernant le type de données relevées et les traitements

qui sont effectués. La grande majorité des études exploitent des distributions purement spatiales, c'est-à-dire que les données sont relevées sur les forces de contact au sein d'un système au repos ou à un temps fini déterminé ("photo" du système). À contrario, ce sont parfois les distributions temporelles qui sont utilisées, ce qui signifie que les échantillons de données proviennent de signaux temporels : le signal d'un capteur de force ou le suivi de la force exercée sur une particule. Dans certains cas les distributions sont obtenues à partir d'échantillons combinant des données spatiales et temporelles, via des moyennes dans le temps ou l'espace. Une revue bibliographique sur le sujet sera détaillée en partie 3.2, mais les principaux résultats extraits de la littérature sur les distributions de forces sont décrits ci-après. On propose ici de distinguer deux modes de mesure :

— les distributions des forces de contact (mesures à l'échelle des grains) dans un premier temps ;

— les distributions de forces intégrées dans l'espace (contribution de plusieurs contacts simultanés) dans un second temps.

Distribution des forces de contact

Les premières analyses de forces de contact dans les milieux granulaires étaient réalisées grâce à du papier carbone placé aux parois du système. Il était possible de remonter aux forces normales en mesurant la taille et l'intensité des traces laissées par les grains (voir [69]). L'utilisation de matériaux photoélastiques (biréfringence induite par contrainte mécanique) et de modélisations numériques a ouvert l'accès aux forces de contact entre les grains au sein du milieu granulaire. Plusieurs études croisées ont démontré que dans le cas statique, les distributions des forces de contact grain-grain sont identiques à celles provenant des forces de contact grain-paroi (voir [95, 96, 80]).

Le comportement des distributions des forces de contact f supérieures à leur valeur moyenne $\overline{f}$ est un résultat robuste, vérifié par de nombreuses études (voir par exemple [61, 81] et Fig. 1.13) : la densité de probabilité décroît exponentiellement jusqu'aux forces les plus élevées. La probabilité relativement forte d'avoir des forces bien supérieures à la force moyenne est généralement associée à la tendance qu'ont les milieux granulaires de transmettre une grande partie des forces le long de structures en chaînes appelées "chaînes de forces fortes" (voir [79]). L'introduction du modèle théorique "q-model" par Liu et al. [61] permet de reproduire ce comportement : chaque grain perçoit les forces en provenance des contacts avec la couche supérieure, et les transmet via une répartition aléatoire aux grains de la couche inférieure. Plusieurs études ont montré la sensibilité de ces distributions à la vitesse de cisaillement (ou au déviateur du tenseur des contraintes pour les systèmes statiques) : l'augmentation de la vitesse de cisaillement du milieu granulaire provoque un élargissement des distributions (voir [62, 96, 45] et Fig. 1.13).

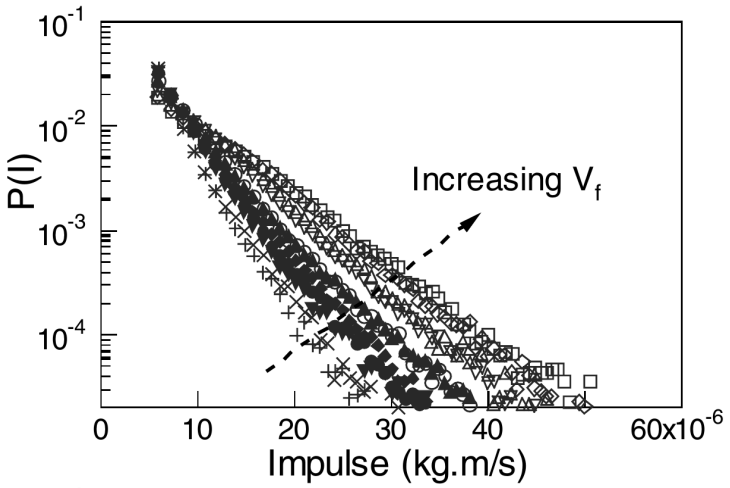

FIGURE 1.13 – Distribution des quantités de mouvement $P(I)$ au bord d'écoulements granulaires. Le capteur, de la taille des grains, est placé sur la surface interne d'un silo se déchargeant à des vitesses V_f différentes (graphique issu de [62]).

Les distributions des forces de contact faibles (inférieures à $\overline{f}$) ont également fait l'objet d'études, mais aucune loi universelle n'a été établie. Cette partie des distributions est en effet très sensible à de nombreux paramètres : la préparation de l'échantillon de grains, la fraction volumique Φ_* au sein du système (liée à l'éventuelle vitesse de cisaillement $\dot{\gamma}$), ou encore l'anisotropie des contacts sont autant de facteurs influents. Ainsi, le comportement exponentiel est parfois continu jusqu'aux faibles forces, mais il est souvent observé à contrario un plateau aux alentours de $\overline{f}$. Dans ce dernier cas, la forme de la courbe pour $f < \overline{f}$ admet un ensemble de possibilités, de la disparition lente au pic de probabilité lorsque $f \to 0$ (voir [4, 96, 104, 78]). À l'heure actuelle, le modèle théorique permettant de prendre en compte cette disparité de la façon la plus complète est décrit par Radjai [78] (voir Fig. 1.14). Basé sur la coexistence et l'interdépendance des réseaux de forces fort et faible (voir [79]), il prend en compte les contraintes stériques des particules et l'aspect aléatoire de la répartition des contacts sur une sphère.

Distribution des forces intégrées dans l'espace

Ce travail de thèse est focalisé sur l'interaction milieu granulaire–obstacle, système dans lequel la force sur l'obstacle est susceptible d'être composée de la contribution simultanée de plusieurs contacts grain–obstacle. Les fluctuations temporelles dans cette situation—pour des écoulements relativement lents—ont été étudiées par un nombre restreint d'études expérimentales, dans des configurations de type Couette (voir [67, 50, 45]) et pour une pale tournante dans un milieu granulaire (voir [97]). Les données sont acquises différemment selon les études, mais systématiquement à des échelles spatiales supérieures à la taille des grains : mesure sur la totalité d'une paroi ou d'un intrus fixe

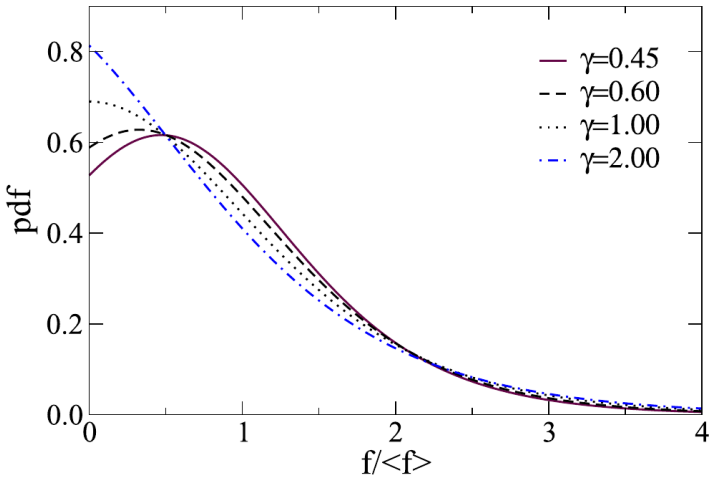

FIGURE 1.14 – Distribution des forces de contact f dans un milieu granulaire statique selon le modèle théorique Radjai [78] (graphique issu de [78]). Le paramètre γ permet de prendre en compte plusieurs comportements lorsque $f < \overline{f}$.

dans [67], [45] et [97] ; mesure des contraintes locales moyennée sur 260 grains du système dans [97]. Un comportement commun des distributions de forces se dégage (voir Fig. 1.15) : en comparaison avec les décroissances exponentielles obtenues à l'échelle des grains, les distributions se resserrent et tendent vers des lois normales à des échelles de mesure plus élevées. Ce résultat est d'autant plus marqué que les écoulements sont lents et s'approchent de l'état quasistatique (forte fraction volumique Φ_*), tandis que l'augmentation de la vitesse provoque l'obtention de distributions de formes log-normales [45] à exponentielles [50].

1.2 Objectifs

En adéquation avec les récents travaux de thèse de Benoît Chanut et Paolo Caccamo (voir [21, 18]), cette thèse vise à étudier l'interaction entre un écoulement granulaire sec le long d'une pente et un obstacle plan orthogonal au déplacement. Les travaux précédents se sont concentrés sur la quantification de la force moyenne subie par l'obstacle, au regard des zones granulaires formées à l'amont : zone stagnante triangulaire surversée par une zone en écoulement dynamique. Cependant, les signaux de force sont systématiquement composés d'une forte composante fluctuante restée inexplorée, notée σ_P dans la figure 1.11.

Les fluctuations de force que subissent les structures soumises aux écoulements granulaires sont un ingrédient essentiel de leur dimensionnement. Ce travail de thèse a pour objectif d'investiguer le rôle que joue la transition fluide-solide au sein du milieu granulaire dans les fluctuations de force sur un obstacle immergé. Il s'agit de les caractériser

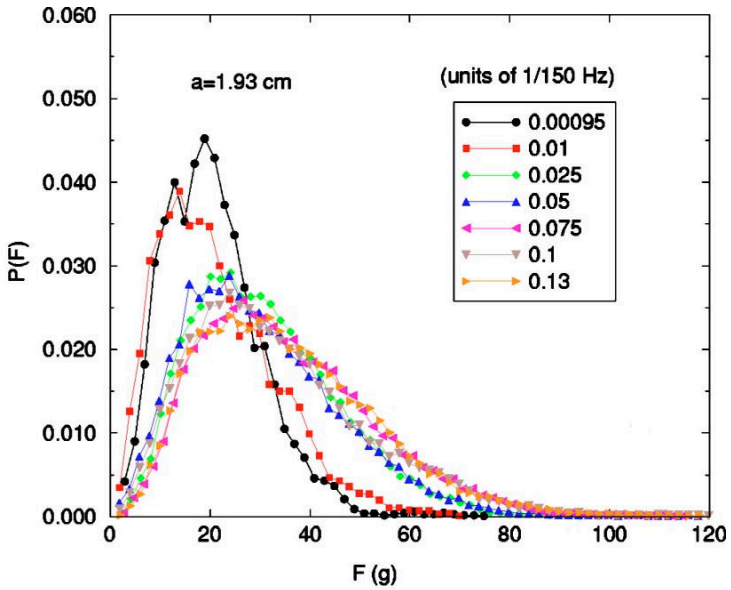

FIGURE 1.15 – Distribution de force exercée sur une particule fixe de diamètre a ($a/d \simeq 2.6$) immergée dans un milieu granulaire en écoulement (expérimentation bidimensionnelle, graphique issu de [45]). Les différentes courbes correspondent à différentes vitesses de cisaillement.

vis-à-vis de paramètres physiques macroscopiques choisis afin de couvrir une gamme très large de régimes d'écoulements permanents : de quasistatique à collisionnel. Différentes échelles spatiales sont considérées dans cette étude : de l'échelle des grains à l'échelle de l'obstacle entier, en passant par une échelle intermédiaire mésoscopique (quelques grains).

Des systèmes modèles mettant en œuvre l'interaction entre un écoulement granulaire et un obstacle plan sont imaginés et modélisés informatiquement par la méthode des éléments discrets. Afin de trouver un équilibre entre rapidité des calculs et représentativité physique, les systèmes sont restreints à des configurations simples en régime permanent sans gravité, correspondant à des zones géométriques en amont de l'obstacle aussi réduites que possible. L'usage de la méthode des éléments discrets permet de prendre en compte l'aspect granulaire du milieu à modéliser, sous des conditions aux limites particulières. Elle s'avère également avantageuse pour acquérir des données complètes, que ce soit aux parois ou au sein du milieu granulaire.

1.3 Méthode

1.3.1 La méthode des éléments discrets (DEM)

La méthode des éléments discrets, formulée dès 1979 par Cundall et al. [28], est une extension de la dynamique moléculaire. Particulièrement adaptée à la modélisation de milieux granulaires, elle prend en compte la complexité géométrique des interactions mul-

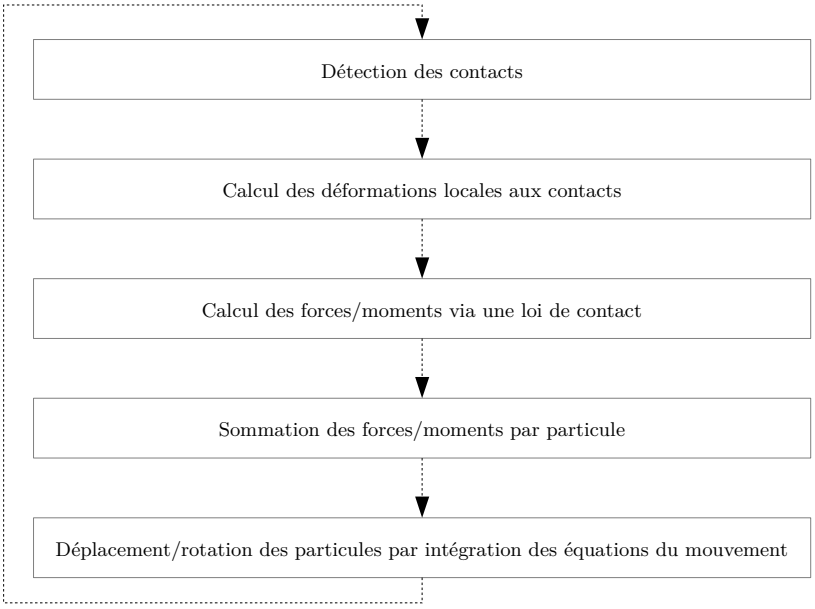

FIGURE 1.16 – Cycle de calcul de la méthode des éléments discrets.

tiples d'un ensemble de particules à l'échelle microscopique. Les particules, supposées localement déformables, sont décrites individuellement par leur position, taille, vitesses de translation et de rotation. Le cycle de calcul est décrit dans la figure 1.16 : à chaque pas de temps, les contacts entre particules sont détectés, puis les déformations normale et tangentielle dans les repères locaux de chaque contact sont calculés. Une loi de contact permet d'en déduire les forces et moments, puis, après sommation par particule, un schéma d'intégration explicite des équations du mouvement est utilisé pour déplacer et appliquer les rotations aux particules. Le schéma numérique est décrit ci-après pour les translations, la formulation est similaire pour les rotations.

Le point de départ est le principe fondamental de la dynamique appliqué à une particule :

$$\ddot{\boldsymbol{x}} = \frac{\sum \boldsymbol{F}}{m}, \tag{1.9}$$

où $\ddot{\boldsymbol{x}}$ et m sont l'accélération et la masse de la particule, et $\sum \boldsymbol{F}$ est la somme des forces de contact qui s'y applique. La discrétisation temporelle suivant la méthode des différences finies centrées à l'ordre 2 permet d'exprimer explicitement l'accélération des particules au temps t en fonction de leurs positions $\boldsymbol{x}$ aux temps $t + dt$, t et $t - dt$:

$$\ddot{\boldsymbol{x}}^t \simeq \frac{\boldsymbol{x}^{t-dt} - 2\boldsymbol{x}^t + \boldsymbol{x}^{t+dt}}{dt^2}, \tag{1.10}$$

d'où :

$$\boldsymbol{x}^{t+dt} \simeq \boldsymbol{x}^t + dt \left(\frac{\boldsymbol{x}^t - \boldsymbol{x}^{t-dt}}{dt} + \ddot{\boldsymbol{x}}^t dt \right). \tag{1.11}$$

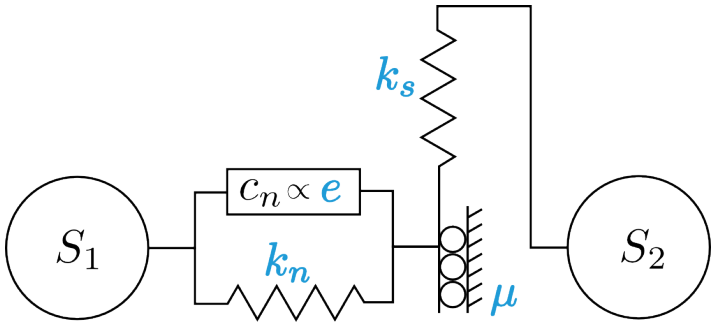

FIGURE 1.17 – Illustration bidimensionnelle de la loi visco-élastique.

Afin de s'affranchir de l'utilisation de $\boldsymbol{x}^{t-dt}$, on approxime la vitesse à $t - \frac{dt}{2}$ par :

$$\dot{\boldsymbol{x}}^{t-\frac{dt}{2}} \simeq \frac{\boldsymbol{x}^t - \boldsymbol{x}^{t-dt}}{dt}, \tag{1.12}$$

et finalement :

$$\boldsymbol{x}^{t+dt} \simeq \boldsymbol{x}^t + dt \left(\dot{\boldsymbol{x}}^{t-\frac{dt}{2}} + \frac{\sum \boldsymbol{F}^t}{m} \right). \tag{1.13}$$

Les positions sont donc connues aux temps $i \cdot dt$ et les vitesses le sont aux temps $i \cdot \frac{dt}{2}$, i étant un entier positif. Le modèle ainsi décrit permet le déroulement de la cinématique des grains en fonction des forces et moments appliqués. Il reste à ajouter la mécanique aux contacts, c'est-à-dire le lien entre déformations locales et forces/moments de contact, et l'ensemble des paramètres associés.

Les expérimentations d'écoulements granulaires en laboratoire sont souvent réalisées à l'aide de billes de verre rigides. Afin de faciliter la correspondance future entre les simulations numériques et d'éventuelles expérimentations, la loi et les paramètres microscopiques sont choisis pour correspondre à ce cas de figure. Une loi de contact visco-élastique est utilisée et illustrée par la figure 1.17 : dans les directions normale et tangentielle au plan de contact, des raideurs k_n et respectivement k_s contrôlent la partie élastique du comportement. L'amortissement normal est piloté par un coefficient de restitution e, et une loi à seuil de frottement μ est utilisée dans la direction tangentielle. Les choix des quatre paramètres, ainsi que la formulation détaillée de la loi seront décrits dans la partie 2.2.1.

Le code de modélisation par la méthode des éléments discrets YADE (voir [105]) est largement utilisé pour ce travail de thèse. Il a l'avantage d'être open-source, permettant ainsi le contrôle, la modification et l'implémentation de fonctionnalités. Il bénéficie de ce fait d'une large communauté d'entraide et de contributeurs, en grande partie constitués de scientifiques.

1.3.2 Systèmes modèles

Le choix de l'utilisation de systèmes modèles simplifiés a été fait pour deux raisons principales.

La première répond à un souci de limitation du temps de calcul, en se focalisant sur une zone restreinte en amont de l'obstacle. De cette façon, il est possible de modéliser finement cette zone en diminuant la taille des particules. Dans le cas d'un écoulement gravitaire, le temps avant établissement de l'état permanent au regard de l'interaction avalanche-obstacle est relativement long. Il faut en effet modéliser le phénomène dans sa totalité, alors que l'initiation de l'écoulement le long de la pente ainsi que la force d'impact pendant l'état transitoire ne font pas partie de cette étude. L'utilisation de systèmes modèles permet d'atteindre bien plus rapidement l'état permanent de l'écoulement, et de ce fait de limiter le temps de calcul.

La seconde motivation à l'utilisation de systèmes simplifiés est la maîtrise des paramètres macroscopiques de l'écoulement comme la pression de confinement et la vitesse. Dans le cas de l'interaction entre un écoulement granulaire et un obstacle, ces paramètres sont fortement dépendants à la pente et alors difficiles à contrôler. En particulier, dans l'étude avancée de Chanut et al. [20] mentionnée en partie 1.1.3, la longueur de la zone morte en amont de l'obstacle est un paramètre primordial mais très sensible à la pente. Pour répondre à cette problématique, les écoulements dans les systèmes choisis ne sont pas induits par la pesanteur, mais par le déplacement de l'une des parois qui contrôle alors le cisaillement et la pression de confinement.

Les deux parties suivantes sont consacrées à la description des deux systèmes modèles étudiés dans cette thèse, à savoir : la cavité granulaire entraînée par cisaillement, puis le mur immergé dans un écoulement granulaire cisaillé. Ils sont tous deux sans gravité, et constitués de sphères et de murs définis dans le même plan. Ils peuvent donc être assimilés à des systèmes bidimensionnels, mais la formulation DEM et les grandeurs physiques sont tridimensionnelles.

La cavité granulaire entraînée par cisaillement

La cavité granulaire entraînée par cisaillement ou LDC (granular Lid-Driven Cavity, voir Fig 1.18) est un système dont les conditions aux limites sont classiquement utilisées dans le domaine de la mécanique des fluides. Un assemblage plan de sphères de hauteur initiale H est déposé par gravité dans une boite à quatre parois. La paroi inférieure de longueur L est immobile et rugueuse, tandis que les parois latérales sont lisses, immobiles, et de hauteur infinie. La paroi supérieure est rugueuse et de longueur infinie. Elle se déplace par translation constante dans la direction x avec une vitesse U positive, appliquant un cisaillement aux grains. La position de cette paroi suivant l'axe vertical y est calculée continuellement par l'algorithme de DEM afin d'appliquer la pression de confinement P au milieu granulaire. Elle repose ainsi sur les grains en leur appliquant une force macroscopique verticale F_c correspondant à la pression macroscopique $P = F_c/Ld$, où d est le diamètre des grains. Il convient de préciser qu'aucun mouvement de rotation n'est autorisé

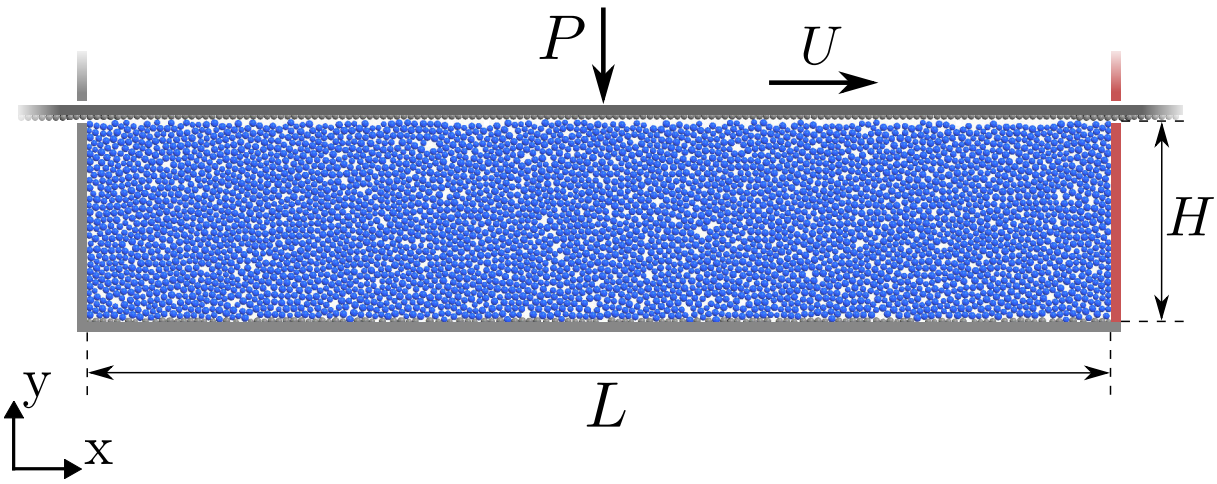

FIGURE 1.18 – Illustration de la cavité granulaire entraînée par cisaillement (LDC). La paroi rouge représente l'obstacle, sur lequel sont faites les mesures.

à la paroi supérieure, et que la pression qu'elle exerce est susceptible de ne pas être homogène le long de l'axe x. Le cisaillement ainsi défini est simulé pour une période (virtuelle) de dix secondes, dont la première est nécessaire pour atteindre le régime permanent alors que l'enregistrement des données est effectué pendant les neuf suivantes.

La correspondance avec la description "zone morte - zone inertielle - obstacle" faite dans les parties précédentes est la suivante : la zone morte est représentée par l'assemblage de grains, qui sont confinés et cisaillés par la paroi supérieure représentant la zone inertielle. Le mur de droite, qui fait face à l'écoulement, est l'obstacle sur lequel les signaux de force F sont enregistrés. La longueur de la zone d'influence de l'obstacle sur l'écoulement, caractérisée par la zone morte dans le modèle de Chanut et al. [20], dépend de la pente dans les systèmes gravitaires et a une forte incidence sur la force subie par l'obstacle. Elle est alors difficile à contrôler et à mesurer, la technique actuellement utilisée reste basée sur un critère de vitesse arbitraire. L'avantage majeur de la cavité granulaire entraînée par cisaillement est la maîtrise de la taille de la zone d'influence, imposée par construction avec l'introduction de la longueur du système L. Il est à noter aussi que les grandeurs macroscopiques de contrôle : U, P et L, sont ajustables explicitement pour permettre d'étudier directement leur impact sur l'interaction écoulement granulaire – obstacle. Cependant, ce système ne permet pas aux grains de surverser l'obstacle, c'est-à-dire de transiter de la zone morte à la zone inertielle. Il est de ce fait susceptible de souffrir d'un phénomène de blocage des grains dans le coin supérieur droit de la cavité, l'éloignant potentiellement de l'application finale.

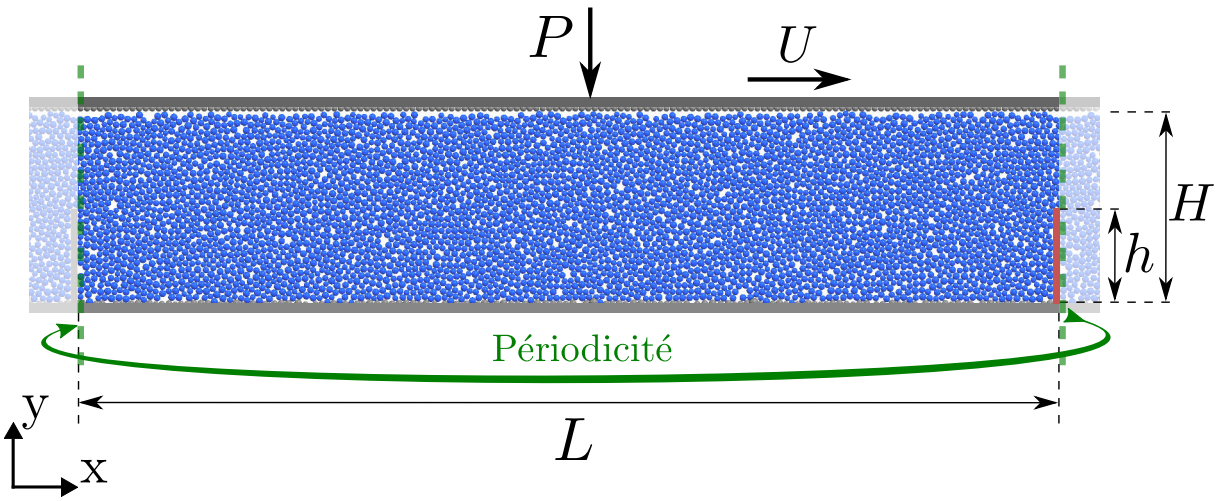

FIGURE 1.19 – Illustration du mur immergé dans un écoulement granulaire entraîné par cisaillement (IW). La paroi rouge représente l'obstacle, sur lequel sont faites les mesures.

Le mur immergé dans un écoulement granulaire entraîné par cisaillement

Le mur immergé dans un écoulement granulaire entraîné par cisaillement, IW (Immersed Wall, voir Fig 1.19) est un système original, imaginé pour correspondre spécifiquement à l'étude des fluctuations dans l'interaction avalanche-obstacle. Il peut être vu comme une généralisation de la LDC à des obstacles dont la hauteur h n'est pas infinie, mais inférieure à la hauteur des grains ($h < H$). Les conditions aux limites supérieure et inférieure sont identiques à la LDC : paroi inférieure rugueuse et immobile, paroi supérieure rugueuse imposant la vitesse de cisaillement $U > 0$ et la pression de confinement P par translations suivant les axes respectifs x et y. La hauteur initiale des grains est H, la longueur du système est L, et un mur vertical de hauteur h est immergé dans le milieu granulaire. Le système dispose d'une condition aux limites périodique suivant l'axe x, ce qui signifie que les grains qui surversent le mur vertical sont de fait réinsérés dans la simulation, à l'extrémité opposée (voir annotations vertes dans la figure 1.19). Comme pour la LDC, le cisaillement dure dix secondes, dont la première est destinée à l'atteinte du régime permanent.

Dans ce système, la définition de la zone morte et de la zone inertielle n'est pas prédéfinie car les grains sont autorisés à transiter naturellement d'une zone à l'autre. La paroi supérieure peut donc être vue comme une condition d'entraînement des grains au sein de la zone inertielle, mais la frontière avec la zone morte se localise librement au sein du milieu granulaire. Contrairement à la LDC, la longueur d'influence de l'obstacle n'est de fait pas imposée, mais ce système a l'avantage de se rapprocher des observations faites sur les écoulements en conditions réelles en autorisant les grains à surverser l'obstacle. En outre, l'utilisation de la condition aux limites périodique permet de garder la souplesse du choix des grandeurs macroscopiques de contrôle : U, P et L, facilitant la comparaison

de ce système avec la LDC.

1.4 Grille de lecture

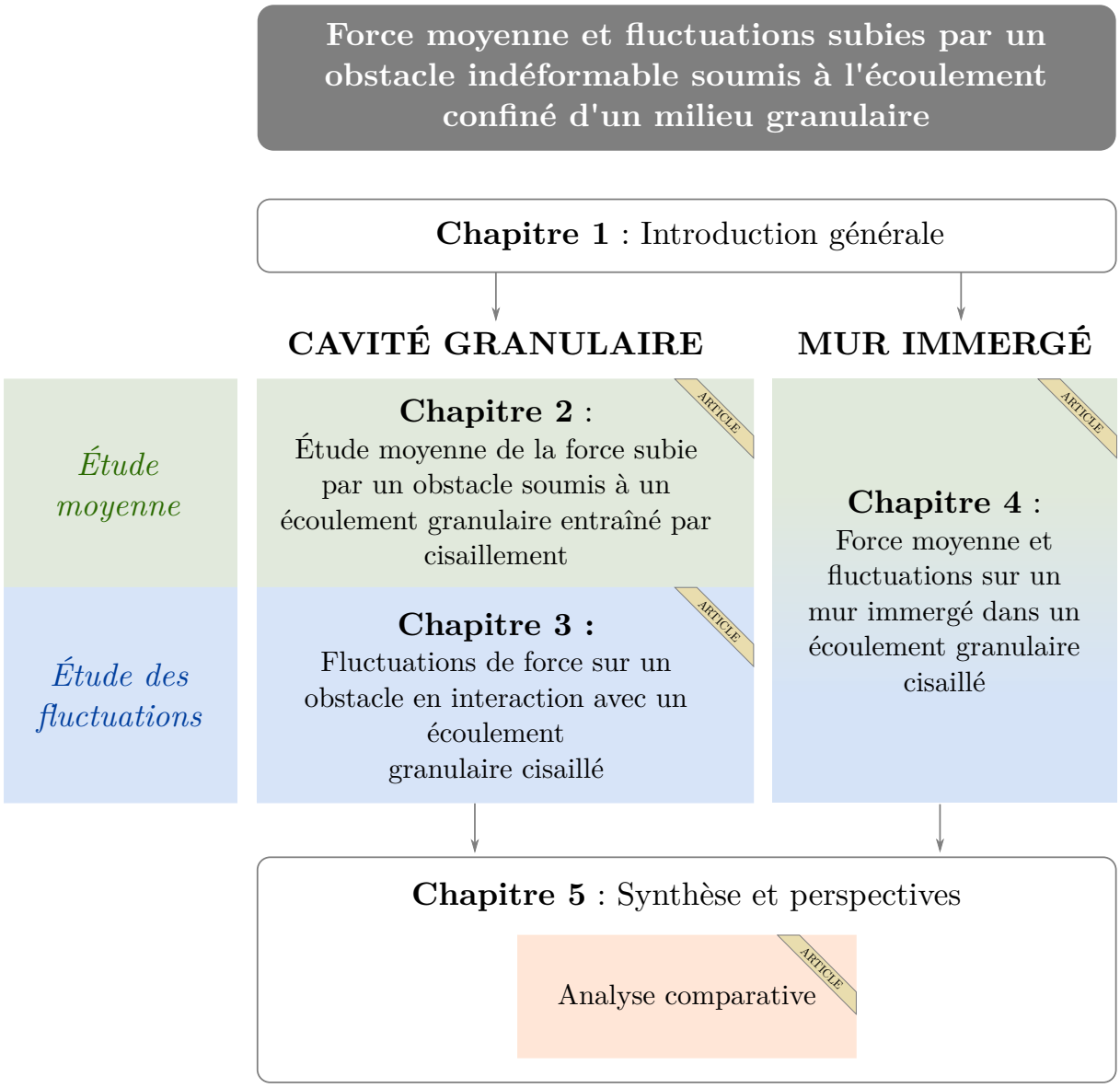

FIGURE 1.20 – Grille de lecture du manuscrit.

Après cette première partie dédiée à l'introduction générale de ce travail, la suite du manuscrit est organisée en 4 chapitres incluant la conclusion (voir aussi Fig. 1.20). Chaque chapitre est constitué d'un article scientifique, et la description suivante permet de les articuler vis-à-vis du contexte général de cette thèse.

— Le chapitre 2 est dédié à l'étude exploratoire de la cavité granulaire entraînée par cisaillement via des grandeurs moyennées dans le temps. Le système ainsi que la

loi de contact et les gammes de paramètres sont décrits de manière détaillée. Les résultats des mesures et leur réponse à la variation des paramètres macroscopiques d'écoulement sont présentés et discutés : lignes de courant, profils spatiaux de forces aux parois, force moyenne sur l'obstacle. La définition d'un nombre inertiel macroscopique I_M, qui reflète les effets antagonistes de la vitesse et de la pression macroscopiques, permet de définir une expression pour la force moyenne exercée sur l'obstacle. Une étude de sensibilité de cette loi aux paramètres microscopiques est également exposée.

— Le chapitre 3 s'intéresse principalement aux fluctuations de forces sur l'obstacle dans le même système. Une brève description du système qui reprend les éléments du chapitre 2 est proposée, et les résultats moyens sont complétés par une analyse de la rhéologie locale. Les fluctuations sont d'abord analysées via des autocorrélations de signaux à l'échelle mésoscopique qui donnent des informations sur la périodicité et la mémoire du système. Les distributions de signaux de forces à trois échelles sont ensuite introduites, et leur comportement vis-à-vis du nombre inertiel I_M est décrit. Dans ce chapitre, les limites de la géométrie de la cavité vis-à-vis des fluctuations sont mises en avant, annonçant la nécessité d'étudier un système différent.

— Le chapitre 4 présente le mur immergé dans un écoulement granulaire cisaillé, répondant à la principale limite du système précédent. Hormis l'introduction de la hauteur du mur, les paramètres et la loi de contact sont identiques au système de cavité. Cette partie s'appuie donc sur les outils et résultats des chapitres précédents pour étudier la dynamique moyenne et les fluctuations dans ce nouveau système. Les lignes de courant ainsi que la rhéologie locale sont analysées, et une loi de prédiction de la force moyenne sur l'obstacle en fonction des paramètres macroscopiques est établie. Enfin, ce chapitre s'intéresse aux fluctuations via les autocorrélations et les distributions de signaux de forces aux échelles mésoscopique et macroscopique.

— La conclusion de ce manuscrit fait un rappel des objectifs et de la méthode employée pour y parvenir. Les résultats des chapitres précédents sont ensuite synthétisés en mettant l'accent sur les principaux résultats pour chaque système dans un premier temps, puis en proposant une analyse comparative des deux systèmes dans un second temps. Finalement, certains résultats sont discutés, amenant les perspectives majeures de ce travail de thèse.

Chapitre 2

Étude de la force moyenne subie par un obstacle soumis à un écoulement granulaire cisaillé

Numerical investigations of the force experienced by a wall subject to granular lid-driven flows : regimes and scaling of the mean force.

Kneib F., Faug T., Dufour F., Naaim M.

Article published in *Computational Particles Mechanics*.

Abstract Discrete element simulations are used to model a two-dimensional[1] gravity-free granular sample, which is trapped between two smooth sidewalls and one bottom rough wall while being subject to a constant shearing velocity at the top under a given confinement pressure. This system, inspired by conventional fluid mechanics, is called a granular lid-driven cavity. Attention is firstly paid to the time-averaged dynamics of the grains once a steady-state is reached. Strong spatial heterogeneities associated with a large-scale vortex formed within the whole volume of the lid-driven cavity are observed. The mean steady force on the sidewall opposite to the shearing direction is then investigated in detail for different cavity lengths, shearing velocities and confinement pressures at the top. The ratio of the force on the latter wall to the top confinement pressure force is not constant but depends on both the shearing velocity and the confinement pressure. Above a critical value of the cavity length relative to the wall height and over a wide range of both shearing velocity and top confinement pressure, all data merge into a one-to-one relation between the mean force scaled by the top pressure force and the macroscopic inertial number of the lid-driven cavity. This result reveals the key role played by the inertial rheology of the granular material in the granular force transmission.

2.1 Introduction

The force experienced by obstacles subject to granular flows is of particular interest for several problems, *e.g.* the transport of particles in industrial or agriculture applications [108], the modeling of impact cratering [55], or the design of safe building and protection structures able to withstand the avalanche force [38]. For the latter example, it is now well-established that stagnant (quasistatic) zones, namely dead zones, can be formed behind obstacles, while the non trapped grains can continue to flow around the obstacle [39]. In those specific configurations, a kind of shear band may appear at the interface between the dead zone and the flowing zone. Up to now, for the particular situation of rigid walls

[1]The two-dimensional system mentionned here was modeled by a perfectly planar assembly of tree-dimensional objects : the grains are modeled by spheres and the walls are modeled by cuboid shapes. As such, their positions coordinates in the z-axis component is fixed to 0, and the rotations of the spheres are only allowed through the z-axis.

normal to incoming free surface flows, a great attention has been paid to the mean (time-averaged) force on the obstacle. Some successful analytical solutions have been developed to predict the time-averaged force on the wall, while accounting for the presence of the dead zone, in either steady [40] or unsteady [20, 39] regimes. One main finding is that the apparent weight of the fluid volume disturbed by the wall (influence zone upstream of the wall), which includes both the dead zone and the overflowing layer of grains, greatly contributes to the total force [40, 20, 39, 38]. The apparent weight is the difference between the weight in the slope direction and the effective friction force. The latter force depends on the rheology of the granular material. The main motivation of the present study is to better understand the role played by the rheological properties of the granular material (through its friction) in the total force experienced by the wall, under a wide range of confinement pressures and shearing velocities imposed by the flow surrounding the dead zone.

A classical geometry in conventional fluid mechanics, namely the lid-driven cavity (see for instance [91] and references therein) is tackled, with the help of two-dimensional[1] (2D) discrete element method (DEM) simulations. Attention is paid to the force experienced by the vertical wall facing the shearing displacement, as a function of the pressure and the shearing speed at the top. Instead of directly studying a flow overflowing a wall (as done in [40, 20]), the lid-driven cavity problem without gravity is considered. This system allows the investigation of the problem of a quasistatic zone in contact with a wall under various flow regimes at reasonable computational times. A wide range of both confinement pressures P and shearing velocities U at the top (mimicking a flowing granular layer above the dead zone) can be studied. Moreover, the size of the granular sample subject to P and U is entirely controlled by the size of the lid-driven cavity itself. Analysing a dead zone formed upstream of a wall down a slope and subject to a wide range of both P and U (imposed by a surrounding flow), with the help of periodic DEM simulations, remains challenging. Firstly, the final length of the dead zone reached in the steady state is unknown and greatly depends on both the wall height and the nature of the incoming flow, which makes the size of the simulated system difficult to predict a priori. In particular, it has been shown in [40] that the length of the dead zone diverges at low slopes. Secondly, it is rather difficult to investigate a wide range of macroscopic inertial number $I_M \propto U/\sqrt{P}$ while the present study on the 2D granular lid-driven cavity allows the range of I_M to span four decades (from $6\,10^{-4}$ to 1.2).

The problem of the force exerted by granular flows impacting obstacles or experienced by objects in motionless granular materials has been tackled in various granular systems : annular flows [108, 2, 1, 45], unidirectional horizontal [17, 106, 13, 99] or vertical [22] flows, objects penetrating in static granular media [55, 89, 90, 15], flows down inclines impacting a wall [40, 20, 39], etc. Rods rotated perpendicular to their axis in a granular bed have been also studied [16, 48]. For rapid (either dense or dilute) flows for which

inertial forces prevail, a velocity-square dependent force is generally found [17, 106, 13, 16]. In contrast, the force is rate-independent when inertia becomes weak [108, 2, 22, 16, 48] and the granular force is described as a frictional phenomenon meaning that the force is proportional to the confinement pressure times the surface of the object. Recent studies have investigated in detail a broad range of parameters for the specific problem of the object penetration in static granular materials [55, 15]. If inertial effects are not dominant (the velocity-square dependent force does not come into play for sufficiently slow flows), a robust scaling verified for several shapes of objects has been found. The force is proportional to the pressure p [15]: $F = \alpha\mu_0 p S_\perp$, where $S_\perp$ is the object surface normal to the flow direction, μ_0 is a constant friction coefficient associated with the granular material at stake and α is a proportionality coefficient which may be much greater than unity. For the penetration problem, $p = \rho g Z$ is the typical hydrostatic pressure associated with the penetration depth Z, where ρ is the bulk density and $g = 9.81\text{m.s}^{-2}$ is the gravity acceleration. A similar scaling was found earlier for rods rotated perpendicular to their axis in a granular bed [16]. The present paper does not deal with the recent results in [49] showing that this classical frictional picture of the granular force may not be valid in some specific systems where the object itself is able to screen the pressure. The present paper demonstrates that the force measured at the wall of a lid-driven cavity is consistent with the traditional frictional scaling, meaning that the force is firstly controlled by the pressure at the top. However, a subtle effect of the rheology of the granular material through imposed U and P will be presented.

The paper is organized as follows. The discrete element method used and the associated contact laws are first described in detail, as well as some important results regarding the time-averaged dynamics of the 2D lid-driven cavity (section 2.2). The time and depth averaged force exerted on the wall which is normal and opposite to the direction of the shear speed is then investigated (section 2.3). Finally, we discuss the main results and further research to be conducted in section 2.4.

2.2 Method and simulated granular system

2.2.1 Discrete element method and contact laws

The Discrete Element Method (DEM) is an extension of the Molecular Dynamics modeling method introduced by Cundall & Strack [28]. It is specifically suited to model granular media as it allows accounting for the multiple interactions between deformable spheres through contact forces. All numerical simulations in this paper were performed with the open-source software YADE-DEM, whose implementation details are available at [105]. At each time step, contact forces are computed from particles relative positions and rotations, and from specific contact laws accounting for the required contact physics.

Then an explicit leapfrog integration of the 2^{nd} Newton's law allows computing the new position and velocity of particles.
A linear visco-elastic normal force model is used with a Coulomb frictional force along the tangential direction. This model is satisfactory for the present study as it can mimick dry contacts regardless to the rate of loading, from a quasistatic regime to a dynamic one (see for instance [27]). The normal component of the interaction force is defined as :

$$\boldsymbol{F_n} = \max(0, k_n\delta_n + c_n\dot{\delta}_n)\boldsymbol{n}, \tag{2.1}$$

where δ_n is the normal interpenetration between the two particles, $\dot{\delta_n}$ the related interpenetration velocity, k_n the contact normal stiffness, c_n the viscous coefficient and $\boldsymbol{n}$ the contact normal unit vector. In accordance with [64], the tangential component of the interaction force is incrementally computed as :

$$\begin{cases} d\boldsymbol{F_s} = (k_s\dot{\delta}_s dt)\boldsymbol{s} \\ |\boldsymbol{F_s}| \leq \mu|\boldsymbol{F_n}| \end{cases} \tag{2.2}$$

where $\dot{\delta_s}$ is the relative tangential velocity at the contact point, k_s the contact tangential stiffness, μ the contact friction coefficient, dt the time-step and $\boldsymbol{s}$ the tangential unit vector associated with the relative tangential displacement. The normal contact stiffness k_n between two particles $\{1, 2\}$ is deduced from their Young modulus $\{E_1, E_2\}$ and their diameters $\{d_1, d_2\}$:

$$k_n = \frac{E_1 d_1 E_2 d_2}{E_1 d_1 + E_2 d_2}. \tag{2.3}$$

The contact tangential stiffness is determined by the particle Poisson's ratios ν_1 and ν_2 :

$$k_s = \frac{\nu_1 E_1 d_1 \nu_2 E_2 d_2}{\nu_1 E_1 d_1 + \nu_2 E_2 d_2}. \tag{2.4}$$

For two identical spheres of diameter d, Young modulus E and Poisson's ratio ν, equations (2.3) and (2.4) reduce to :

$$\begin{aligned} k_n &= \frac{1}{2}Ed, \\ k_s &= \nu k_n. \end{aligned} \tag{2.5}$$

The initial aim is to mimick glass beads behavior, but the real glass Young modulus cannot be used as this would lead to heavy calculation times. It is quite well established that the following dimensionless number should be sufficiently high for the simulations to be in the asymptotic limit of rigid grains :

$$N_0 = \frac{k_n}{P_0 d} = \frac{1}{2}\frac{E}{P_0}, \tag{2.6}$$

where the dimensionless number N_0 compares the normal contact stiffness to a typical pressure P_0 characterizing the granular system at stake (the value chosen for P_0 will be

discussed hereinafter). Keeping E (or k_n) sufficiently large leads to simulations insensitive to its value, at least if the mean (macroscopic) behavior of the granular system is considered. This generally works well with $N_0 = 10^4$, as discussed for instance in [40] and references therein. However, as local peak pressures are likely to reach very high values, the results sensitivity toward the particle stiffness was investigated by increasing N_0 from $1.5\,10^4$ to $6\,10^4$ (see table 2.1).

The contact friction coefficient μ is deduced from the two particle friction coefficients μ_1 and μ_2 :

$$\mu = \min(\mu_1, \mu_2) \tag{2.7}$$

Computing the viscous coefficient c_n from the particle parameters – and especially from the restitution coefficient e – is not trivial. The formulation reported in [88] is used :

$$e = \begin{cases} \exp\left[-\frac{\beta}{\omega}\left(\pi - \arctan\frac{2\beta\omega}{\omega^2-\beta^2}\right)\right] & \text{for } \beta < \frac{\omega_0}{\sqrt{2}}, \\ \exp\left[-\frac{\beta}{\omega}\left(\arctan\frac{-2\beta\omega}{\omega^2-\beta^2}\right)\right] & \text{for } \beta \in \left[\frac{\omega_0}{\sqrt{2}}, \omega_0\right], \\ \exp\left[-\frac{\beta}{\Omega}\ln\frac{\beta+\Omega}{\beta-\Omega}\right] & \text{for } \beta > \omega_0, \end{cases} \tag{2.8}$$

where $\beta = c_n/m_{eff}$, $\omega_0^2 = 2k_n/m_{eff}$, $\omega = \sqrt{\omega_0^2 - \beta^2}$, $\Omega = \sqrt{\beta^2 - \omega_0^2}$ and $1/m_{eff} = 1/m_1 + 1/m_2$. But the reciprocal function of equation (2.8) to get a solution for $c_n(e, k_n, m_{eff})$ does not allow any analytic solution. Thus, the efficient Newton-Raphson method was implemented, which is appropriate as $c_n(e, k_n, m_{eff})$ is a monotonic function. The effect of c_n is analysed on the results according to the values of e reported in table 2.1. In the DEM model, the time-step is chosen with respect to the minimum natural oscillation period amongst all particles (T_{min}). The time-step dt is then automatically set up with a safety factor N_{dt} as :

$$dt = N_{dt} T_{min}. \tag{2.9}$$

The effect of the time-step on the results is studied by modifying N_{dt}, as reported in table 2.1. In accordance with equations (2.3, 2.6, 2.8) and table 2.1, the following ranges of values are used : $k_n \in [6.6\,10^1, 6.6\,10^5]\text{N.m}^{-1}$; $c_n \in [1.3\,10^{-3}, 3.3\,10^{-1}]\text{kg.m.s}^{-1}$.

To avoid crystallization effect, a slight polydispersity is introduced by choosing the grain diameters randomly between $d(1 - d_{disp})$ and $d(1 + d_{disp})$, where d_{disp} is the polydispersity coefficient. Although all results presented in this paper were obtained with $d_{disp} = 0.15$, it has been verified that they are not influenced by a slight variation of the polydispersity coefficient by performing some simulations with $d_{disp} = 0.1$. The particle density ρ_p is chosen according to the glass density, i.e. 2500 kg.m^{-3}.

TABLE 2.1 – All simulation parameters and corresponding values used. RCP = random close packing.

Symbol	Value(s)	Description
d	10^{-3}m	mean grain diameter
d_{disp}	$\{0.1, 0.15\}$	polydispersity coefficient
ρ_p	2500 kg.m^{-3}	grain density
Φ	0.6	estimated RCP (spheres)
e	$\{0.5, 0.75\}$	restitution coefficient
N_0	$\{1.5\,10^4, 3\,10^4, 6\,10^4\}$	stiffness safety factor
μ	$\{0.27, 0.5\}$	friction coefficient
N_{dt}	$\{0.15, 0.3\}$	time-step safety factor
ν	$\{0.3\}$	Poisson's ratio
H	$\{30d\}$	cavity height
L	$0.5H$ to $10H$	cavity length
N_U	1 to 20	shear velocity coefficient
N_P	0.01 to 100	top pressure coefficient

2.2.2 Lid-driven cavity

Geometry and boundaries

The lid-driven cavity is modeled by a planar assembly of spheres trapped in a rectangular gravity-free box (see Fig. 2.1). The box length is L and its height is H. The box height H was kept constant and equal to $30d$ in all simulations discussed in the present paper. The two sidewalls are fixed and smooth while the bottom wall is fixed and rough. The top wall is horizontal, rough and rigid. Its infinite length allows the application of a constant horizontal (shear) velocity U as well as a constant vertical pressure P (through the vertical displacement of the top wall satisfying inertial dynamics). Roughnesses are made by glued grains. The friction coefficient between walls and particles is equal to the inter-particle friction. The imposed vertical pressure P directly defines the typical pressure P_0 used for the limit of rigid grains discussed in section 2.2.1 : $P_0 = P$. As a large range of flow regimes is studied, the two dimensionless numbers N_U and N_P are introduced : $U = N_U\sqrt{gd}$ and $P = N_P\Phi\rho_p gH$. They are convenient to modify the shear velocity and the vertical pressure around some typical values based on the gravity acceleration g, the grain diameter d, the box height H, the particle density ρ_P and a typical volume fraction Φ. Please note that even if the system is gravity-free, N_P is based on a typical pressure which would act in an identical system under gravity.

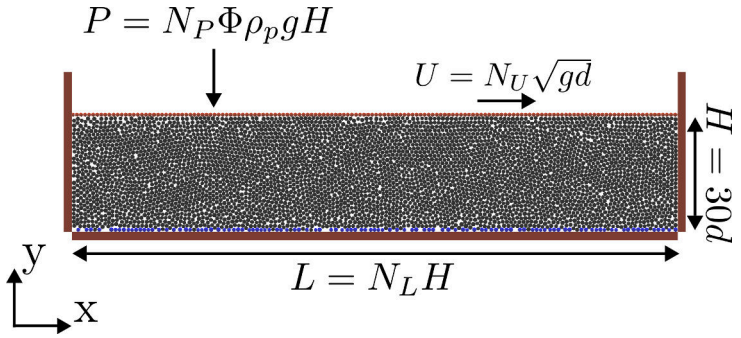

FIGURE 2.1 – Sketch of the 2D granular lid-driven cavity simulated by DEM.

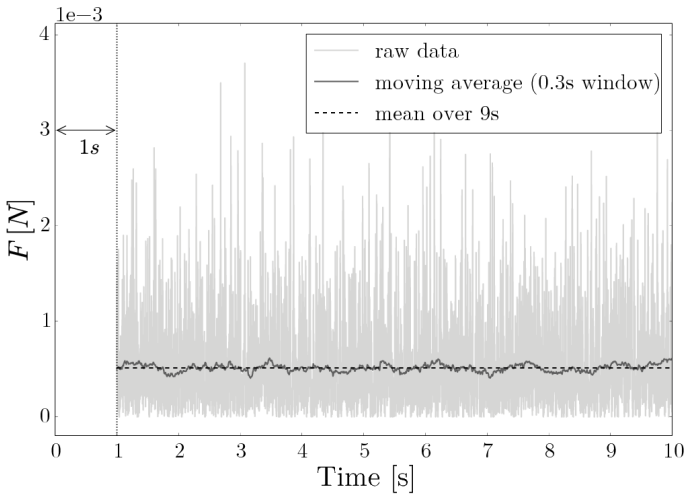

FIGURE 2.2 – Example of time series of space-averaged force on the wall, obtained for $L/H = 5$, $N_U = 10$, $N_P = 0.01$. The instantaneous force F is highly fluctuating over time. The horizontal dashed line depicts the value of the time-averaged force, named $\overline{F}$, reached in the steady-state regime (after a short transient of about 1s).

Steady-state regime

Figure 2.2 displays an example of the total normal force (F) on the wall evolving over time, obtained for $L/H = 5$, $N_U = 1$ and $N_P = 0.01$. The tangential component of the force is much smaller than the normal component for all simulations. The force time series show strong fluctuations. If a moving average is considered (over 0.3 seconds, as shown in Fig. 2.2), a transient regime followed by a steady-state regime is observed. $\overline{F}$ is defined as the mean force experienced by the sidewall facing to the shear velocity averaged over time and across the wall height, which is reached in the steady-state regime. Thus, $\overline{F}$ is independent of the simulation time as soon as the latter is high enough. This mean steady force $\overline{F}$ corresponds to the horizontal dashed line drawn in Fig. 2.2.

The present study is mainly focused on the study of the mean force $\overline{F}$ over a wide range of velocity U and pressure P. However, three important aspects are first investigated

in order to highlight the strong spatial heterogeneities within the box, which are caused by the geometry and boundary conditions associated with the lid-driven cavity problem. The main observations associated with the development of a large-scale vortex within the whole volume of the cavity are reported in the following section.

Large-scale vortex and spatial heterogeneities within the cavity

Firstly, some examples of time-averaged streamlines within the cavity are drawn in Fig. 2.3 for $L/H = 5$ at constant pressure ($N_P = 1$) for two distinct shear velocities ($N_U = \{3, 10\}$). Similarly to classical patterns usually observed with Newtonian fluids flows, a large-scale vortex appears within the whole cavity. In contrast with recent investigations on the formation of mesoscopic and short-life vortice in granular media (see [82] and [68]), the present study focuses on the macroscopic steady vortex whose size is fully controlled by the cavity size. The vertical dashed line highlights the position of the vortex center relative to the box length : the vortex center is almost located at the center of the box at low shear rates, while it is shifted to the right at high shear rates. The horizontal dashed line depicts the position of the vortex center across the cavity height, which remains very close to the upper shearing wall whatever the shear rate. Interestingly, those time-averaged streamlines show that the flow within the cavity ressembles a thick layer of grains undergoing a quasi simple shear (below the vortex center and moving from right to left in Fig. 2.3) surmounted by a very thin and rapid inertial layer (above the vortex center and moving from left to right). The typical thickness of the latter layer is called ϵ (a few grains), while the thickness of the former layer is $H - \epsilon$, as shown in Fig. 2.3. This picture is true over around 75% of the cavity length for $N_U = 3$ and around 40% for $N_U = 10$. In addition to the shearing at the top, the roughness at the bottom might be essential for the vortex center position (we expect that a smoother but still rough bottom would probably increase ϵ).

Secondly, Fig. 2.4 shows the variation of the time-averaged vertical force on the top wall across the cavity length (along the position x). The data were reconstituted from the position and the vertical component of the force of each sphere that compose the top wall. It is worth noting that $\frac{1}{L}\int_0^L \overline{F_n^{top}}(x)dx = PLd$, where P is the pressure imposed at the top. The overlapping curves at constant cavity length exhibit a weak effect of the shear velocity on the top force profile. A strong increase along the cavity length occurs at the top : the profile is exponential and may become more than exponential when approaching the position $x = L$ (sidewall facing the shearing velocity). This kind of singular wedge effect (caused by a very high confinement in the top right corner of the cavity) prevails when the typical length of the wedge reaches the length of the cavity. There might then exist a critical cavity length above which the magnitude of the force experienced by the sidewall facing to the shearing velocity should not be significantly influenced by this wedge

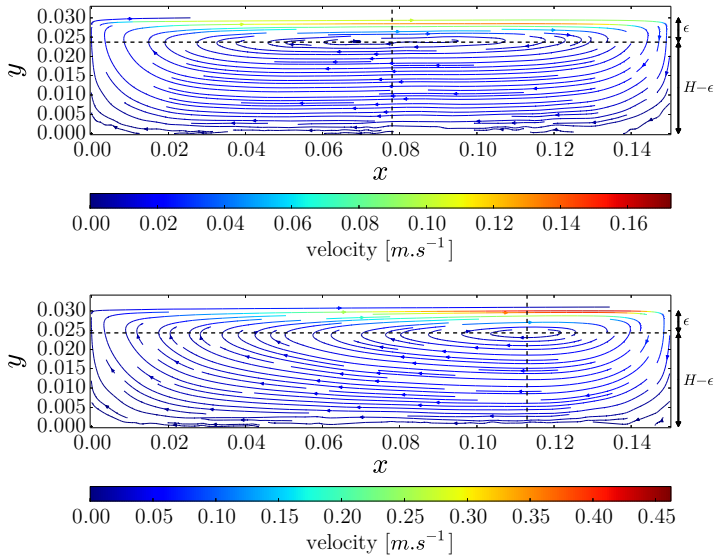

FIGURE 2.3 – Examples of time-averaged streamlines for two shearing velocities : $N_U = 3$ (top) and $N_U = 10$ (bottom), $N_P = 1$ and $L/H = 5$ for both plots. The intersection between the vertical and horizontal dashed lines defines the position of the vortex center.

effect (see discussion in section 2.3.1).

Thirdly, the time-averaged force distribution along the wall height is investigated. Fig. 2.5 shows the normalized pressure variation across the vertical position y, which is experienced by the right sidewall of the cavity. The curves were obtained by segmenting the force measurement along the right wall height into 10 parts of same thickness, in a similar fashion that would stem from data obtained from laboratory tests with 10 force sensors placed along the wall (the surface of each of them filling a tenth of the wall height). The high increase of the force just below the cavity lid confirms the importance of the wedge effect.

No systematic analysis of the time-averaged streamlines, spatial pressure variations at the top and against the wall, as functions of L/H, N_U and N_P is conducted in this paper. However, the results shown in Figs. 2.3, 2.4 and 2.5 clearly evidence the strong spatial heterogeneities occurring within the cavity, which are associated with the large-scale vortex forming inside the whole volume of the cavity. In spite of those strong spatial heterogeneities, the existence of a scaling of $\overline{F}$ is investigated thereinafter.

2.3 Mean force on the sidewall facing to the upper shearing velocity

Forces in slow sheared dense granular media are usually described as a frictional phenomenon, meaning that the forces are proportional to the local confining pressure times the

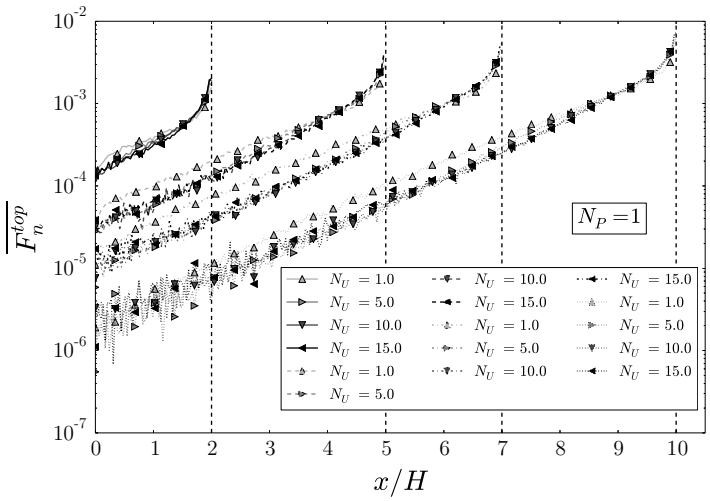

FIGURE 2.4 – Examples of time-averaged pressure variation along the position x at the top of the cavity for different cavity lengths and shear velocities. Cavities lengths are displayed by vertical dashed lines.

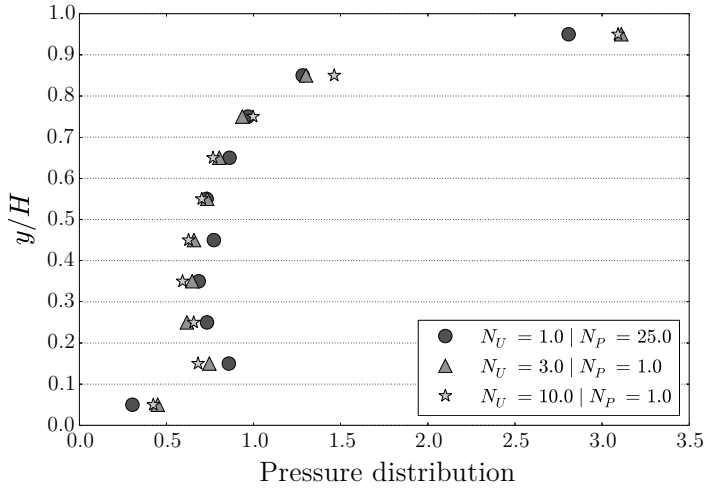

FIGURE 2.5 – Examples of normalized spatial pressure variation across the vertical position y at the right wall of the cavity, for different confinement pressures P and shear velocities U ($L/H = 5$). The wall height is segmented into 10 parts for force measurements.

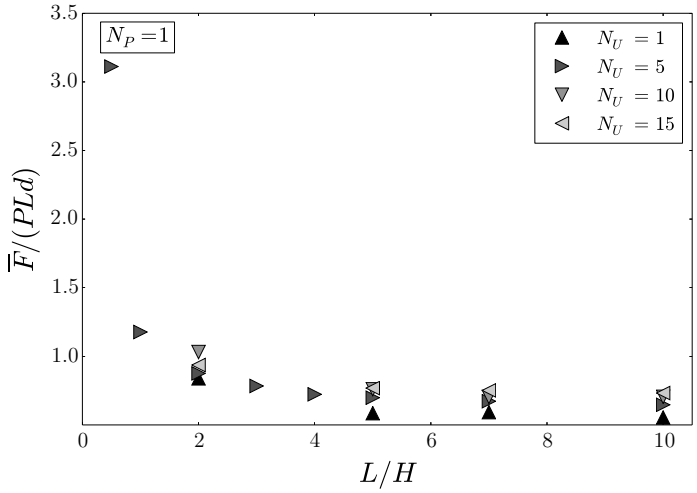

FIGURE 2.6 – Mean force on the right wall relative to the top force, $\overline{F}/(PLd)$, versus the cavity length relative to its height, L/H, for different velocities at constant $N_P = 1$ ($H/d = 30$).

surface of the object (see discussion in the introduction of the paper). The mean force from the top, PLd, should then play a prevailing role in the force transmission from the top toward the sidewall facing to the upper shear velocity. In the following, the effect of L, U and P on the mean force $\overline{F}$ scaled by the top force PLd on the wall is investigated.

2.3.1 Effect of the cavity length

Figure 2.6 shows how the ratio $\overline{F}/(PLd)$ varies with the cavity relative length L/H. This ratio highly depends on L/H at small L/H values, which confirms some influence of the strong spatial heterogeneities observed within the cavity and discussed before in section 2.2.2. However, the ratio $\overline{F}/(PLd)$ becomes only weakly dependent on L/H above a critical value of L/H around $4-5$. Data on the force experienced by the left wall of the cavity, named $\overline{F}_{-}$, are not shown here because the magnitude of this force was found to be much lower than the force $\overline{F}$ on the right wall, once L/H was sufficiently large. The following values are typically obtained : $\overline{F}_{-}/\overline{F} < 0.05 - 0.10$ for L/H above $4-5$, while $\overline{F}_{-}/\overline{F}$ could reach $0.2 - 0.25$ for $L/H = 2$. In order to avoid a prevailing effect of the cavity length while keeping reasonable computational times (large L leads to higher computational times), the results presented in the following of the paper were obtained with a constant cavity length relative to its height, namely $L/H = 5$, unless otherwise specified.

2.3.2 Effect of the macroscopic inertial number

Figure 2.7 shows how the ratio $\overline{F}/(PLd)$ varies with N_U at different values of N_P : $\overline{F}/(PLd)$ undergoes a slow increase with the shear velocity, similarly to the results re-

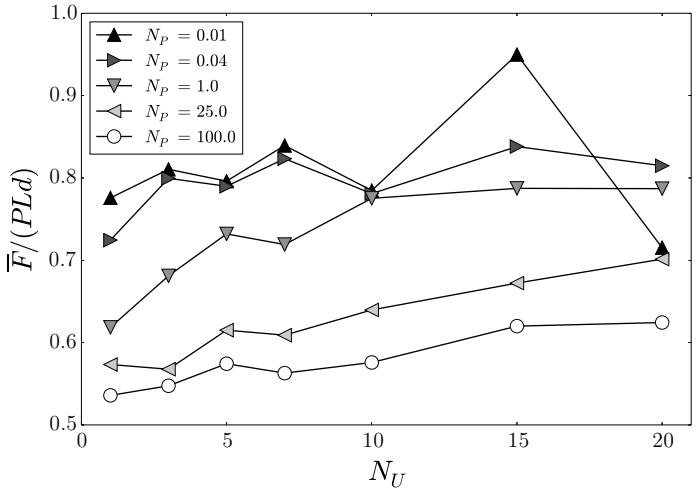

FIGURE 2.7 – Mean force on the wall relative to the top force, $\overline{F}/(PLd)$, versus N_U at different N_P.

ported by [45] for an object moving in a static granular medium in an annular geometry. Note that decreasing P at constant U leads to a substantial increase of $\overline{F}/(PLd)$.

Two conclusions are straightforward from Fig. 2.7. Firstly, the force is rate-dependent, in contrast to rate-independent stresses in purely Mohr-Coulomb friction models. Secondly, it does not correspond to the linear increase of force with the velocity (when the velocity is not too large) for Newtonian fluids in conventional fluid mechanics. The slow increase of $\overline{F}$ with U observed here might be consistent with the $\mu(I)$ inertial rheology proposed by [52] for sheared dense granular materials. It is now well established that flow regimes in sheared dense granular materials are mainly controlled by the inertial number $I = t_\sigma/t_{\dot\gamma}$ (see [44]), which compares the typical time scale of rearrangements under pressure σ, ($t_\sigma = d/\sqrt{\sigma/\rho_P}$), and the macroscopic time scale ($t_{\dot\gamma} = 1/\dot\gamma$) linked to the mean deformation γ ($\dot\gamma$ is the local strain shear rate). The detailed time-averaged mapping of the local inertial number within the whole volume of the cavity is not quantified in this study. This remains a technical challenge regarding data processing because the $I(x,z)-$mapping is likely to be highly heterogeneous with respect to the shape of the streamlines and to pressure variation along x at the top, as shown in section 2.2.2. A direct and much simpler approach is rather adopted by defining the macroscopic inertial number of the lid-driven cavity as the macroscopic shear rate U/H times the macroscopic time scale $t_P = d\sqrt{\rho/P}$ associated with the mean top pressure P :

$$I_M = \frac{U}{H} t_P = \frac{U}{H} d \sqrt{\frac{\rho}{P}}, \tag{2.10}$$

where ρ is taken equal to $\Phi\rho_p$, which corresponds to the mean medium density within the whole cavity (see values in table 2.1). It is important to stress that the present study is focused on how varying U and P affects $\overline{F}/(PLd)$ (H and d were kept constant).

Figure 2.8 depicts the ratio $\overline{F}/(PLd)$ as a function of the macroscopic inertial number I_M. Depending on the set of simulation parameters considered, the top plot in Fig. 2.8 shows some scattering, *i.e.* a slight dispersion of $\overline{F}/(PLd)$ at identical I_M can appear. In the bottom plot of Fig. 2.8, the averaged value of $\overline{F}/(PLd)$ for a given I_M is considered, which allows to obtain a very well-defined curve showing that $\left\langle \overline{F}/(PLd) \right\rangle$ is entirely controlled by the inertial number I_M, whatever the couple (U, P). It is worth noting that some results obtained here with values of L/H different from 5 ($L/H = 7$ or 10) are also included. The latter result means that $\overline{F}$ is not only controlled by P, but the length of the cavity crucially comes into play. Thus, following the traditional granular force on objects discussed in the introduction, the force $\overline{F}$ can also be written : $F = \alpha\mu_0 PHd$, where α would depend on L/H.

Fig. 2.8 also allows to verify that the results are insensitive to the value of k_n because this parameter is not constant but varied with P with respect to the limit of rigid grains (see section 2.2.1).A recent study has investigated in detail the influence of the particles stiffness for steady-state shear granular flows [94]. In particular that study has quantified a critical stiffness below which the softness of the particles plays a significant role in the constitutive laws. In the present study, it is verified that k_n is kept sufficiently high and weakly influences the one-to-one relation between $\overline{F}/(PLd)$ and I_M shown in Fig. 2.8 by testing the values reported in table 2.1. The results are presented in Fig. 2.9, confirming the weak sensitivity to k_n in our simulations. Fig. 2.9 also allows the verification that both e and N_{dt} do not have any influence on the results. However, a strong influence of the particle friction μ was found : decreasing μ from 0.5 to 0.27 led to a systematic and remarkable decrease of $\overline{F}/(PLd)$, whatever the value of I_M (see black crosses in Fig. 2.9). This result highlights that even though the mean force is primarily controlled by P and L, the interparticle friction also comes into play. As a consequence, the bulk shear stress analysis should provide crucial information. This will be done in a future study based on the work of Singh et al. [93], where the shear stress is deduced from the contact forces along the local strain rate eigendirections.

2.3.3 Toward an empirical model for the mean force

The data on Fig. 2.8 can be robustly fitted by the following empirical function ($R^2 \simeq 0.98$) :

$$\frac{\overline{F}}{PLd} = r_1 + \frac{r_2 - r_1}{1 + \frac{I_M^0}{I_M}}, \tag{2.11}$$

where r_1 and r_2 would correspond to asymptotic values of the ratio $\overline{F}/(PLd)$ at low I_M and high I_M, respectively. A fit on data displayed in the bottom plot of Fig. 2.8 (see continuous line) gives $r_1 = 0.53$ and $r_2 = 0.86$. I_M^0 defines the typical inertial number

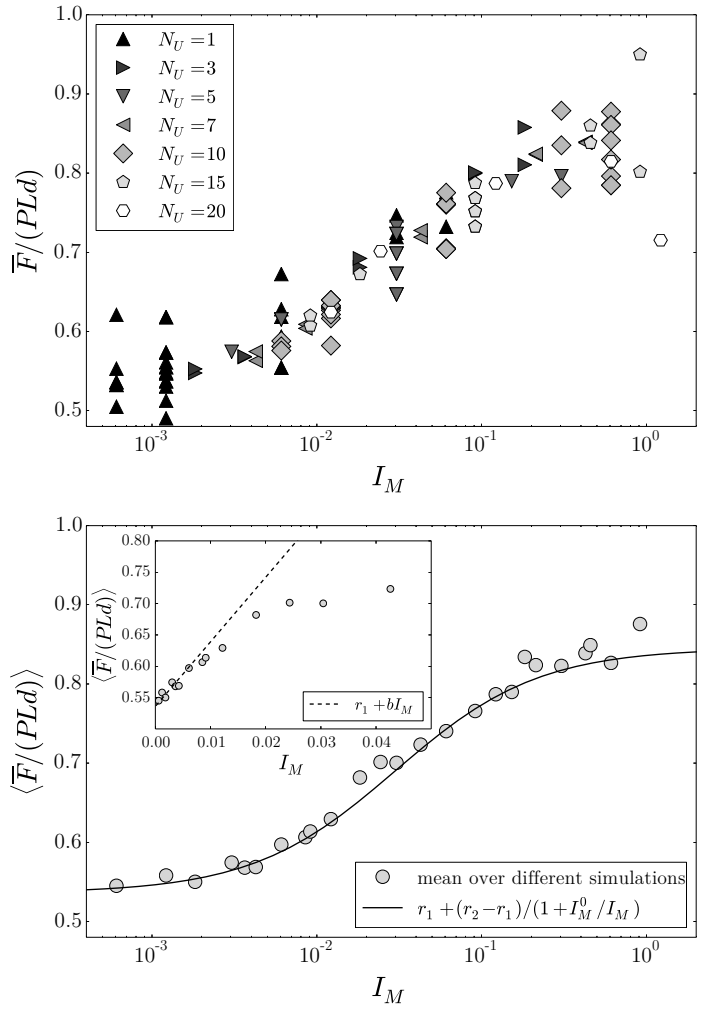

FIGURE 2.8 – Mean force on the wall relative to the top force, $\overline{F}/(PLd)$, versus the macroscopic inertial number I_M. Top plot : raw data corresponding to all simulations conducted at different U and P ($H/d = 30$) ; for a given I_M, some scattering is observed depending on the set of simulation parameters considered. Bottom plot : same data as in the top plot but by considering the averaged value of $\overline{F}/(PLd)$ obtained at identical I_M. The continuous line depicts the fit given by Eq.(2.11) with $r_1 = 0.53$, $r_2 = 0.86$ and $I_M^0 = 0.034$. Inset : same plot with a linear scale and the prediction of the linear equation $r_1 + bI_M$ with $b = (r_2 - r_1)/I_M^0$ (valid for the lowest I_M).

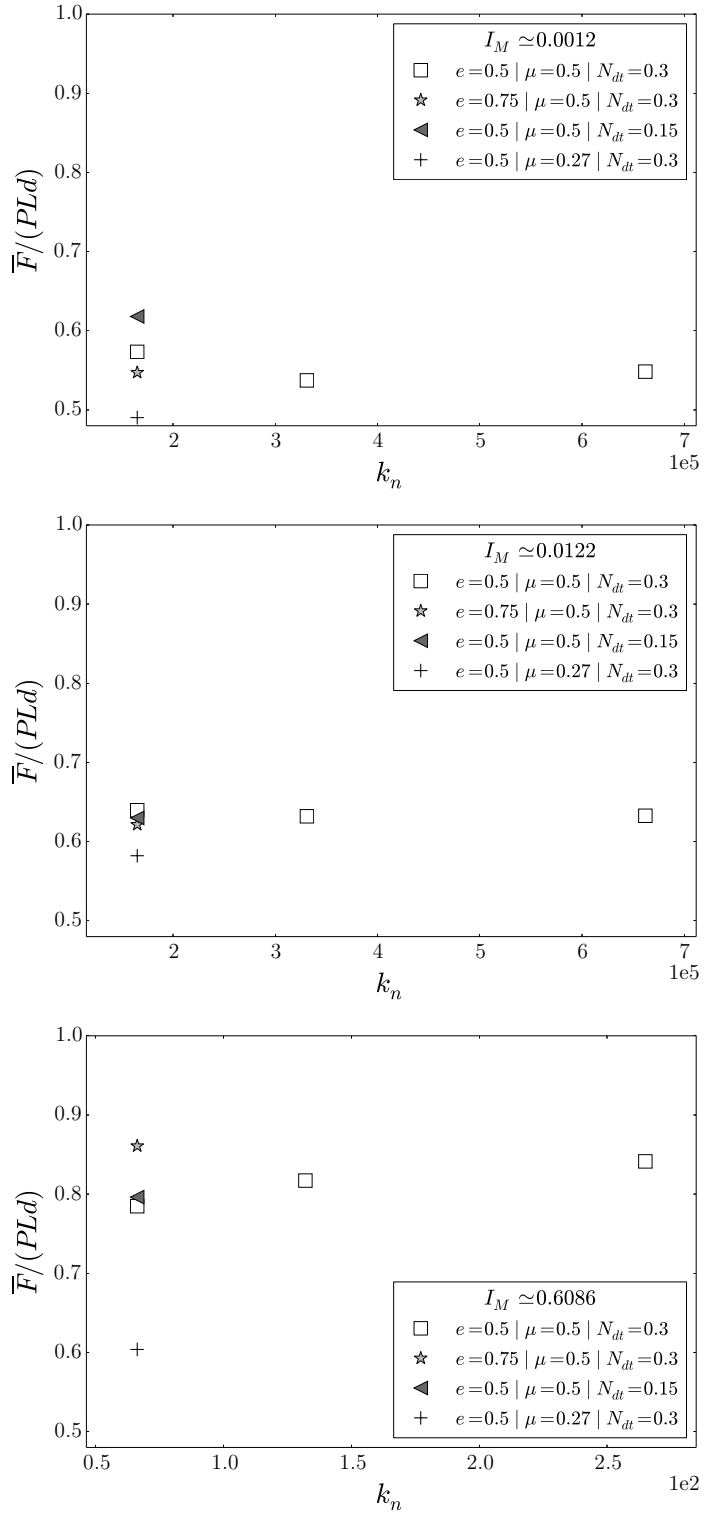

FIGURE 2.9 – Mean force on the wall relative to the top force, $\overline{F}/(PLd)$, versus the normal stiffness k_n for three values of $I_M \simeq 0.0012$ (top), $I_M \simeq 0.0122$ (center) and I_M : $I_M \simeq 0.6086$ (bottom) with different sets of e, μ and N_{dt}.

for which $\overline{F}/(PLd) = (r_1 + r_2)/2$ and is found to be $I_M^0 = 0.034$. For low I_M, Eq. (2.11) reduces to $\overline{F}/(PLd) = r_1 + bI_M$, where $b = (r_2 - r_1)/I_M^0$ (see dashed line in the bottom plot of Fig. 2.8). The cross-comparison between the data and this linear law clearly shows the saturation of $\overline{F}/(PLd)$ at high I_M, which can be captured by Eq.(2.11) with the additional parameter r_2 corresponding to the upper-limiting value of $\overline{F}/(PLd)$. As a conclusion, the force on the right wall is dependent on the three different flow regimes, which are classically characterized by the inertial number I_M : the quasistatic regime at low I_M ($I_M \lesssim 10^{-3}$) for which $\overline{F}/(PLd)$ is constant, the dense inertial regime at intermediate values of I_M ($10^{-3} \lesssim I_M \lesssim 0.3$) for which $\overline{F}/(PLd)$ is a function of I_M and the rapid regime at higher I_M ($I_M \gtrsim 0.3$) for which $\overline{F}/(PLd)$ starts saturating.

It is now well-established that (if non-local effects do not play a role) there exists a one-to-one relation between the inertial number and the bulk friction within the material [52] (enhanced granular rheologies that quantifies the non-local effects introduced in [54] and [14] are not taken into account in this paper). The analogy between the characteristic shape of the data shown in Fig. 2.8, fitted by Eq.(2.11), and the form of the friction law proposed by Jop et al. (see [52]) for dense sheared granular flows is striking. This might confirm the crucial role played by friction, intimately linked to the inertial number, in the force transmission process. Let's assume a $I-$dependent friction force, known to increase when the inertial number increases [52], which is likely to drive the variation of $\overline{F}/(PLd)$. Assuming the collinearity between the stress and strain rate tensors, the latter friction force should (by construction) be oriented from the left to the right in the same direction as the upper shear velocity, so it may produce an increase of $\overline{F}/(PLd)$ with I_M (for the detailed discussion about the non-collinearity, see [107]). Coming back to the shape of the time-averaged streamlines within the cavity associated with the large-scale vortex moving clockwise (Fig. 2.3), the thick bottom layer (of thickness $H - \epsilon$) in quasi simple shear might produce this friction force. In contrast, the friction force stemming from the thin upper layer (of thickness ϵ) is expected to be negligible because the latter layer correspond to a dilute and more inertial flow. The high force experienced by the wall in its upper part (see Fig. 2.5) is more likely to emerge from a purely inertial force in the form $\rho U^2 \epsilon d$. The existence of a thick flow in simple shear opposite to the shearing velocity at the top appears to be consistent with the observation of an increasing $\overline{F}/(PLd)$ with I_M, as observed in Fig. 2.8.

The inertial forces (proportional to U^2) caused by the large-scale vortex moving clockwise do not appear to come into play, meaning that the force is not controlled by the velocity square (within the range of parameters tested in the present study), in contrast to the velocity-square dependent force generally found for rapid granular flows in some other geometries [17, 106, 13]. Eq.(2.11) demonstrates that the force transmission is rather driven by frictional but rate-dependent processes. The force is proportional to the pressure imposed at the top. However, the proportionality coefficient is not constant but

depends on the macroscopic inertial number. This result reveals a new granular regime regarding force transmission process. Further measurements are needed to understand more in detail the role played by the $\mu(I)$ inertial rheology in the force transmission and to possibly develop a model for fully predicting $\overline{F}$, instead of Eq.(2.11) which remains an empirical fit of the numerical data.

2.4 Discussion and conclusion

The present paper described the study of a granular lid-driven cavity with a particular attention paid to the force experienced by the sidewall facing to the shear velocity. Because of the boundary conditions associated with the lid-driven cavity (two fixed sidewalls, one bottom fixed wall and a moving upper wall at velocity U), a large-scale vortex developed inside the whole volume of the cavity and reached a steady-state regime. Strong spatial heterogeneities stem from this vortex-like dead zone. In particular, the force at the top of the cavity increased exponentially from the left to the right (in the direction of the shearing velocity) with the development of wedge zone of high pressure. As a result, the force on the right wall was much higher in the upper part of the wall than in the rest of the wall height. In spite of this strong spatial heterogeneity, the time-averaged force on the wall $\overline{F}$ relative to the mean top force PLd is entirely controlled by the macroscopic inertial number of the cavity I_M over a wide range of I_M, whatever the couple U and P. From quasistatic to nearly collisional flow regimes, no influence of both the stiffness and the restitution coefficient used in the contact law between grains was found in our simulations. For collisional flow regimes, increasing the latter two parameters may slightly increase $\overline{F}/(PLd)$. A significant effect of the interparticle friction was however observed, suggesting the crucial role of friction in the force transmission mechanism. For a given value of the interparticle friction, the data could be described by a robust fit showing that the force transmission is fully controlled by a rate-dependent frictional process. Further measurements (mapping of the local inertial number within the whole volume of the cavity in particular) are needed to better understand the one-to-one relation between $\overline{F}/(PLd)$ and I_M, which might emerge from the $\mu(I)$ inertial rheology. This could open a path to develop a model for predicting the mean force on the wall.

Next step of this research will tackle the force fluctuations on the wall. Since the early experimental work in a granular Couette geometry by Miller et al. (see [67]), force fluctuations in sheared granular materials received a great attention in the past recent years by analysing force fluctuations on objects moving in a static granular medium [1, 45, 97] or the force at the boundary of a granular flow during silo discharge [62, 42]. Some studies directly tracked the force fluctuations between particles in response to an external perturbation [26]. Many of those studies support the idea that force fluctuations in sheared

granular materials are mainly controlled by dynamic force chains which continuously form and collapse, through either repeated cycles of stick-slip events of the bulk granular material or other (more random) grain-scale dynamics yet to be solved. It is still unclear if the birth-death evolution remains the prevailing process over a whole range of granular flow regimes from the quasistatic regime to the dense inertial regime. The DEM simulations of the granular lid-driven cavity offer the possibility to answer the question. Preliminary analysis of the temporal force fluctuations have shown that the shape of the force distribution is fully controlled by the macroscopic inertial number, further confirming the key role played the $\mu(I)-$inertial rheology proposed by [44, 52].

Acknowledgments This work has been partially supported by the LabEx Tec21 (*Investissements d'Avenir* : grant agreement No. ANR-11-LABX-0030). Thierry Faug and Mohamed Naaim are grateful to the financial support by the People Programme (Marie Curie Actions) of the EU 7th FP under REA grant agreement No. 622899 (FP7-PEOPLE-2013-IOF, GRAINPACT).

Chapitre 3

Fluctuations de force sur un obstacle en interaction avec un écoulement granulaire cisaillé

Force fluctuations on a wall in interaction with a granular lid-driven cavity flow

Kneib F., Faug T., Nicolet G., Eckert N., Dufour F., Naaim M.

Article submitted in *Physical Review E.*

Abstract The force fluctuations experienced by a boundary wall subjected to a lid-driven cavity flow are investigated by means of numerical simulations based on the discrete element method. The time-averaged dynamics inside the cavity volume and the resulting steady force on the wall are governed by the boundary macroscopic inertial number, the latter being derived from the shearing velocity and the confinement pressure imposed at the top. The force fluctuations are quantified through measuring both the autocorrelation of force time-series and the distributions of grain-wall forces, at distinct spatial scales from particle-scale to wall-scale. A key result is that the grain-wall force distributions are entirely driven by the boundary macroscopic inertial number, whatever the spatial scale considered. In particular, the distributions at wall-scale are found to evolve from exponential to Gaussian distributions when the macroscopic inertial number is decreased. The transition from quasistatic to dense inertial flow is well identified through remarkable changes in the shapes of the distributions of grain-wall forces, accompagnied by a loss of system memory in terms of the mesoscale force transmitted toward the wall.

3.1 Introduction

Granular materials are ubiquitous in nature and daily life situations. Depending on the stress level applied, dense packings of grains can exhibit solidlike or fluidlike behaviour. The rheology of dense granular flows is a key question among others in granular physics that has attracted increasing attention in the last twenty years [44, 41, 53]. The still unsolved questions, in particular related to the transition between quasistatic and dense inertial regimes, are relevant to a number of physical problems. Two examples are the modeling of the processes at stake when a full-scale granular flow—such as an avalanche or a landslide—initiates in the release area or ceases in the runout zone on the one hand, and the optimal design of silos to guarantee an efficient transport of particles in food processing or mining industry on the other hand.

Though outstanding progress was recently made regarding the rheology of dense granular flows, most of the existing models were developed to predict the average flow with only limited attention paid to the fluctuating part (fluctuating trajectories of grains, velocity fluctuations, stress fluctuations) of the flow [53]. In a similar manner, many studies

about the force experienced by objects immersed in dense granular flows [37] focused on the average force signal but only a few of them (see for instance [45]) addressed the problem of the fluctuating part of the force signal.

There exists a large body of statistical studies which are focused on spatial force variability, more particularly on the analysis of the distributions of forces, in static (unsheared) or slowly sheared granular media, thanks to laboratory tests [69, 63, 9, 35, 65, 25], numerical simulations [4, 81, 92] and theory [61, 23, 34, 95, 96, 104, 78]. In contrast, there are only few studies that have tackled the problem of temporal and/or spatio-temporal fluctuations (the distinction between both being not so clear in a number of studies) in slow to fast flows of granular materials [67, 50, 62, 92, 45, 26, 42, 43]. Section 3.2 will give an overview of those studies

The present paper proposes to investigate in detail the fluctuating part of the force experienced by a boundary wall subjected to a granular flow. Our study is based on an original system, namely the granular lid-driven cavity, which is simulated by the discrete element method (DEM). This follows a preliminary analysis of the time-averaged dynamics of this granular cavity system that was presented in [58]. The force fluctuations experienced by the boundary wall are analysed with the help of a systematic characterization of the probability distributions of grain-wall forces, over a wide range of confinement pressure and shear velocity imparted to the cavity. Moreover, various spatial scales are analysed including particle microscale, wall macroscale, and mesoscale (intermediate between the two previous scales).

The present paper is organized as follows. Section 3.2 provides a brief state of the art on past studies dedicated to the distributions of forces in granular media. Following our initial numerical study on the time-averaged dynamics of the granular lid-driven cavity system [58], Sec. 3.3 gives a summary of the macroscopic boundary conditions and the microscopic parameters which we are using for this new numerical study. Section 3.4 recalls briefly the main results regarding the time-averaged dynamics and enriches them with analysis of the horizontal position of the vortex formed within the cavity, as well as of the local rheology in the granular bulk. Section 3.5 tackles the temporal fluctuations of force by analysing in detail the autocorrelation of the force time-series on both the entire height of the wall and portions of the wall. Section 3.6 is devoted to the analysis of the grain-wall force distributions at microscale (particle scale), macroscale (entire height of the wall) and mesoscale (portion of wall). Finally, the paper ends by discussing the main results and some potential implications for basic aspects of granular physics.

3.2 Force distributions in granular media

The present section provides an overview of the literature about contact force distributions in granular media for static (unsheared) or slowly sheared systems, as well as for fast flow systems.

For static granular packings, the $q-$model was early proposed and successful to reproduce the inhomogeneous interparticle contact force distributions observed in the pioneering experimental and numerical studies [61, 24]. In particular, the $q-$model is able to predict the remarkable exponential decay at large forces generally measured in static granular matter. The high probability (compared to a Gaussian distribution) of having forces much larger than the mean is generally associated with the ability of granular materials to develop long chainlike structures, the so-called *granular force chains*, that can support the large forces [81]. The probability density function (PDF) of interparticle contact forces f predicted by the $q-$model in static granular media under gravity takes the following form [61, 24]:

$$\mathcal{P}(f/\overline{f}) = \frac{k^k}{(k-1)!}\left(\frac{f}{\overline{f}}\right)^{k-1}\exp\left(-k\frac{f}{\overline{f}}\right), \tag{3.1}$$

where $\overline{f}$ is the mean and k is the number of downward neighbour particles considered (see much more details in [61, 24, 23]). Considering $k = 2-3$ generally gives good results for the forces larger than the mean [101, 4]. However, thanks to technological progress in the field of force sensors, a number of experimental studies identified a range of complicated shapes of contact force distributions when approaching forces much below the mean (see [4] for a detailed summary of those studies, before 2000, about distributions at weak forces). In particular, the presence of a plateau, followed by a slight increase at the smallest forces, was identified under certain circumstances. In order to fit that more complicated shape of contact force distributions, the empirical following functional form was proposed in [69]:

$$\mathcal{P}(f/\overline{f}) = a\left[1 - b\exp\left(-\frac{f^2}{\overline{f}^2}\right)\right]\exp\left(-\frac{\beta f}{\overline{f}}\right), \tag{3.2}$$

where a, b and β correspond to the PDF parameters fitted on the experimental measurements made by [69]. A slight modification of Eq. (3.2) was proposed by [9] to interpret their experimental data on the effect of both packing order (disordered packings versus highly ordered—crystalline—configurations) and interparticle friction on $\mathcal{P}(f)$. Finally, it is worthwhile to note that log-normal distributions were reported in some studies [76, 30].

As discussed in a recent review in [78] and a number of references therein, the key features of the contact force distributions in static or very slowly sheared granular packings can be summarized as follow : i) the distribution functions fall-off exponentially at

large forces, ii) a small peak, or plateau, is observed below the mean force, and iii) the vanishingly small forces remain highly probable. In his review about granular force transmission in static granular packings, Radjai [78] proposed an elegant model for contact force distributions and derived an analytical expression for the density function able to predict the three aforementioned features :

$$\mathcal{P}(f) = \beta_0(1+\gamma_0)\frac{\gamma_0 \exp(\beta_0 f)}{[1+\gamma_0 \exp(\beta_0 f)]^2}, \tag{3.3}$$

where β_0 (homogeneous to a force) and γ_0 (dimensionless coefficient) are the PDF parameters. Under the normalization $\overline{f} = 1$, β_0 and γ_0 are linked by the relation $\beta_0 = (1+\gamma_0)\ln[(1+\gamma_0)/\gamma_0)]$. Though further studies are needed to relate γ_0 to actual physical properties of the grains, varying γ_0 allows to cover a wide range of distributions with or without the presence of a peak [78].

Among the great number of experimental, numerical and theoretical results concerning the shape of force distributions in static packings or slowly sheared granular media, a key result is that the distribution at small forces (plateau versus peak, maximum value, non-zero value at vanishingly small force, etc.) is found to be very sensitive to the granular sample preparation and shear history the system experiences [4, 78]. While interpreting distributions of contact forces in static granular packings, Antony [4] concluded that it is required to pay a due attention to the shear strain level and any other quantities related to shear history, such as the volume fraction. A theoretical study on static packings proposed by [96] predicted a broadening of the distribution while increasing the shear stress level, moving from distributions with a peak below the mean value to exponential distributions. Two-dimensional granular packings under anisotropic stresses were studied theoretically by [104], showing that an increase in the stress anisotropy produced a transition from distributions with a peak below the mean to exponential distributions.

A few studies observed the possibility of a crossover in the shape of $\mathcal{P}(f)$ from exponential to Gaussian at large confining pressure [101, 102, 66]. This change in the shape of $\mathcal{P}(f)$ was attributed to very large deformations of particles [9]. The effect of particle stiffness on distributions of contact forces in static packings was investigated by Erikson et al. [35]. They found that beyond a high threshold—around 30% of deformation, the distributions became sensitive to the particle stiffness. Decreasing the particle stiffness led to an increase in the peak and of the slope of the exponential decay at large forces, thus producing a distribution likely to evolve toward a Gaussian distribution. The increase of the peak by decreasing the particle stiffness was also derived from the theory in [96] (note that this theory predicts an increase of the non-zero value at $f = 0$). In the limit of rigid grains (as addressed in the present study), one can conclude that the distributions are very weakly—not to say not—affected by the particle stiffness.

The pioneering laboratory measurements of contact forces distributions in granular

media (see for instance [61, 69, 63, 66, 9]) were confined to contact forces between a grain packing and a boundary wall. It is worthwhile to note that some studies paid attention to the cross-comparison between the grain-grain (inside the bulk) contact force distributions and the grain-wall contact force distributions. No significant difference was found for static packings [80, 95, 96], suggesting that the results for the distributions at the boundary walls may generally be extended to the grain-grain contact forces.

For slowly sheared granular packings, the effect of a slight variation of the volume fraction on the shape of distributions was evidenced by the two-dimensional experiments on a granular Couette geometry [50]. The authors observed exponential distributions at the smallest volume fraction (around 0.78 in their 2D system), while the distributions exhibited a peak at larger volume fraction (around 0.81). Interestingly, Howell et al. [50] provided a comparison between the distributions at the particle scale to the distributions averaged over a great number of particles (~ 260 in their study). For the latter, they found that at large volume fraction the distributions became nearly Gaussian. The transition from exponential distributions to narrower distributions with the presence of a peak while increasing packing density was also reported in a theoretical study based on the analogy with supercooled liquids and foams [75].

A study on relatively fast granular flows (a silo discharge) identified the effect of the velocity (flow rate at the exit of the silo) on the shape of distributions [62]: the authors observed a broadening of the distribution at large velocities. A similar conclusion was drawn from the experiments on objects dragged into a static granular medium in an annular cell by Geng et al. [45], who observed broader distributions at large rotation speeds of the annular cell. The theoretical study of O'Hern et al. [75] based on the analogy with supercooled liquids and foams predicted the broadening of distributions with the increase of the shear stress.

The original system considered in the present paper, namely the granular lid-driven cavity, makes possible the investigation of a wide range of boundary conditions in terms of shearing velocity and confinement pressure, keeping the granular bulk relatively dense. This allows to investigate, for the first time, how the distributions of grain-wall contact forces evolve over a wide range of both shearing velocity and confinement pressure imposed on the granular medium, and considering different spatial scales from a single grain to the entire boundary wall.

3.3 The granular lid-driven cavity simulated by DEM

3.3.1 Macroscopic boundary conditions

A planar assembly of spheres is trapped into a box made of four walls, as sketched in Fig. 3.1. The bottom horizontal wall is fixed and rough, while both lateral walls are fixed,

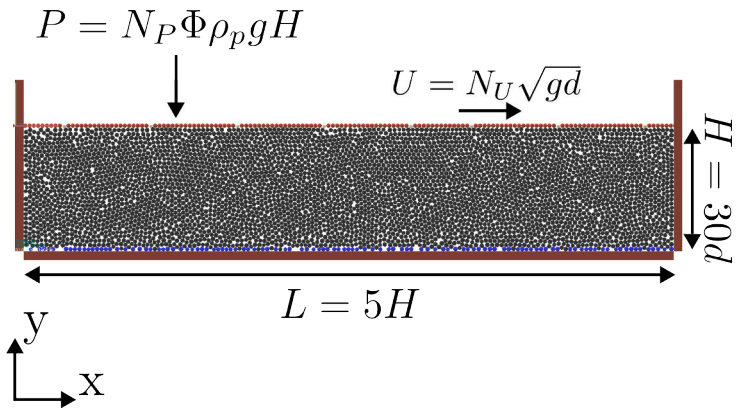

FIGURE 3.1 – Geometry and boundary conditions for the lid-driven cavity simulated by DEM. The granular sample is trapped between four walls, the top one (the lid) applies the shear displacement U and the confinement pressure P (see text for details).

smooth and spaced by a distance $L = 5H$. The upper horizontal wall, namely the lid, is rough and has an infinite length that allows for a uniform horizontal displacement, thus producing a constant shearing of the sample at velocity U. A constant vertical confinement force F_c is added continuously to the lid whose vertical position is computed through the DEM algorithm. Although the grains reaction to this force is not homogeneous along the lid—but rather exhibits an exponential shape (see figure 4 of our preliminary study on this system [58]), an equivalent macroscopic confinement pressure P can be defined from the system dimensions : $P = F_c/Ld$. As the grains are forced to stay inside the cavity and the force profile is heterogeneous, a perpetual circulation takes place within the whole volume of the cavity, as further discussed in Sec. 3.4 of the present paper.

The following dimensionless macroscopic parameters are used to run the numerical simulations over a broad range of confinement pressure P and shear velocity U, namely N_P and N_U :

$$P = N_P \Phi \rho_p g H, \tag{3.4}$$

$$U = N_U \sqrt{gd}. \tag{3.5}$$

The gravity acceleration $g = 9.81$ m s^{-2} is used for convenience in order to facilitate the parallel with any potential real laboratory tests in the future, though the numerical system considered here is gravity-free. A constant macroscopic volume fraction $\Phi = 0.6$ is considered here, which corresponds roughly to the random close packing of a three dimensional assembly of spheres of width d. The particle density was taken equal to $\rho_P = 2500$kg m^{-3}.

The cavity is initially filled of grains under gravity deposition in order to produce a dense granular packing of height H. Once the system reaches the static equilibrium, the

gravity is set to zero and the shearing starts for a period of 10 seconds. As it will be defined in Sec. 3.5 (see Fig. 3.6), the data recording starts one second after the shearing has started. One second typically corresponds to the maximal time needed for the system to reach a permanent regime in terms of force measured on the sidewall (see also more detail in [58]). In most of the simulations presented in the present study, H/d was taken equal to 30 with $H = 0.3$m and $d = 1$mm. Some results from numerical simulations with $H = 0.3$m but $d = 0.3$mm will be discussed in conclusion.

Following the analysis proposed by [44] at the local grain scale, if we consider the typical time $t_P = d\sqrt{\rho/P}$ associated with the top confinement pressure P and the typical time $t_U = H/U$ equal to the inverse of the macroscopic shear rate, one can define the macroscopic inertial number I_M :

$$I_M = \frac{t_P}{t_U} = \frac{d\sqrt{\rho/P}}{H/U}, \tag{3.6}$$

where $\rho = \Phi\rho_P$ holds for the density of the granular sample within the cavity.

In the present study, N_P varied from 0.01 to 100 and N_U from 1 to 20, which allows to investigate a wide range of granular flow regimes defined by I_M ranging typically from $5\ 10^{-4}$ to 0.6. A very slight variation of Φ_*—the volume fraction actually measured in our simulations— with the boundary conditions in terms of U and P was observed. This point will be discussed in Sec. 3.7. In addition to I_M, another dimensionless parameter that controls the system is the length L of the cavity relative to its height H. It has been shown in our preliminary study of this granular lid-driven cavity system [58] that the constraint $L/H \geq 5$ should be respected to prevent an effect of the cavity length on the steady force experienced by the wall facing the shear displacement (namely the right sidewall shown in Fig. 3.1).

All the results shown in the present paper were obtained for $L/H = 5$, but their sensitivity to L/H was investigated by performing simulations with $L/H = 7$ and $L/H = 10$. This sensitivity analysis revealed that—as observed for the mean force, the force fluctuations remainded not influenced by L/H as soon as $L/H \geq 5$.

3.3.2 Micromechanical parameters

The grain-grain and the grain-wall interactions are handled by a viscoelastic contact law for the normal force and an elastic force with a Coulomb threshold for the shear force. The normal contact force $\boldsymbol{F_n}$ and the shear contact force $\boldsymbol{F_s}$ are expressed as :

$$\begin{cases} \boldsymbol{F_n} = \max(0, k_n\delta_n + c_n\dot{\delta}_n)\boldsymbol{n}, \\ d\boldsymbol{F_s} = (k_s\dot{\delta}_s dt)\boldsymbol{s}, \\ |\boldsymbol{F_s}| \leq \mu|\boldsymbol{F_n}|, \end{cases} \tag{3.7}$$

where $\boldsymbol{n}$ is the normal of the contact plane, $\boldsymbol{s}$ is the unity vector along the shear direction ($\boldsymbol{n} \cdot \boldsymbol{s} = 0$), k_n and k_s are the normal and tangential contact stiffnesses, δ_n is the normal penetration depth, $\dot{\delta}_s$ is the tangential displacement increment, μ is the local friction coefficient, c_n is the normal viscosity coefficient and dt is the timestep.

For a contact between two identical spheres of diameter d, Young's modulus E and Poisson's ratio ν, the contact stiffnesses can be computed as :

$$\begin{aligned} k_n &= \frac{1}{2} E d, \\ k_s &= \nu k_n. \end{aligned} \tag{3.8}$$

The contact law is governed by four physical parameters : E, ν, c_n and μ. It has been discussed in a number of studies (see [40, 58] and references therein) that E can be reduced to decrease the total time of calculation without changing the numerical results, as long as we stay in the limit of rigid grains. Such a limit of rigid grains is verified if, for instance, we take $N_0 = E/(2P) = 1.5\ 10^4$, where P holds for the macroscopic confinement pressure and N_0 is a dimensionless number. c_n is set in the same manner as in [58], with a restitution coefficient $e = 0.5$. Most of the simulations were conducted with $\mu = 0.5$ but we will shortly discuss some results with $\mu = 0.27$ in the conclusion. In order to avoid crystallization, the grain diameters are homogeneously chosen between $d(1 - d_{disp})$ and $d(1 + d_{disp})$ where $d_{disp} = 0.15$.

3.4 Time-averaged dynamics

The overarching goal of the present paper is to study in detail the force fluctuations experienced by the boundary wall that faces the direction of the shearing velocity at the top. In our previous study of this system [58], we reported an analysis of the results regarding the time-averaged dynamics. Before going into the details of force fluctuations, this section proposes to recall some important results reported in [58] and to further extend some of the results concerning the time-averaged dynamics.

3.4.1 Steady vortex and mean force

The macroscopic inertial number I_M, defined from the boundary condition [see Eq.(3.6)], is the relevant parameter to quantify the flow inertial state and to predict the mean force experienced on the sidewall scaled by the force imposed at the top, namely $\overline{F}/(PLd)$ (see figure 8 in [58]). More specifically, our previous study showed that the mean force on the right sidewall is entirely controlled by the changes in granular flow regimes, the latter regimes being governed by the macroscopic inertial number. In the quasistatic regime at low I_M, $\overline{F}/(PLd)$ is constant. In the dense inertial regime at intermediate I_M,

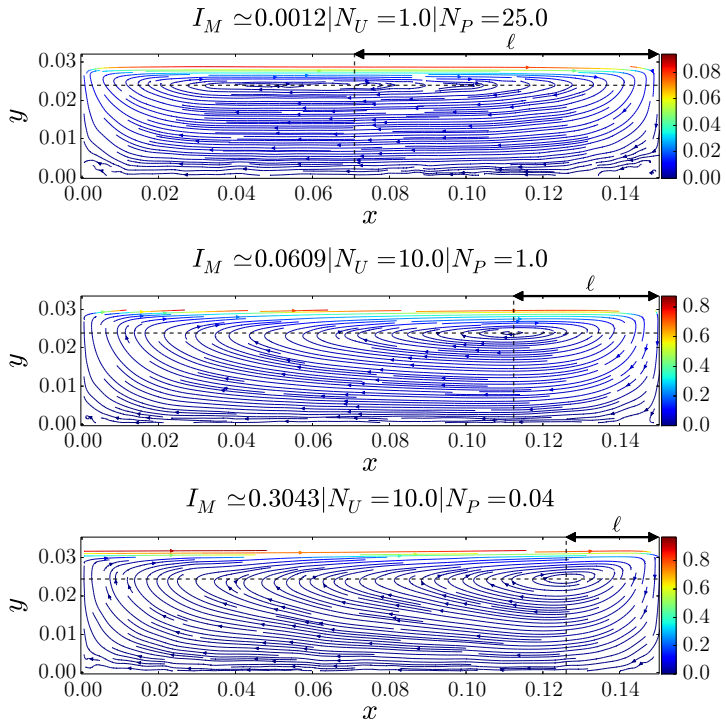

FIGURE 3.2 – Time-averaged streamlines within the cavity for three different values of I_M : $I_M = 1.2\ 10^{-3}$ (top panel), $I_M = 6\ 10^{-2}$ (middle) and $I_M = 0.3$ (bottom).

$\overline{F}/(PLd)$ is a nearly-linear increasing function of I_M. In the rapid regime at higher I_M values, $\overline{F}/(PLd)$ starts saturating. The measurement of time-averaged local granular flow velocity-fields revealed the formation of one single vortex occupying the whole volume of the cavity. This cavity-scale vortex is caused by the fact this system forces the grains to move within the cavity volume, without any possibility to escape it.

Figure 3.2 shows examples of the streamlines inside the cavity for low ($I_M = 1.2\ 10^{-3}$), intermediate ($I_M = 6\ 10^{-2}$) and high ($I_M = 0.3$) values of I_M. The $x-$position of the vortex centre along the cavity was extracted from the streamlines (as shown by the vertical dotted lines in Fig. 3.2), thus allowing to deduce the horizontal distance ℓ between the vortex center and the right sidewall. The top graph in Fig. 3.3 shows ℓ scaled by the cavity length L as a function of I_M. In the quasistatic regime ($I_M \lesssim 10^{-2}$), ℓ is relatively constant at an approximative value of $L/2$, meaning that the vortex is centered. Beyond $I_M \lesssim 10^{-2}$, the symmetry of the velocity pattern is lost, as depicted by ℓ/L which starts decreasing sharply. The vortex centre is more and more shifted toward the right sidewall when I_M is increased, thus producing an important horizontal asymmetry at the highest I_M.

Figure 3.3 depicts how the mean force on the wall $\overline{F}$ relative to the typical pressure force PLd imposed at the top evolves with the macroscopic inertial number (see [58] for more details). The variation of both $\overline{F}/(PLd)$ and ℓ/L with I_M reveals the same transition

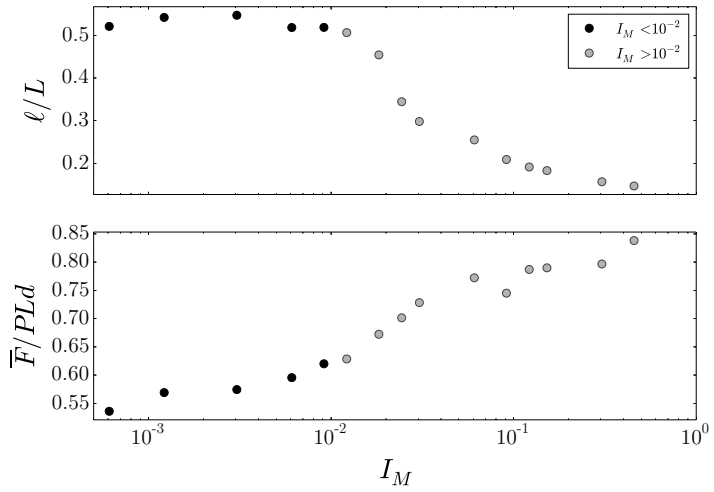

FIGURE 3.3 – Distance of the vortex center from the right sidewall, ℓ, relative to the cavity length L, as a function of the macroscopic inertial number I_M (top panel). Mean force $\overline{F}$ on the wall relative to the pressure force PLd imposed at the top, as a function of I_M (bottom panel).

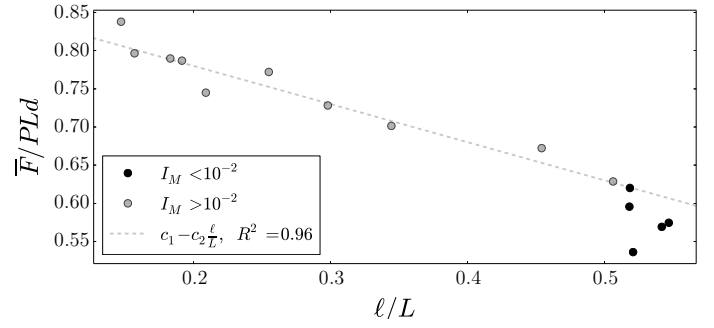

FIGURE 3.4 – $\overline{F}/(PLd)$ versus ℓ/L. The grey dashed line is a fit of Eq.(3.9) for $I_M > 10^{-2}$. This graph reveals that the mean force on the wall is entirely controlled by the distance of the vortex from the right sidewall.

from quasistatic to dense inertial regime. While comparing the two curves, a significant coupling can be detected, which becomes obvious when plotting $\overline{F}/(PLd)$ as a function of ℓ/L in Fig. 3.4. $\overline{F}/(PLd)$ and ℓ/L are linearly linked, meaning that the mean force on the wall scaled by PLd may be deduced from the vortex position, and vice-versa. It is worth noting that the scattering at low $\overline{F}/(PLd)$ in Fig. 3.4 is due to the very low velocity of the flow in this region, making difficult the identification of the vortex centre position.

In our previous study, we proposed an empirical scaling for $\overline{F}$ as a function of I_M in the following form [58]: $\overline{F} = PLd\,[r_1 + (r_2 - r_1)f(I_M)]$, where $f(I_M) = (1 + I_M^0/I_M)^{-1}$, and r_1, r_2 and I_M^0 were constant fitting parameters. For the data shown in Fig. 3.3, a good fit is obtained with $r_1 = 0.53$, $r_2 = 0.86$ and $I_M^0 = 0.02$. The interparticle friction does affect the values of r_1, r_2 and I_0, as it will be discussed in Sec. 3.7.

Considering that the mean force on the wall is controlled by the distance of the vortex center from the wall (ℓ being a function of I_M as displayed in the top panel of Fig. 3.3), we can specify another scaling that is given by the following relation :

$$\overline{F} = PLd\left(c_1 - c_2\frac{\ell(I_M)}{L}\right), \tag{3.9}$$

where c_1 and c_2 are two constants that may depend on the micromechanical parameters of the grains. In this specific case $c_1 = 0.88$ and $c_2 = 0.5$, as shown by the dashed line in Fig. 3.4.

The above analysis showing the link between the vortex center position and the mean force on the right sidewall (that faces the shearing direction at the top) further extends the results reported in [58] concerning the mean dynamics of the granular lid-driven cavity. For given micromechanical grain properties, all macroscopic physical quantities measured in the cavity can be deduced from the macroscopic inertial number defined on the imposed shearing velocity and confinement pressure.

3.4.2 The local $\mu(I)-$rheology

To further test the rheology, the local effective friction μ_{loc} and the local inertial number I were measured within the whole volume of the cavity. Detailed steps for the calculation of those local quantities are provided in appendices 3.8 and 3.8. Though the strain field is rather complicated inside the cavity (see the streamlines in Fig. 3.2), the local $\mu(I)-$rheology, given by the relation $\mu_{th} = \mu_1 + (\mu_2 - \mu_1)(1 + I/I_0)^{-1}$ [52], was found to be valid in most of the cavity volume. The values found for the parameters of the $\mu_{loc}(I)-$friction law were $\mu_1 = 0.12$, $\mu_2 = 0.40$ and $I_0 = 0.13$ (see much more details in appendix 3.8). The difference between the μ_{loc} actually measured and μ_{th} was calculated. Figure 3.5 displays the results in terms of maps of $|\mu_{loc} - \mu_{th}|$, for two distinct values of $I_M \sim 10^{-2}$ and $I_M \sim 6\,10^{-2}$.

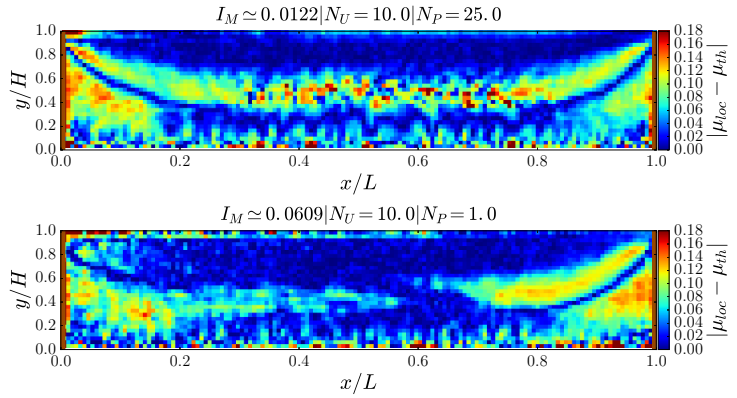

FIGURE 3.5 – Maps of $|\mu_{loc} - \mu_{th}|$ for $I_M = 1.22\,10^{-2}$ (top panel) and $I_M = 6.09\,10^{-2}$ (bottom panel).

At $I_M \sim 10^{-2}$, a symmetrical bow-like pattern appears across the entire length of the cavity (see top panel). Similar symmetrical bow-like patterns (not shown here) were systematically obtained for I_M below 10^{-2}. Above the bow-like pattern and below it (apart from the two regions close to the two lateral walls), $|\mu_{loc} - \mu_{th}|$ is nil, which means that the sample is well governed by the $\mu(I)-$inertial rheology. For higher values of I_M (see bottom panel in Fig. 3.5), the symmetry and the bow-like shape were broken. In other words, the region inside the cavity where $|\mu_{loc} - \mu_{th}|$ was nil could extend over the whole height of the cavity.

Note that Fig. 3.5 displays the absolute values of $\mu_{loc} - \mu_{th}$, thus preventing the detection of negative values. However, a great number of values of μ_{loc} were found to be lower than μ_1 for I_M below 10^{-2} (see Fig. 3.18 in appendix), which corresponds to the region in the center of the cavity in the top panel of Fig. 3.5 (forming the bow-like pattern across the entire length of the cavity). These negative values of $\mu_{loc} - \mu_{th}$ that suggest the presence of non-locality [54] will deserve further investigation in the future.

In conclusion, the crossover from a bow-like pattern extending across the entire length of the cavity to a smaller pattern in the confines of the boundary wall appears to be a clear signature of the quasistatic to dense inertial transition in the system studied here. The rest of the paper is devoted to the influence of the macroscopic inertial number on the force fluctuations.

3.5 Force data autocorrelations

3.5.1 Data recordings

While analysing temporal fluctuations, data acquisition frequency requires a particular attention : it has to be large enough to be able to capture short-life force events, and simultaneously small enough to avoid practical memory allocation issues while recording

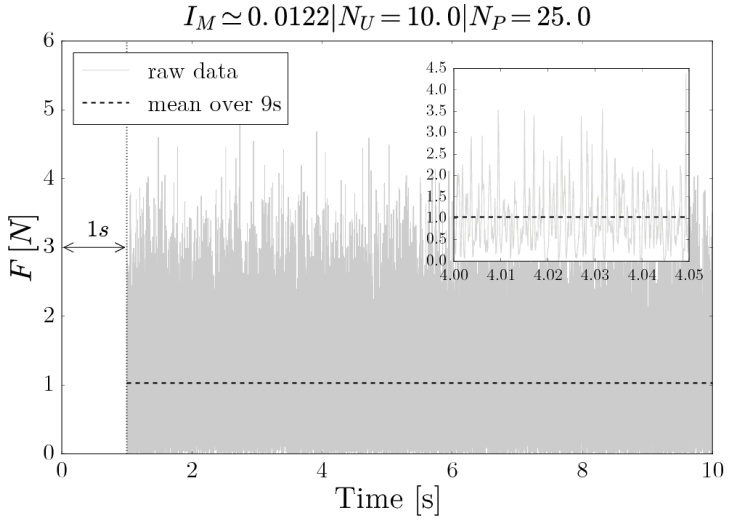

FIGURE 3.6 – Example of time-series of total force on the wall, obtained for $N_U = 10$ and $N_P = 25$. The instantaneous force F is highly fluctuating over time. The horizontal dashed line depicts the value of the time-averaged force, named $\overline{F}$, reached in the steady-state regime (after a short transient of about 1s). Inset : same data, zoomed in a time window of 0.05 s.

trends over large durations. The DEM algorithm is not able to model oscillating phenomena that occur at frequencies higher than the typical natural contact frequency f_c. In the present statistical study the record frequency f_{rec} was set to 10 kHz and f_c typically ranged from 4.8 kHz to 320 kHz. The frequency corresponding to the DEM timestep was systematically set to $10 f_c$, avoiding any instability issues. The overlap between f_{rec} and the lowest values of f_c may cause the recording of unintended effects caused by particle oscillations. It has been verified that neither the autocorrelations nor the distributions of the force time-series presented in the following statistical study are sensitive to f_{rec} by comparing to simulations with a doubled (20 kHz) and a halved (5 kHz) record frequency.

3.5.2 Force time-series autocorrelation

The force time-series on the right sidewall of the cavity show high temporal fluctuations, as displayed in Fig. 3.6. This section aims at studying these fluctuations by analysing the autocorrelation of force time-series. The first information that will be extracted is the force periodicity. The latter is for instance a sensitive data while designing civil engineering structures subjected to granular avalanche-flows, if one wants to avoid a resonance phenomenon around the natural frequency of the impacted structure. The second information arising from force autocorrelation is the critical autocorrelation time Δt_c, which can be interpreted as the time after which the system has forgotten a certain force value on the wall. In other words, it reflects the typical time during which a future state of the system keeps history of its past state regarding the force transmitted to the wall.

We denote by $\mathcal{C}(F(t), F(t+\Delta t))$ the temporal autocorrelation function, where Δt is the lag between two system states. The critical autocorrelation time Δt_c is defined with an arbitrary low autocorrelation threshold :

$$\mathcal{C}\left(F(t), F(t+\Delta t_c)\right) = 0.15. \tag{3.10}$$

It is worthwhile to note that the above threshold value does not influence the conclusions presented here as they are qualitative, focused on main trends. Since the local autocorrelation function $\mathcal{C}(F(t), F(t+\Delta t))$ is likely to be a non monotonic function, it is expected to cross the threshold many times. In this case, because we focus on the initial autocorrelation decrease corresponding to memory loss and we want to avoid any effect of the signal noise, the lowest value of Δt_c is kept.

In the following, we present the autocorrelation of force time-series at macroscopic scale, i.e. on the entire height of the wall (Sec. 3.5.2). Then the autocorrelation at mesoscopic scale is studied by splitting the wall height into ten portions of a few grains each (Sec. 3.5.2).

Autocorrelation for the entire height of the wall

Figure 3.7 depicts the autocorrelation of the force signal on the entire height of the right sidewall, for five values of the macroscopic inertial number I_M.

Because of the strong stress localisation taking place at the top right corner of the cavity (see more detail on this wedge effect in [58]), the shearing frequency at the roughness (particle) scale is transmitted to the right sidewall, as long as I_M is not too high (typically smaller than 10^{-2}). Sinusoid-like oscillations are therefore observed, with a decreasing period while increasing N_U. The inset of Fig. 3.7 shows a collapse of sinusoid-like oscillations when the autocorrelation function is plotted versus $(U/d)\Delta t$, the wavelength associated with these oscillations being d (the diameter of the grains composing the top wall roughness and shearing the sample).

For the highest I_M, this effect is absent, which is in agreement with a more inertial regime for which short-time collisions occur in addition to enduring frictional contacts able to transmit the shear force. The mean free path of grains increases, which makes impossible any continuous transmission of enduring contacts between grains. Again, we detect the transition from the quasistatic to the dense inertial granular regime occurring around $I_M = 10^{-2}$, which is a value similar to the one extracted from the time-averaged dynamics in Sec. 3.4.

The general shapes of the autocorrelation functions shown in Fig. 3.7 resemble a lot the ones found by Geng et al. [45] in their experimental study of an intruder slowly dragged into a granular medium (see figure 8 in [45]). We generally observe that $\mathcal{C}(F(t), F(t+\Delta t))$ drops quickly (exponentially) to zero over a time scale Δt_c and then fluctuate around zero.

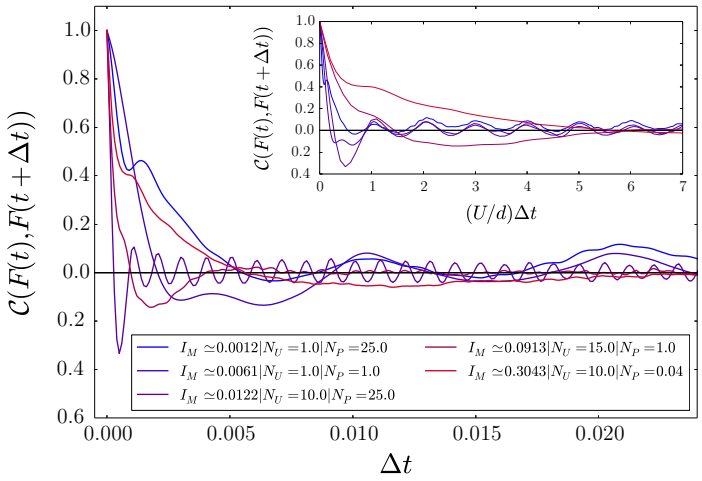

FIGURE 3.7 – Evolution of $\mathcal{C}(F(t), F(t+\Delta t))$ over time for five values of I_m, where $F(t)$ is the force time-series on the entire right sidewall. Inset : $\mathcal{C}(F(t), F(t+\Delta t))$ plotted against $(U/d)\Delta t$ to highlight the oscillations wavelength.

These fluctuations are well explained in our system by the typical frequency U/d associated with the shearing velocity at the top and the grain size (see discussion above). We were not able to find a clear dependency of the critical time Δt_c on either the macroscopic inertial number I_M or any input parameter such as the shear velocity of the lid, or the confinement pressure at the top. In the following, we focus on portions of the wall.

Autocorrelation for portions of the wall

The force time-series on the right wall is the result of the cumulative contact forces applied over the entire height of the wall. Consequently, the strong spatial heterogeneity of the granular lid-driven cavity system may require a more localized analysis by taking into account the position at which individual forces are applied to the wall. We propose here to investigate the autocorrelation of force time-series on some portions of the wall. The entire wall height is split into ten slices $i \in \{1...10\}$ of identical size. Each slice has its associated force time-series from which the autocorrelation $\mathcal{C}^i(F(t), F(t+\Delta t))$ is then computed.

Figure 3.8 shows the autocorrelation of force time-series for each of the ten identical wall portions, for three values of the macroscopic inertial number. The signal periodicity already discussed above is still observed at the frequency U/d—associated with the roughness of the top wall moving at velocity U. This is particularly clear in the simulation at $I_M = 1.2\ 10^{-2}$ for which each temporal autocorrelation curve shows this period, whatever the vertical slice i considered along the wall. This indicates that the periodic fluctuations at the top can be transmitted to the lowest position at the bottom of the cavity. This result is consistent with the fact that we could identify a small, yet non-zero, spatial

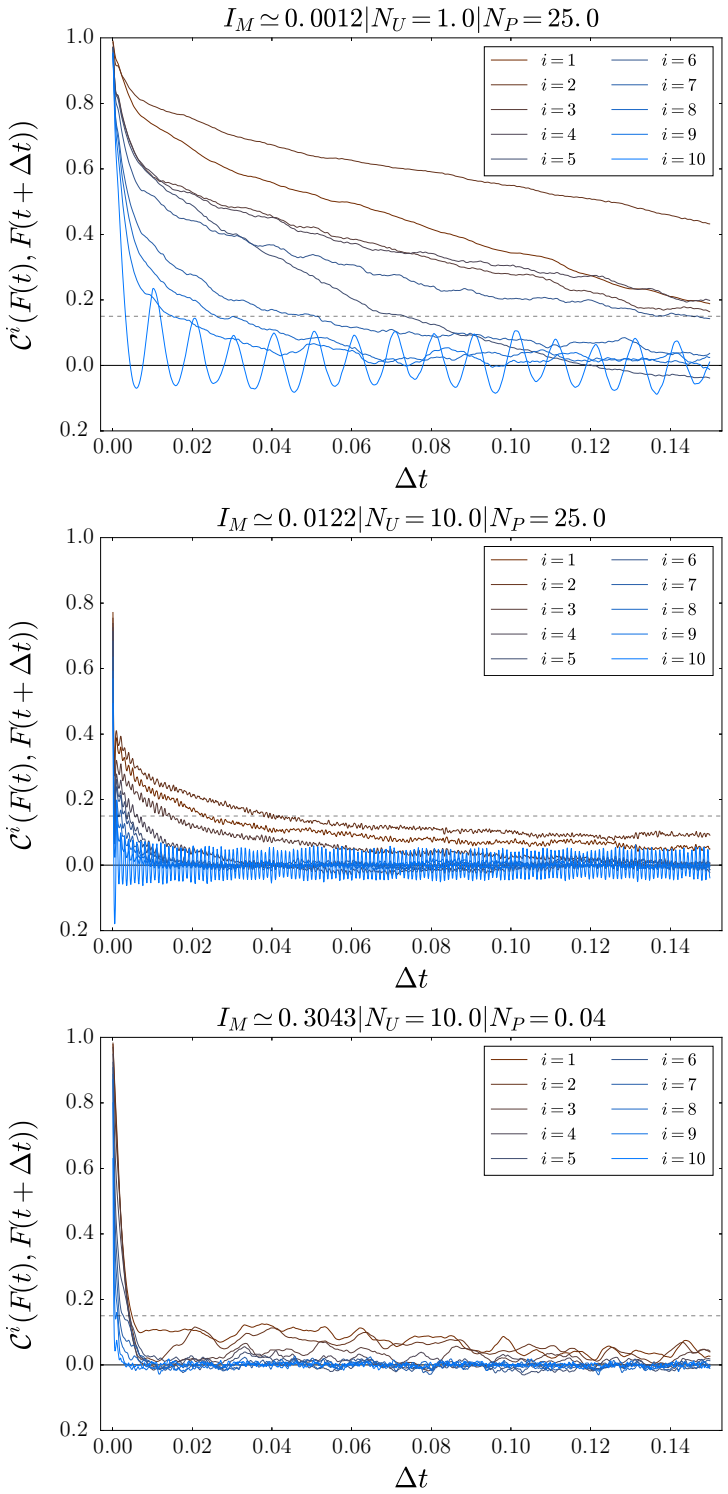

FIGURE 3.8 – Evolution of $\mathcal{C}^i(F(t), F(t+\Delta t))$ over time measured on 10 portions i of wall, for three values of I_M. In each graph, the horizontal dashed line shows the threshold of 0.15 that was used to derive Δt_c^i.

autocorrelation at $I_M = 1.2\ 10^{-2}$ (not shown here). At the lowest $I_M = 1.2\ 10^{-3}$, the periodicity caused by the top roughness is present at the highest portion of the wall ($i = 10$) but quickly fades while going deeper into the sample along the wall, and even disappears for the lowest position at the bottom of the cavity. In contrast to the intermediate I_M, the periodic fluctuations from the top wall cannot be transmitted over the entire depth of the wall. This observation is in accordance with the fact that at $I_M = 1.2\ 10^{-3}$ we did not find any spatial autocorrelation (not shown here). There might exist some zones near the cavity top inside which the grains have enough time to rearrange locally, thus being able to relax the high stress caused by jamming close to the wedge. At higher I_M, the periodic fluctuations associated with the roughness of the top wall are lost whatever the vertical position along the wall, thus further confirming the transition toward a much more inertial regime for which the increase of the mean free path between grains prevents the transmission of those fluctuations (see Sec. 3.5.2).

Figure 3.9 shows the mean value of autocorrelation time, $<\Delta t_c>$, averaged over all portions of the wall. Though there is some data scattering regarding Δt_c^i (see grey-colored crosses on Fig. 3.9), this plot demonstrates that there exists a I_M below which $<\Delta t_c>$ is not zero and beyond which $<\Delta t_c>$ vanishes. In other words, it means that beyond a I_M ($\simeq 10^{-2}$) it is not possible to predict a future system state from the past one, thus indicating that the memory of the system is completely lost. This observation was still valid by increasing L/H from 5 to 10 (not shown here). The granular lid-driven cavity system suggests here a remarkable transition from the quasistatic to the dense inertial granular regime, which is characterized by a total loss of *system memory* (not intrinsic to the material) in terms of the force transmission from the top wall toward the right sidewall.

3.6 Force distributions

The distributions of force time-series on the sidewall give crucial information on fluctuations, as they quantify the probability of each force value the sidewall may experience. In this section, the analysis of force distributions concerns three spatial scales : the microscale focused on individual grain-wall contact forces, the macroscale focused on the total force on the wall, and the mesoscale focused on the force experienced by portions of wall. For each scale, the distribution response to the same wide range of I_M as tackled in the previous sections is investigated. All distributions presented in this section were obtained from quantities that were scaled by their time-averaged value.

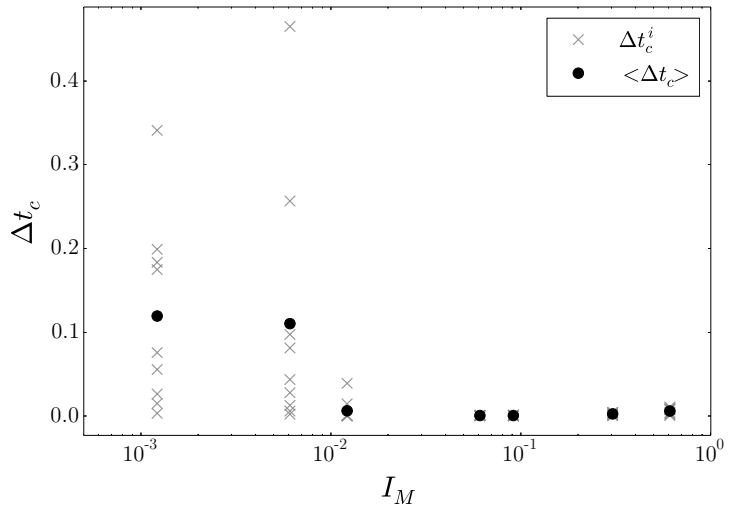

FIGURE 3.9 – Critical time Δt_c^i (cross symbols) beyond which the force time-series becomes weakly correlated ($\mathcal{C} < 0.15$)—for ten portions $i \in [1;10]$ of the wall height, as a function of I_M. The full circles show $<\Delta t_c>$ that is the mean over the ten Δt_c^i values. The data were extracted from the autocorrelation functions plotted on Fig. 3.8

3.6.1 Force distributions at microscale

The distributions of contact forces measured in our DEM simulations, for grains in contact with the right sidewall, characterize the typical forces repartition applied locally on the wall (grain scale). Recorded contact forces on the wall from all recording times are merged to form the sample, and then the probability distribution is computed. Let us note f an individual grain-wall contact force and $\overline{f}$ the overall mean grain-wall contact force of a simulation. In the following, $\widetilde{f} = f/\overline{f}$ is the scaled grain-wall particle contact force.

Figure 3.10 shows examples of distributions of $\widetilde{f}$ obtained with three different values of I_M but from several distinct dipoles (N_U, N_P). The remarkable result is that the distributions collapse very well at each I_M, revealing that the repartition of particle contact forces on the wall is entirely controlled by the macroscopic inertial number of the granular lid-driven cavity.

Figure 3.11 shows the distributions of $\widetilde{f}$ computed for several I_M. We have tested a number of well-established PDFs to fit these curves, as well as theoretical or empirical PDFs discussed in the literature for granular contact forces, specifically the ones proposed by [69] [Eq. (3.2)] and [78] [Eq. (3.3)] (see Sec. 3.2). None of those PDFs was able to give conclusive results over the whole range of I_M tested in our DEM simulations. The results were conclusive, over the whole range of I_M, with a truncated log-normal distribution that reads as follows :

$$\mathcal{P}(\widetilde{f}) = \frac{1}{\mathcal{S}} \frac{1}{\widetilde{f}_\sigma \sqrt{2\pi}(\widetilde{f} + \widetilde{f}_0)} \exp\left(-\frac{[\ln(\widetilde{f} + \widetilde{f}_0) - \widetilde{f}_\mu]^2}{2\widetilde{f}_\sigma{}^2} \right), \tag{3.11}$$

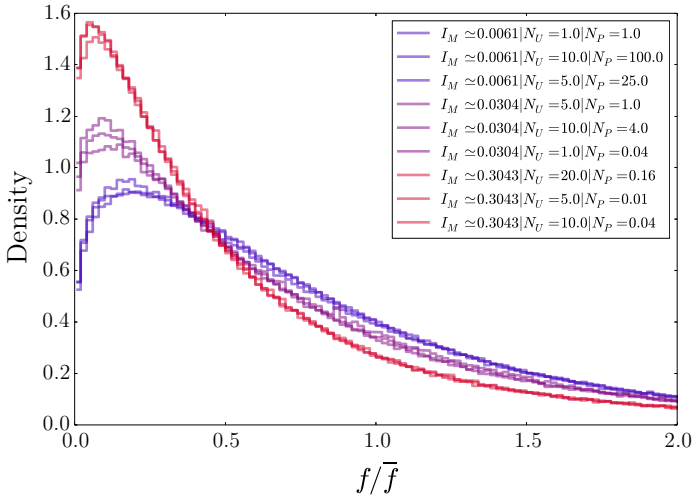

FIGURE 3.10 – Probability distributions of contact forces for grains in contact with the wall. For each I_M the curves are collapsing whatever the dipole (U, P), thus demonstrating that the boundary macroscopic inertial number fully controls the grain-wall contacts distributions.

where $\widetilde{f} > 0$, $\widetilde{f}_0 > 0$, and $\mathcal{S}$ is the normalization factor corresponding to the value at $\widetilde{f}_0$ of the survival function of the (untruncated) log-normal PDF. The scale parameter $\widetilde{f}_\mu$, the shape parameter $\widetilde{f}_\sigma$ and the location parameter $\widetilde{f}_0$ are monotonic functions of the macroscopic inertial number I_M, as shown at the bottom panel of Fig. 3.11.

Apart from the fact that the best fits were obtained with the truncated log-normal distributions over the whole range of I_M tested, it remains challenging to provide physically-based arguments to justify the use of such a PDF. A key result of the present study is that the parameters of Eq. (3.11) are found to be well-defined monotonic functions of I_M (see bottom of Fig. 3.11). This opens a path to predict the force distributions empirically, as long as the boundary macroscopic inertial number is known. A question then arises : does that key result too hold for the distributions of the total force on the entire height of the wall ?

3.6.2 Force distribution at macroscale

Figure 3.12 shows the distribution of $\widetilde{F}$, the total force time-series exerted on the sidewall scaled by its mean $\overline{F}$, for seven values of I_M ranging from 1.2 10^{-3} to 0.6. At the lowest I_M in the quasistatic regime, the distribution are nearly Gaussian whereas at the highest I_M, the PDF has an exponential shape. This result is consistent with the crossover from exponential to Gaussian PDFs generally observed at high confinement pressures in some past studies [101, 102, 66] (as reviewed in Sec. 3.2).

At intermediate I_M in the dense inertial regime, the distribution has a more complex shape : at a first glance, it may appear as a distribution which would combine some

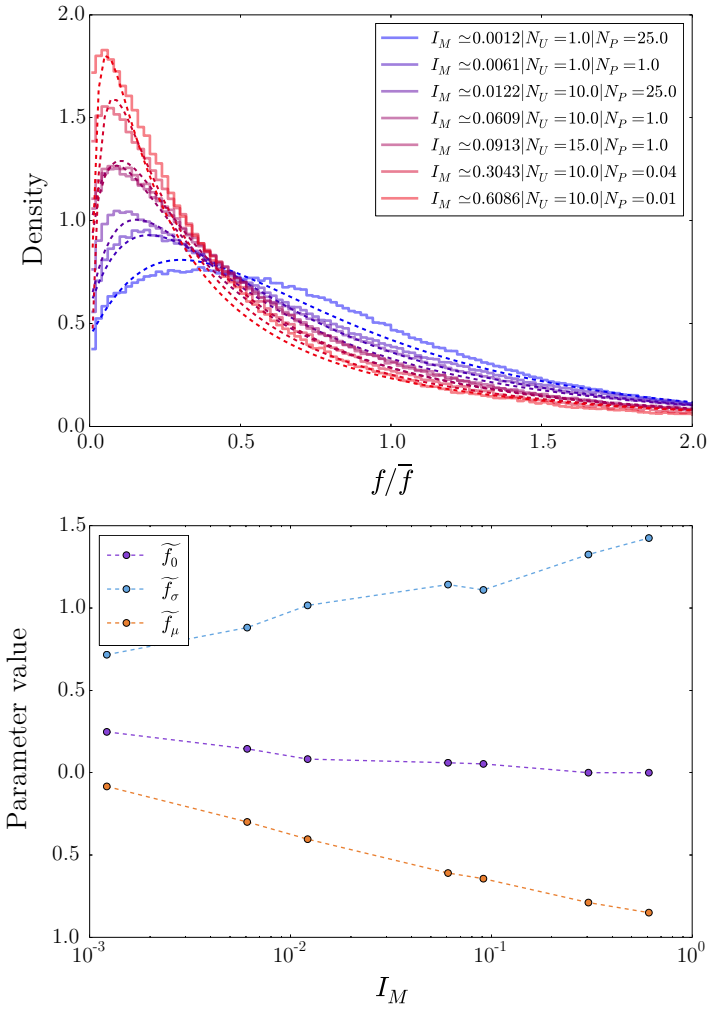

FIGURE 3.11 – Top panel : probability distributions of contact forces for grains in contact with the wall, for different values of I_M ; the dashed lines show a fit by a truncated log-normal distribution (maximizing the likelihood with the Nelder-Mead optimization method). Bottom panel : variation of the parameters of the log-normal distributions as functions of I_M (see Eq.(3.11)).

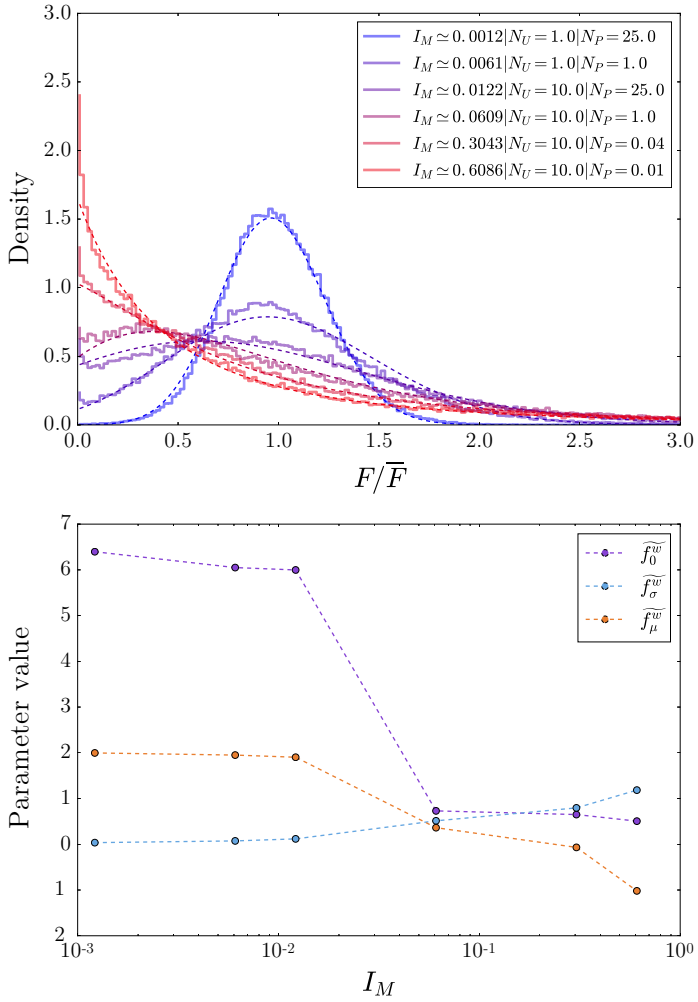

FIGURE 3.12 – Top panel : PDF of the total force on the right sidewall for eight values of I_M ranging from 1.2 10^{-3} to 0.9. A truncated log-normal distribution can be fitted on the data (dashed lines). Bottom panel : the truncated log-normal parameters variation as a function of I_M.

properties of a Gaussian-like distribution and an exponential-like distribution. However, it was impossible to find a way to model the distributions of total force by an analytical form that combines both Gaussian and exponential distributions, over the entire range of I_M tested here. The only PDF that could be fitted to the distributions of the total force on the wall is again the truncated log-normal distribution [see Eq.(3.11)], as shown by the dashed lines drawn in Fig. 3.12.

As for the distributions of $\widetilde{f}$ discussed in Sec. 3.6.1, it would be difficult to give a physical interpretation for the truncated log-normal PDF for the distributions of $\widetilde{F}$. However, it is possible to analyse the evolution of the corresponding parameters with the inertial number. $\widetilde{f_\mu^w}$, $\widetilde{f_\sigma^w}$ and $\widetilde{f_0^w}$ (the scale, shape and local parameters, respectively) are presented at the bottom panel of Fig. 3.12, as a function of I_M. These parameters

follow monotonous paths with I_M, allowing to predict the distribution of the force on the sidewall from the inertial number. This result was further confirmed (with the same set of simulations as in Fig. 3.10) because several distinct dipoles (N_U, N_P) that give the same inertial number systematically led to the same distribution (curves not presented here).

The bottom panel of Fig. 3.12 displays a jump in the parameters of the truncated log-normal distribution between $I_M = 10^{-2}$ and $I_M = 6\ 10^{-2}$. Further looking at the curves on the top panel of Fig. 3.12, this jump occurs when the Gaussian shape almost disappears due to the competition with the exponential shape at low forces, thus displaying an homogeneous repartition (kind of plateau) from $F/\overline{F} = 0$ to $F/\overline{F} = 1$. This significant change (for $I_M \sim 10^{-2}$) of the distribution of the total force on the wall, when the low forces and the mean forces have almost the same probability of occurrence, appears to be an additional marker of the quasistatic to dense inertial transition, concomitant with the total loss of system memory discussed in Sec. 3.5.2.

3.6.3 Force distribution at mesoscale

Because of the heterogeneity of the granular sample induced by the cavity boundary conditions, it is interesting to investigate the force distributions at a mesoscopic scale—smaller than the cavity height and greater than the grain scale, as already done for the force autocorrelation (see Sec. 3.5.2). We note F_i the force time-series on a portion of wall located at a given i, and $\overline{F_i}$ its mean. The top panel of Fig. 3.13 displays the distributions of $F_i/\overline{F_i}$ obtained on ten wall portions of identical size, for $I_M \simeq 10^{-2}$. The distributions corresponding to the portions located in the center of the right sidewall collapse into one single curve, while the distributions measured close to the top and bottom right corners of the cavity differ from this master curve. This result reflects the spatial heterogeneity of the cavity over its height, in connection to three zones : a highly sheared zone of small height at the top, a small dead zone at the bottom and (in between) a flowing zone of much larger height in the center. An identical behaviour (curves not shown here) was observed for all values of I_M. These three zones, extracted from the distributions of $F_i/\overline{F_i}$, are fully consistent with the vertical profile of the time-averaged force measured on the wall, as depicted in figure 5 of our previous study [58]. The time-averaged force was rather homogeneous over the same (large) central zone of the wall. It is worth noting that the sizes of the bottom and top zones may be sensitive to the grain diameter relative to the wall height. Further simulations with different grain diameters would be necessary to study the potential influence on the size of the boundary (top and bottom) zones identified here.

In the following, the collapse of the $F_i/\overline{F_i}$ distributions, excluding the extreme (top and bottom) zones of the wall, is exploited to analyse how the distribution at mesoscale evolves with the macroscopic inertial number. This mesoscale corresponds to a size $H/10 = 3d$.

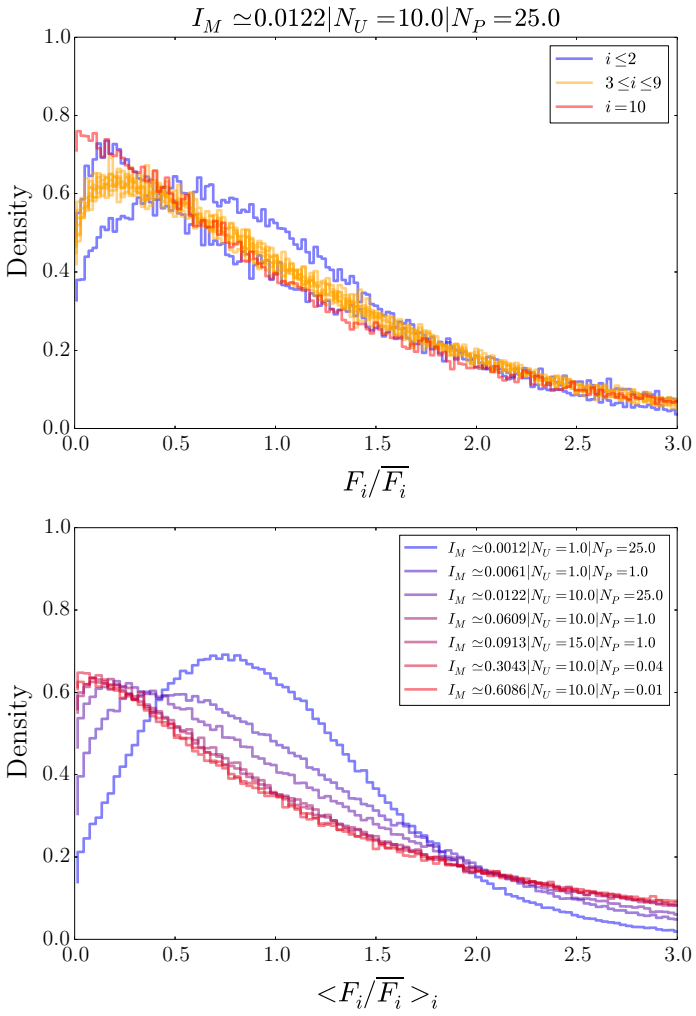

FIGURE 3.13 – Top panel : PDF of force time-series on ten wall portions i for $N_U = 10$ and $N_P = 25$ (each portion time-series is scaled by its corresponding time-averaged force). The blue, orange and red curves respectively correspond to $i \in [1; 2]$, $i \in [3; 9]$ and $i = 10$. Bottom panel : mean distribution over i for $i \in [3; 9]$ (yellow curves of top panel) for seven values of I_M.

The bottom panel of Fig. 3.13 depicts the mean distribution over seven values of $i \in [3;9]$ (corresponding to the central zone of the cavity excluding the top and bottom highly inhomogeneous layers), for a wide range of I_M. As observed for the force distributions at micro- and macroscale presented previously (see Sec. 3.6.1 and 3.6.2, respectively), the curves depict shapes that resemble a truncated log-normal PDF. While comparing the distributions over the wide range of I_M, they appear however to be much closer with each other, meaning they exhibit a weaker dependency toward I_M. It has been verified (curves not shown here) that the distributions at macroscale for the entire wall did remain unchanged if the data near the bottom and top wedges was not considered. The weaker dependency of the distributions to I_M at mesoscale is thus striking, as it cannot be explained by a wedge effect only (this effect would be detected on the macroscale otherwise). As a consequence, it can be concluded that similar mesoscale distributions can result in radically different macroscale distributions through the summation relation that links the forces on wall portions to the force on the entire height of the wall. The latter observation may put emphasis on the crucial role of spatial dependencies between mesoscale force signals, that are controlled by the granular flow regime (through the value of I_M). In particular, the Gaussian-like shapes shown on Fig. 3.12 obtained for quasistatic regimes ($I_M \simeq 10^{-3}$) typically reflect the summation of independent mesoscale force signals. This is consistent with the fact that no spatial correlation was found at the lowest I_M (as detected from the temporal autocorrelation functions at different i shown on the top graph of Fig. 3.8). Conversely, the evolution toward an exponential-like distribution at intermediate inertial numbers ($I_M \gtrsim 10^{-2}$) on Fig. 3.12 reveals a spatial dependency between the mesoscale force signals. This is consistent with the spatial correlation detected between the temporal autocorrelation functions at different i shown in the mid graph of Fig. 3.8.

At $I_M \simeq 10^{-3}$, the distribution displays a small amount of low forces and a nearly Gaussian repartition centered at about $0.7\overline{F_i}$. Then, with the increase of I_M, all distributions quickly converge to an exponential-like decrease with a high number of low forces. Finally, the force distribution on wall portions become independent of I_M as soon as $I_M \gtrsim 10^{-2}$ and $i \in [3;9]$. This result allows once again the identification of a clear signature of the transition from quasistatic to dense inertial granular flow regime for the cavity system studied here.

3.7 Discussion and conclusion

3.7.1 Time-averaged dynamics

The analysis of the time-averaged dynamics in section 3.4 highlighted the crucial role played by the $\mu(I)-$rheology (proposed by [44, 52]) in the granular force transmission

toward a boundary wall. To further confirm it, we have analysed the slight variation of the height H of the cavity system. Up to now, a constant volume fraction $\Phi = 0.6$ close to random close packing has been considered. The cavity system defined in our study is by construction a volume-free system, meaning that the volume fraction inside the cavity may vary. Indeed, though the variation of volume fraction of the granular bulk was small, one could measure it. The top graph of Fig. 3.14 displays how the volume fraction Φ_*, actually measured in our DEM simulations, evolved with the boundary macroscopic inertial number I_M. We observe a plateau (constant Φ_*) at the lowest I_M, followed by a slow decrease of Φ_* with $\log(I_M)$. This slight dilatancy of the granular bulk while increasing the inertial number is a robust result for a number of volume-free granular systems governed by the $\mu(I)-$rheology, such as plane shear flows [27], free-surface granular flows down inclines [41], annular shear cell flows [36], etc. Finding this dynamic dilatancy law in the lid-driven cavity system studied here further confirms the key role played by the $\mu(I)-$rheology.

Note that the results in the top graph of Fig. 3.14 are shown with two values of both μ and d. A decrease of the interparticle friction coefficient produced a slight increase of Φ_* but did not change the qualitative trend regarding the overall evolution of Φ_* with I_M. The increase of Φ_* with the decrease of the grain diameter d may be explained by some boundary effects at the confining walls of the cavity, which are smoothed for smaller d. The bottom graph of Fig. 3.14 shows how the scaling between $\overline{F}/(PLd)$ and I_M, was influenced by the interparticle friction μ. The values of r_1, r_2 and I_M^0 used for the fitting function are slightly changed when μ is divided by nearly two (see detail in bottom panel of Fig. 3.14). Finally, the particle diameter d has a slight influence on the relation in the quasistatic regime, namely when I_M is below 10^{-2}. The influence of the grain properties (grain diameter, interparticle friction) will merit more attention in the future.

3.7.2 Grain-wall force distributions

As already mentioned in Sec. 3.2, Howell et al. [50] found exponential distributions at the smallest volume fraction while the distributions exhibited a peak at larger volume fraction. Considering the one-to-one relation between I_M and Φ_* shown in Fig. 3.14, the evolution of the distributions with I_M depicted in Figs. 3.11 and 3.12 are in qualitative agreement with the evolution of the distributions with the volume fraction reported by Howell et al. [50] in their 2D granular Couette experiments.

While varying I_M and the spatial scale of interest, the probability distributions of grain-wall forces which we found in the present study (summarized in Fig. 3.15) cover the wide range of shapes discussed in the literature overview proposed in Sec. 3.2. In their two-dimensional granular Couette experiments, Howell et al. [50] compared the distributions at the particle scale to the ones averaged over a great number of particles, and found that

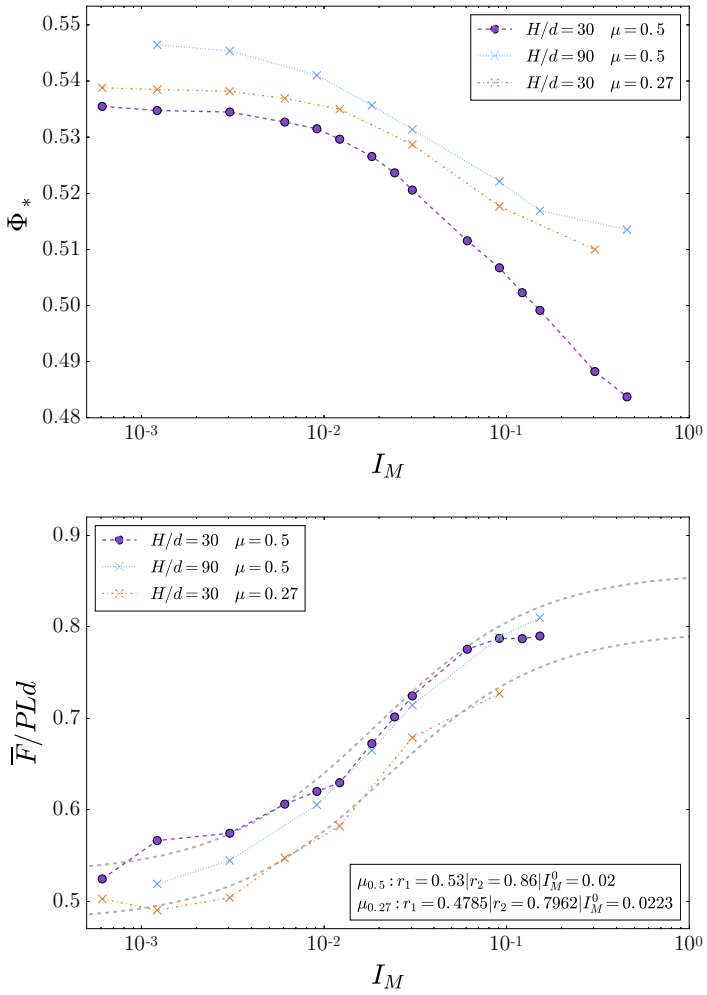

FIGURE 3.14 – Volume fraction Φ_* (top panel) and scaled mean force on the sidewall $\overline{F}/(PLd)$ (bottom panel) actually measured in the numerical simulations, as a function of I_M : $d = 0.001$ and $\mu = 0.5$ (blue curve), $d = 0.0003$ and $\mu = 0.5$ (green curve), $d = 0.001$ and $\mu = 0.27$ (red curve). In the bottom panel, the fits proposed in [58] are drawn to show how μ affects the fitting parameters r_1, r_2 and I_M^0.

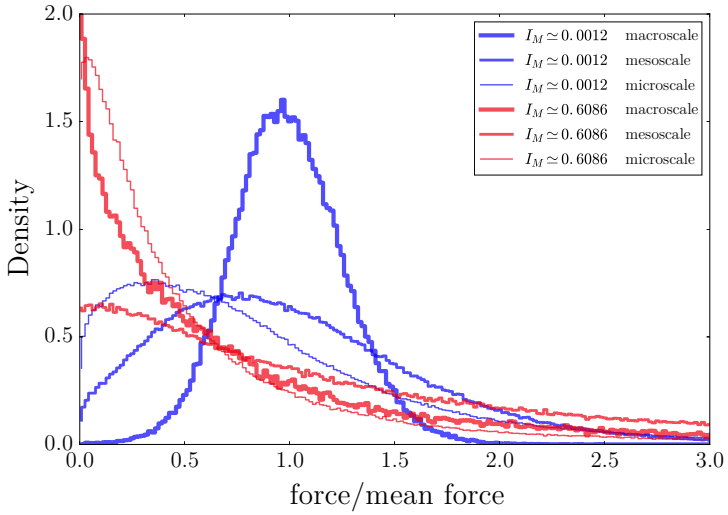

FIGURE 3.15 – PDFs of grain-wall forces at three different spatial scales for two extreme values of I_M.

at large volume fraction the distributions became nearly Gaussian. The latter observation appears to be consistent with the evolution of the distributions for $I_M = 1.2\,10^{-3}$ (largest volume fraction in this numerical study) when the spatial scale is increased, as shown in Fig. 3.15.

A key result of the present study is that the value of the boundary macroscopic inertial number and, to a lesser extent, the spatial scale (macro, micro, or meso) considered, are key inputs that predetermine the grain-wall force distributions. Note that doubling L/H (not shown here) did not change the distributions. All measured distributions could be modeled by truncated log-normal PDFs whose parameters were fully controlled by I_M. This opens a path to being able to predict the grain-wall force distributions over a wide range of I_M.

3.7.3 Quasistatic to dense inertial regime

The analysis of the granular lid-driven cavity problem showed that the macroscopic inertial number I_M fully controlled all the time-averaged quantities (the mean scaled force on the wall, the position of the vortex, and the bulk volume fraction) and the force fluctuations (through the analysis of probability distributions). Moreover, a clear transition was observed at I_M around 10^{-2} in the time-averaged dynamics of the cavity system. This transition was identified by an increase of the scaled steady force, a displacement of the vortex position toward the wall, a loss of symmetry in the $|\mu_{loc} - \mu_{th}|$ maps, and a macroscopic dilation of the granular bulk. The autocorrelation of force time-series at mesoscale allowed to reveal a total loss of system memory (not intrinsic to the material) beyond a value of $I_M \sim 10^{-2}$. Finally, we identified drastic changes in the evolution of the

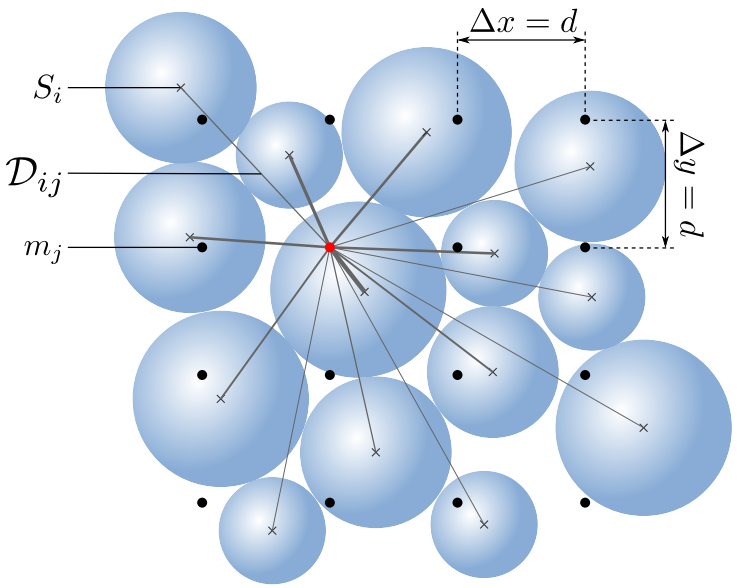

FIGURE 3.16 – Illustration of the kernel smoothing used for regular mesh fields calculations.

shape of probability distributions beyond a I_M once again close to 10^{-2}. All these results are interpreted as a salient signature of the transition from quasistatic to dense inertial flow regime in granular media.

Acknowledgments This work has been partially supported by the LabEx Tec21 (Investissements d'Avenir : grant agreement No. ANR11-LABX-0030). Thierry Faug and Mohamed Naaim are grateful to the financial support by the People Programme (Marie Curie Actions) of the EU 7th FP under REA Grant Agreement No. 622899 (FP7-PEOPLE-2013-IOF, GRAINPACT). François Kneib and Thierry Faug would like to thank Pierre Jop for instructive discussions.

3.8 Appendices

Kernel smoothing As the granular sample is made of discrete particles involving discontinuities, the construction of classical fields often used in continuous mechanics require a particular attention. In this paper, a spacial kernel smoothing is used, as described in Fig. 3.16.

A 2D set of points m_j spaced by d constitutes a regular mesh over the whole cavity. The physical quantities are computed at each mesh point from the particles quantities, according to the particle-point distance. Thus, any (scalar or tensor) quantity Q_i which is associated with each individual sphere S_i can also be associated with all individual mesh points m_j, forming a continuous field. This quantity at the point m_j, noted Q_j, is the

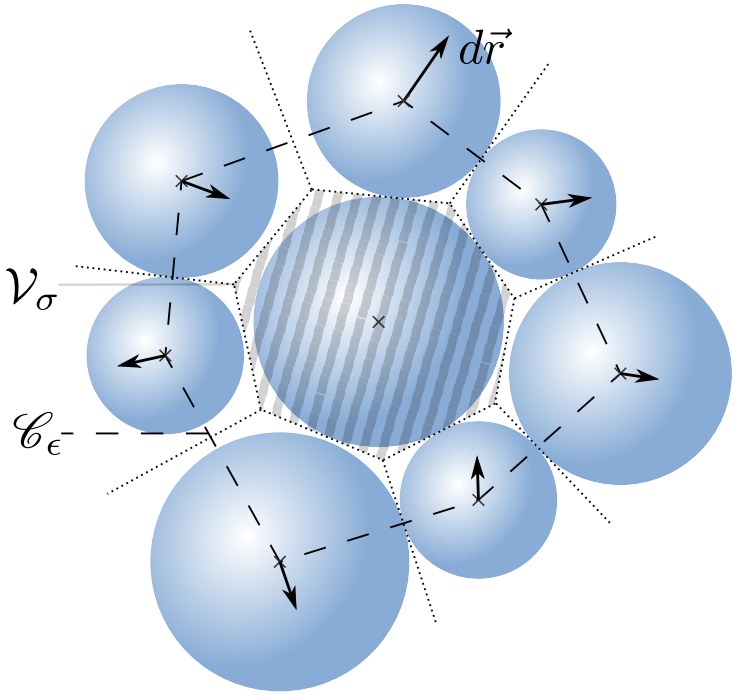

FIGURE 3.17 – Illustration of the tesselation for the per-particle volume calculation.

result of a spacial kernel smoothing with a Gaussian kernel :

$$Q_j = \frac{1}{\sum_i \mathcal{N}(\mathcal{D}_{ij})} \sum_i Q_i \mathcal{N}(\mathcal{D}_{ij}), \tag{3.12}$$

where $\mathcal{D}_{ij}$ are the distances between the spheres centers and the mesh points, and $\mathcal{N}$ is the Gaussian function of mean 0 and standard deviation $d/2$. It is worth noting that the use of a Gaussian kernel is arbitrary and any classical kernel such as a simple rectangular function should not modify the results. The choice of the standard deviation follows the result presented in [107]: the coarse-graining width should be of the order of magnitude of the grains diameter to avoid any oscillation effect and at the same time to limit sidewall effects.

Local stress and strain rate tensors The per-particle stress tensors and strain rate tensors used in the current paper are computed thanks to the algorithms that are part of the YADE-DEM open-source code (see [105] and [19]). The space inside the cavity is discretized with the help of a Voronoï tesselation algorithm, as shown by the dotted lines in Fig. 3.17. In this way, it is possible to compute quantities based on an equivalent continuum of the cavity space. Each sphere is then associated with a list of neighbours forming a bounding polyhedral contour $\mathscr{C}_\epsilon$ with their centroid positions, and a bounding volume $\mathcal{V}_\sigma$ which does not overlap with the neighbours.

Making the assumption that the spheres are at static equilibrium, the following Love-Weber expression can be applied to each sphere in order to compute their associated local

stress tensors based on the contact forces :

$$\boldsymbol{\sigma} = \frac{1}{\mathcal{V}_\sigma} \sum_{c_n} \vec{f_c} \otimes \vec{l_c}, \tag{3.13}$$

where c_n is the ensemble of contacts on the sphere, $\vec{f_c}$ are the contact forces and $\vec{l_c}$ are the vectors linking the sphere center to the contact points.

The local strain rate tensor $\boldsymbol{D}$ is defined as $\boldsymbol{D} = \frac{\boldsymbol{\epsilon}}{\Delta t}$, where $\boldsymbol{\epsilon}$ is the strain tensor computed from two system states shifted by a short lag Δt. For a particular sphere, the displacements of all neighbours during Δt are computed. Then the average displacement gradient $< \nabla d\vec{r} >$ is obtained from the integration of the displacement $d\vec{r}$ along $\mathscr{C}_\epsilon$ (see [19] for more details) :

$$< \nabla d\vec{r} >= \frac{1}{\mathcal{V}_D} \int_{\mathscr{C}_\epsilon} d\vec{x} \otimes \vec{n} ds, \tag{3.14}$$

where $\mathcal{V}_D$ is the volume associated with the contour $\mathscr{C}_\epsilon$, and $d\vec{r}$ is linearly interpolated on the segment between two successive neighbours. Finally, the strain tensor is given by the symmetric part of $< \nabla d\vec{r} >$.

Inertial number and effective friction coefficient The stress tensors $\boldsymbol{\sigma}$ and strain rate tensors $\boldsymbol{D}$ computed according to Sec. 3.8 enable the computation of the spatial fields of inertial numbers I and effective friction coefficients μ_{loc}. The following formulations are the same as described in [10] and are applied at each field point m.

The norm $||\boldsymbol{A}||$ and the deviatoric component $\boldsymbol{A'}$ of a matrix $\boldsymbol{A}$ are defined as :

$$||\boldsymbol{A}|| = \sqrt{\frac{\mathrm{Tr}(\boldsymbol{A}\boldsymbol{A}^{\boldsymbol{T}})}{2}}, \tag{3.15}$$

$$\boldsymbol{A'} = \boldsymbol{A} - \frac{\mathrm{Tr}(\boldsymbol{A})}{3}\boldsymbol{I_3}, \tag{3.16}$$

where $\boldsymbol{I_3}$ is the identity matrix of size 3. The inertial number I and the effective friction coefficient μ_{loc} are :

$$I = d\sqrt{\rho_p}\frac{||\boldsymbol{D'}||}{\sqrt{p}}, \tag{3.17}$$

$$\mu_{loc} = \frac{\mathrm{Tr}(\boldsymbol{\sigma'}\boldsymbol{D'})}{3}\frac{1}{p||\boldsymbol{D'}||}. \tag{3.18}$$

In the above relations, p denotes the pressure that is defined from the decomposition of the Cauchy stress into the isotropic pressure and the deviatoric stress : $\boldsymbol{\sigma} = p\boldsymbol{I}_3 + \boldsymbol{\sigma}'$. Figure 3.18 displays μ_{loc} as a function of I for each point m that belongs to a selected region of the cavity not too close to the boundary walls (see its definition in the caption of Fig. 3.18) and for all simulations of this study—over the whole range of I_M tested. Finally,

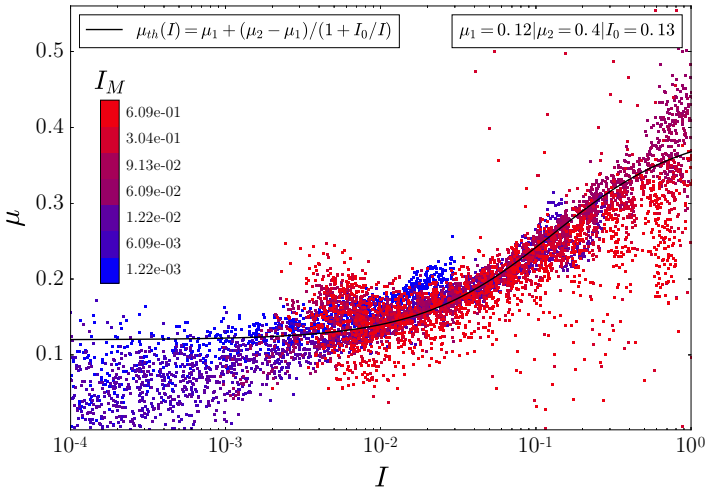

FIGURE 3.18 – Test of the local $\mu(I)-$rheology for all simulations of this study, including all I_M. The points come from a region of the cavity selected to approach the conditions of a simple shear flow. This region corresponds to the upper half region along y that is centered in a band of length $L/2$ along x.

the empirical following form proposed by [52] is used to fit all the points, as drawn by the solid line on Fig. 3.18 :

$$\mu_{th}(I) = \mu_1 + (\mu_2 - \mu_1)\frac{1}{1 + I_0/I}, \tag{3.19}$$

where $\mu_1 = 0.12$, $\mu_2 = 0.40$ and $I_0 = 0.13$. Note that a great number of points falls below μ_1 at low I_M, suggesting that non-locality [54] is present. This point will need further investigation in the future.

Chapitre 4

Force moyenne et fluctuations sur un mur immergé dans un écoulement granulaire cisaillé

Mean force and fluctuations on a wall immersed in a sheared granular flow

Kneib F., Faug T., Dufour F., Naaim M.

In progress.

Abstract The time-averaged dynamics and the force fluctuations in a system composed of a wall-like obstacle subjected to a granular flow under different shearing velocity and confinement pressure are investigated by means of numerical simulations based on the discrete elements method. The mean force on the wall is controlled by the boundary macroscopic inertial number which is derived from the confinement pressure, the shearing velocity and the height of grains sheared above the wall. An empirical law is thus defined to predict the mean force as a function of the boundary macroscopic inertial number, whatever the flow regime and the wall height. The force fluctuations on the wall are characterized by the analysis of the force autocorrelations at mesoscale on the one hand, and by the distributions of grains-wall forces at both macroscale and mesoscale on the other hand. A modified macroscopic inertial number that takes into account a shearing across the whole height of grains is found to fully control the force fluctuations on the wall. The distributions evolve from Gaussian-like shapes to broader asymmetric log-normal shapes with the increase of this macroscopic inertial number. The collapse of all distributions above a certain value of the macroscopic inertial number, and the concomitant loss of system memory revealed by the force autocorrelations, are two indicators of a remarkable transition from quasistatic to dense inertial flow regime. The latter result is further emphasized by a detailed study of the local rheology, showing that the $\mu(I)$ rheological law governs the system in a large part of the granular bulk.

4.1 Introduction

Many industrial processes and geophysical problems involve granular matter at rest or in movement. More specifically, the force exerted on solid objects subjected to flowing granular matter is an important topic that has attracted increasing attention over the recent years. The time-averaged force on objects of different sizes and shapes was studied in various configurations (see for instance [108, 2, 22, 16, 90]). The drag force on immersed solid objects in dense free-surface granular flows was firstly investigated by the experimental work of Wieghardt [108]. In his pioneering experiments, Wieghardt found on the one hand that the drag force was only weakly influenced by the flow velocity, and on the other hand that a quasistatic pile of grains formed upstream the solid object. These

findings were confirmed later in different configurations from low to intermediate shear rates, including annular shear flows [2], free-fall chute flows [22], immersed rods rotating along an axis perpendicular to its main axis [16], etc. All these studies showed that, whenever the obstacle is in contact with a quasistatic bulk of grains, the drag force linearly depends on the confinement pressure and the object size rather than on the flow velocity. This picture is however no longer valid once the granular flows become fast, more dilute and collisional, as shown for instance in [8, 106]. In this situation, it was found that the force acting on the obstacle evolved with the square of the relative grains-object velocity.

A free-surface flow of granular materials down a slope and coming across a perpendicular wall-like obstacle is a common situation in the field of natural hazards related to full-scale gravity-driven granular flows. In particular, protection structures against snow avalanches or landslides are built to limit their propagation through the decrease of their kinetic energy. In this situation, a roughly triangular stagnant zone of grains—a so-called dead zone—is formed upstream the obstacle, and a more inertial zone made of flowing grains can overcome the dead zone (see [38] and references therein). In-situ force measurements of snow avalanches against a square plate were conducted by Thibert et al. [100], Berthet-Rambaud et al. [7], and Baroudi et al. [5]. The time series signals systematically display complex shapes. After a fast rise, the force reaches a peak, and then decreases to a plateau. The latter plateau reflects a permanent regime, disturbed by high amplitude and high frequency fluctuations. A full prediction of the entire force time series remains challenging due to measurement issues and the complex rheology of granular materials. Faug et al. [40] proposed a rich semi-analytic model able to predict the average force on a wall-like obstacle in steady regime. It is based on the mass and momentum conservation equations applied to a control-volume corresponding to the dead zone plus the overflowing inertial zone. This model has the particularity to take into account the length of the dead zone. Such a model was extended with some success to transient flows that mimic natural avalanche-flows [20, 39]. However, while this model (based on conservation equations in their depth-averaged form) predicts well the force signals smoothed over time, it does not handle the fluctuating component which remains poorly documented in this flow-obstacle configuration. The overarching aim of the present paper is to analyse force fluctuations experienced by a wall facing a sheared granular flow.

Most studies dedicated to force fluctuations in granular materials concerned quasistatic or slowly sheared systems, in Couette-like geometries (see [1, 45, 26]). Only a few number of papers addressed the problem of force fluctuations for rapid granular flows. The experiments were based on the discharge of silos equipped with a force sensor, at a boundary wall, whose size was the typical size of the grains [62, 42]. The measurements of contact force distributions in quasistatic or slowly sheared systems were initially computed with the help of carbon paper placed at a system boundary [69], but the use of photo-elastic disks in laboratory experiments, as well as numerical modelling, opened the

path to measuring the contact forces inside the granular bulk. Some cross-comparisons were performed in [80, 95, 96, 76], showing that—at least in the static case—the grain-grain contact force distributions from the bulk were identical to the grain-wall contact force distributions. A robust result concerns the shape of the contact forces f distributions for values greater than the mean $\overline{f}$: they decrease exponentially up to the highest values of f (see for instance [61, 62, 81]). This behaviour is sensitive to the shear velocity (or the deviatoric stress tensor in static cases), as the inertia tends to broaden the distributions (see [62, 96, 45]). For the lowest forces ($f < \overline{f}$), different behaviours depending mostly on the sample history are observed from vanishing to very high probabilities near $f = 0$. Some empirical or theoretical models were proposed to fit the entire range of observed distribution shapes for quasistatic systems [69, 67, 78].

A few studies tackled the distributions of forces that were integrated through a spatial dimension, for slow to intermediate flow rates. It means that the data sets were systematically recorded on surfaces that were greater than the grain size. The configurations tested were the Couette geometry [67, 50, 45], as well as a rotating immersed rod [97]. A remarkable trend emerged from all these studies : while increasing the spatial scale considered, the exponential force distributions narrow and finally move toward Gaussian-like distributions. The latter result is especially pronounced for very slow flows, whereas intermediate shear rates result in exponential to log-normal shapes.

The present paper is dedicated to the numerical modelling of the force exerted on a wall-like obstacle immersed in a sheared granular flow. The originality of this work is the wide range of flow regimes investigated, from nearly quasistatic to collisional flows, through dense inertial flows. In order to control the flowing conditions and to focus on the grain-wall interactions, an innovative planar and gravity-free system is designed. While the spherical grains are trapped across the vertical direction between two rough walls, a periodic boundary condition is used in the horizontal direction. The obstacle is a wall which is fully immersed in the granular bulk and orthogonal to the shearing direction. First, the modelled system (boundary conditions, relevant macroscopic parameters), as well as the numerical simulations based on the discrete element method, are described in Sec. 4.2. Then, the mean (time-averaged) dynamics in terms of velocity fields, scaling of the mean force experienced by the wall, and spatial maps of the local $\mu(I)-$rheology, is analysed in Sec. 4.3. The fluctuations are quantified through both the autocorrelation of mesoscopic force signals associated with the system memory (Sec. 4.4), and the distributions of force time series at macroscopic and mesoscopic spatial scales (Sec. 4.5.1). The effect of the system length relative to its height is discussed in Sec. 4.6, before concluding the paper with an extended discussion on the main results and perspectives (Sec. 4.7).

4.2 DEM simulation of the wall immersed in a granular flow

4.2.1 Macroscopic boundary conditions

A planar sample of spheres is confined between two walls at the top and the bottom, and by a periodic boundary condition linking the right and the left borders of the system, as depicted by the vertical dashed lines in Fig.4.1. The bottom wall is fixed, rough, and its length is equal to the system length L. A constant macroscopic pressure P is applied to the system. It is controlled by the vertical position of the rough top wall, continuously computed by the DEM algorithm and applying a vertical force on the sample. The periodicity of the system also concerns the top wall which has a constant horizontal velocity U shearing the sample. The top wall remains perfectly horizontal by preventing its rotation in the (x, y) plane (see Fig.4.1). The roughness of these walls is made of fixed aligned spheres that are identical to the ones forming the granular medium. A thin and smooth vertical wall of finite height h, namely the obstacle, is immersed into the spheres assembly. The spheres are initially deposited under gravity to form a rectangular dense packing of height H greater than h. Then, the gravity is set off and the shearing starts for a period of ten seconds over which the data are collected. Only the data arising from the latest nine seconds are exploited because the first second is the observed time needed by the system to reach a permanent regime. In the present system, the grains are allow to overflow the obstacle (by contrast to the lid-driven cavity problem studied in [58]), thus mimicking a granular flow passing over a rigid wall.

The following dimensionless macroscopic parameters are used to run the numerical simulations over a broad range of confinement pressure P and shear velocity U :

$$N_P = \frac{P}{\Phi \rho_p g H}, \tag{4.1}$$

$$N_U = \frac{U}{\sqrt{gd}}. \tag{4.2}$$

The mean grain diameter d was taken equal to 1 mm and $H/d = 30$, and a slight polydispersity was introduced by picking randomly the grain diameters between $0.85d$ and $1.15d$. A constant macroscopic volume fraction $\Phi = 0.6$ is considered in these two definitions, as it roughly corresponds to the random close packing of a three-dimensional assembly of spheres. We will discuss in more detail the mean volume fraction of the granular sample in the concluding section of the paper (Sec. 4.3). The particle density was taken equal to $\rho_P = 2500$ kg m^{-3}, and although the system is gravity-free, the gravity acceleration is considered here ($g = 9.81$ m s^{-2}) for convenience to compare the results with laboratory experiments in a future work.

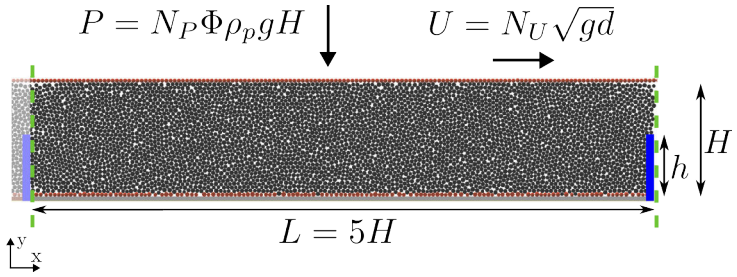

FIGURE 4.1 – Geometry and boundary conditions of the periodic sheared system simulated by DEM. The granular sample is trapped between two horizontal walls and a periodic boundary condition in the horizontal $x-$direction (dashed lines). The top wall applies the shear displacement U and the confinement pressure P (see text for details), and force measurements are done onto the sidewall of height h, immersed into the granular sample.

The boundary macroscopic inertial number I_M can be defined from the typical time associated with the top confinement pressure $t_P = d\sqrt{\rho/P}$ and the typical time equal to the inverse of the macroscopic shear rate $t_U = H/U$:

$$I_M = \frac{t_P}{t_U} = \frac{d\sqrt{\rho/P}}{H/U}, \tag{4.3}$$

where $\rho = \Phi\rho_P$ holds for the density of the granular sample.

In the present study, N_P ranged from 0.01 to 100 and N_U from 1 to 20, which allows to investigate a wide range of granular flow regimes defined by I_M ranging typically from $1.2\ 10^{-3}$ to $6\ 10^{-1}$.

The length of the periodic cell relative to the initial height of the sample, L/H, is a parameter that may also influence the system dynamics. It has been shown by similar DEM simulations on another system, namely the lid-driven cavity (see details in [58, 59]), that the mean dynamics and the force fluctuations are no longer dependent on L/H as soon as $L/H > 5$. In this paper L/H is taken equal to 5 unless otherwise specified, and the sensitivity of the results to L/H will be discussed in detail in Sec. 4.6.

Simulations with various obstacle heights ($h \in \{5d, 10d, 15d, 20d\}$) were performed to analyze the influence of this parameter on the time-averaged results.

4.2.2 Micromechanical parameters

The discrete elements method, the contact laws and the associated parameters used in this paper are the same as described in [58]. The general DEM algorithm is described in [28]. A visco-elastic contact law is used for the normal component of the inter-particle forces (see [88]), while a classical coulomb friction threshold drives the tangential component in the same fashion as in [64]. The following set of equations describes the micromechanical

model used in the present study, for the grain-grain and the grain-wall interactions :

$$\begin{cases} \boldsymbol{F_n} = \max(0, k_n\delta_n + c_n\dot{\delta}_n)\boldsymbol{n}, \\ d\boldsymbol{F_s} = (k_s\dot{\delta}_s dt)\boldsymbol{s}, \\ |\boldsymbol{F_s}| \leq \mu|\boldsymbol{F_n}|, \end{cases} \tag{4.4}$$

where $\boldsymbol{n}$ and $\boldsymbol{s}$ are the unity vectors along the contact normal and shear directions respectively, k_n and k_s are the normal and tangential contact stiffnesses, δ_n is the normal penetration depth, $\dot{\delta}_s$ is the tangential displacement increment, μ is the local friction coefficient, c_n is the normal viscosity coefficient and dt is the time-step. The four physical parameters k_n, k_s, c_n and μ, are chosen to fit the behaviour of glass beads. As discussed in [40] the contact stiffnesses are reduced to decrease the total time of calculation, but the limit of rigid grains was respected with the help of an adimensional number $N_0 = 1.5\ 10^4$. For two grains of same size, k_n was thus set regarding the macroscopic pressure and N_0 : $k_n = N_0 Pd$, and k_s was set with a poisson ratio $\nu = 0.3 : k_s = \nu k_n$. c_n is set in the same manner as in [58] with a restitution coefficient $e = 0.5$, and μ was taken equal to 0.5.

In accordance with the motivation of this study—i.e. the force fluctuations experienced by an obstacle immersed in a granular flow, the current paper is mainly focused on $F(t)$, the normal force time-series exerted on the vertical sidewall over a broad range of I_M. Before going into the details of the force fluctuations (see Secs. 4.4 and 4.5), the time-averaged dynamics of the system (mean force $\overline{F}$ on the wall, streamlines, vertical velocity-profiles and local $\mu(I)-$rheology within the granular sample) is studied in the next section.

4.3 Mean dynamics

4.3.1 Velocity field

The time-averaged granular flow velocity streamlines are displayed on Fig.4.2 for three different inertial numbers I_M and one obstacle height $h = 20d$. The norm of the local grain velocity v_g scaled by the top wall shearing velocity U is displayed on the colour scale. For all simulations the flow velocity fits the top and bottom boundary conditions, ranging from zero near the bottom to U in the vicinity of the top wall. At low inertial numbers ($I_M \simeq 1.2\ 10^{-3}$) the flow velocity shows a symmetric pattern along the system length. Near both corners at the bottom of the system, very low flow rates take place in front of the obstacle—likely at the origin of the streamlines instabilities. They are the markers of nearly triangular dead zones of height h forming near the obstacle and gradually disappearing while moving farther from the obstacle. In a central region ($50d \lesssim x/d \lesssim 100d$) the streamlines are horizontal and parallel with each other, revealing that the flow experiences a quasi-horizontal shear without any significant vertical displacement. Back to past studies on free-surface gravity-driven granular flows passing over a rigid wall

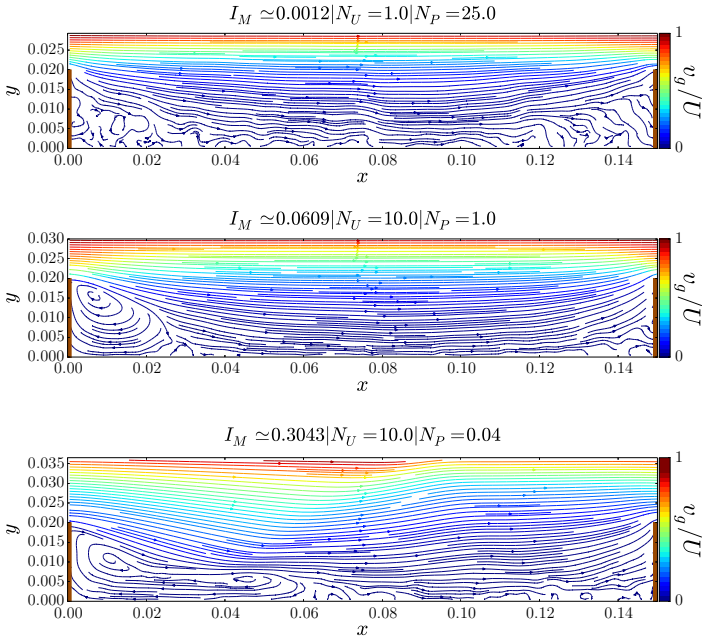

FIGURE 4.2 – Time-averaged streamlines for an obstacle height of $h = 20d$ (thin vertical bars on each border of the system), for three different values of I_M : $I_M = 1.2\ 10^{-3}$ (top panel), $I_M = 6.09\ 10^{-2}$ (middle) and $I_M = 0.3043$ (bottom). The colour scale represents the norm of the local grain velocity scaled by the top wall shearing velocity, v_g/U.

[40, 20, 39, 38], the latter homogeneous region mimics the incoming flow, co-existing with a similar (nearly triangular) dead zone formed upstream the obstacle (the wall on the right side).

However, the response of the system velocity streamlines to the increase of I_M is tricky. While the top panel at the lowest I_M exhibits a symmetric pattern, the middle and the bottom panels of Fig.4.2 display different behaviours. As the obstacle is also duplicated through the periodic boundary condition along x, a local vortex of height h starts forming on the left side of the system. In the present context, this phenomenon is considered as an artifact caused by the grains flowing through the periodic boundary condition and incoming with high velocity from the top of the vertical left sidewall. The shape of this vortex varies with the macroscopic boundary conditions. In particular, the vortex length increases with I_M, disturbing progressively the above picture of the central region where shear is quasi-horizontal. The latter region becomes narrower when increasing I_M, and may totally disappear at the largest I_M. This peculiar feature of the periodic flow-obstacle system studied here is further investigated in the following paragraph, focusing on the vertical velocities of grains.

Figure 4.3 depicts the vertical component V_y of the grain velocity along the system length, averaged over time and height, and scaled by the top wall shearing velocity U. This measurement is presented for seven values of inertial numbers, from quasistatic to

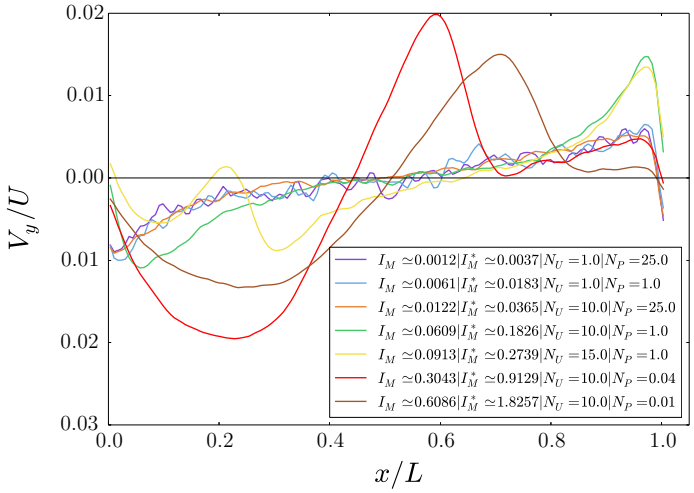

FIGURE 4.3 – Profile of the vertical component of the grains velocity V_y, averaged over time and grains height H, scaled by the top wall shearing velocity U. The profile is plotted for an obstacle height h of $20d$ and seven values of I_M from $1.2\ 10^{-3}$ to 0.6.

collisional flow regimes.

For $I_M \leq 1.2\ 10^{-2}$ all profiles collapse, revealing that the global (scaled) grain velocity is not influenced by the macroscopic conditions in the quasistatic regime. Near the (left side) incoming flow region ($x/L < 0.3$), V_y is negative with a high slope gradient, induced by the grains that continuously fill the bottom of the system. Between $x/L = 0.3$ and $x/L = 0.85$, V_y/U is nearly close to zero with only a very small positive slope gradient. This region, which we call a plateau, characterizes the homogeneous sheared zone described just above. Finally, from $x/L = 0.85$, the increase of the slope gradient marks the presence of the dead zone formed upstream of the obstacle (on the right side) overflowed by the grains. The presence of a plateau in the center of Fig. 4.3 is a sign that the system length should be large enough to guarantee that the flowing direction of the granular assembly is orthogonal to the obstacle. Thus—if non-local effects do not play a prevailing role, the force exerted on the obstacle should not be influenced by its periodic duplicate (on the left side). The effect of increasing L/H (fixed to 5 here) will be discussed in Sec. 4.6.

As shown at the middle and bottom panels of Fig.4.2, the vortex formed in the left side of the system produces vertical movements of the granular flow that are inhomogeneous through the system height for simulations done with $I_M \geq 6.09\ 10^{-2}$. As a consequence, the averaging over height done in Fig.4.3 to obtain the V_y/U profile for the corresponding inertial numbers cannot be quantitatively interpreted. Qualitatively, the plateau is still observed up to $I_M = 9.13\ 10^{-2}$ but the two curves obtained for the largest I_M ($I_M \geq 0.3$) are highly disturbed by the vortex, thus preventing the occurrence of the plateau in the collisional regime. We will show in Sec. 4.6 that increasing L/H does not change this observation : it is not possible to produce a plateau for $L/H = 10$ at high inertial numbers.

This flow inhomogeneity along the main flow direction ($x-$axis direction) observed for high I_M makes difficult, in the collisional regime, the direct comparison of this system to free-surface gravity-driven granular flows passing over a wall. The influence zone downstream of the duplicate obstacle (on the left side of the periodic system) is too long so that it disturbed the granular kinematics in the whole volume of the system up to the obstacle (on the right side) of interest here. However, it will be shown in the following of the paper that an analysis of the force (time averaged value and fluctuations) experienced by the latter obstacle can be done continuously, over the whole range of I_M covered by this study. In particular, a robust scaling of the mean total force exerted on the obstacle is proposed in the next section.

4.3.2 Mean force on the obstacle

The main feature of the present system is that the height H of the granular sample is higher than the height h of the obstacle, by contrast to the lid-driven cavity problem in [58]. As a consequence the following flow dynamics can be observed : grains are trapped upstream the obstacle (the right sidewall), thus forming a dead zone, and other grains are able to flow over the obstacle, as discussed in Sec. 4.3.1. Based on the height $H - h$ of the sheared layer passing over the obstacle, a new macroscopic inertial number I_M^* can be defined :

$$I_M^* = \frac{d\sqrt{\rho/P}}{(H-h)/U}. \tag{4.5}$$

In the above definition, the dead zone is assumed to cover the entire height of the wall. The grains passing over the wall are sheared between the top wall of vertical position H on the one hand, and the top of the dead zone of null velocity and height h on the other hand. Introducing this macroscopic inertial number allows us to obtain a remarkable scaling of the mean force $\overline{F}$ on the obstacle, scaled by the pressure force Phd associated with the wall height, as a function of I_M^*, as shown in Fig.4.4.

A collapse of all the data is observed, including four obstacle heights $h \in \{5d, 10d, 15d, 20d\}$. This result reveals that the shearing velocity and the top pressure can be wrapped into a macroscopic inertial number which predicts the scaled mean force on the sidewall. It is enhanced by the construction of I_M^*, showing that the inertial number corresponding to the grains overflowing the sidewall plays a crucial role in the force applied on the obstacle.

The scaled mean force, $\overline{F}/(Phd)$, shows a quasi-linear evolution with I_M^* at low and intermediate I_M^*. Though a scattering of the data appears at high I_M^*, a saturation then occurs from around $I_M^* = 0.3$ (see the linear plot in the inset of Fig. 4.4). The following relation fits well the data points, as shown by the solid line drawn on Fig. 4.4 :

$$\frac{\overline{F}}{Phd} = r_1^* + \frac{r_2^* - r_1^*}{1 + \frac{I_M^{*0}}{I_M^*}}, \tag{4.6}$$

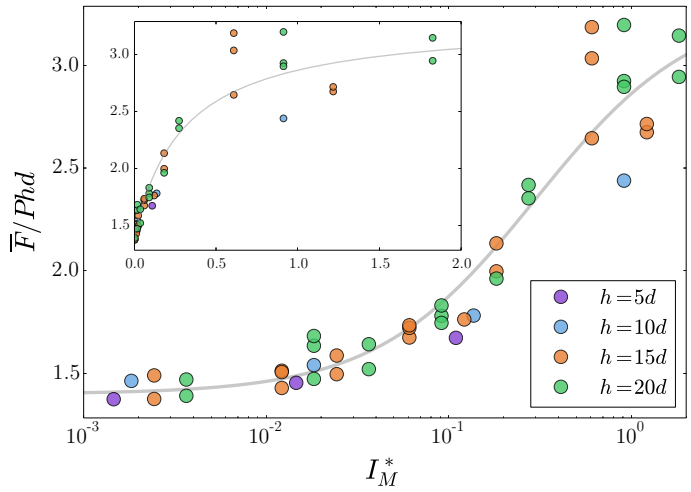

FIGURE 4.4 – Time-averaged force on the obstacle $\overline{F}$ scaled by Phd as a function of I_M^*, the inertial number corresponding to the height of grains overflowing the obstacle. Four obstacle heights are presented : $h \in \{5d, 10d, 15d, 20d\}$. Inset : same data with linear x-axis scale.

where $r_1^* = 1.4$ and $r_2^* = 3.3$ are the two asymptotic values of $\overline{F}/(Phd)$ at low and high I_M^*, respectively. The constant $I_M^{*0} = 0.3$ is the inertial number for which $\overline{F}/(Phd) = (r_1^* + r_2^*)/2$. It is worth noting that the values of r_1^*, r_2^* and I_M^{*0} were obtained for the configuration presented in this paper, and may be influenced by the micromechanical grain parameters (d, μ, etc.), as well as by the system configuration. In particular, the effect of L/H on the mean force scaling shown in Fig. 4.4 will be discussed in Sec. 4.6.

It is worthwhile to note that the data saturation (concomitant with some scattering) and the plateau which vanishes in the mean V_y profiles (see Sec. 4.3.1) both occur at $I_M^* \simeq 0.3$. This observation is a signature of the transition from the dense inertial regime to a more collisional regime, where enduring frictional grain-grain contacts are replaced by short-life contacts due to the strong increase of the inertia and the increase of the mean free path of particles. The role played by the local $\mu(I)-$rheology, proposed by [52, 44], on the force transmision toward the wall-like obstacle is further analysed below.

4.3.3 The local $\mu(I)-$rheology

The form of the empirical scaling showing a one-to-one relation between the scaled mean force $\overline{F}/(Phd)$ on the wall and the boundary macroscopic inertial number I_M^*, given by Eq. (4.6), suggests that the local $\mu(I)-$rheology comes into play. To further investigate the rheology, the time-averaged values of the local inertial number I and the local effective friction μ_{loc} were measured inside the whole volume of the granular system.

For that purpose, the strain ($\boldsymbol{D}$) and stress ($\boldsymbol{\sigma}$) tensors at local (grain) scale were computed, using a spatial kernel smoothing method and tesselation techniques (see much

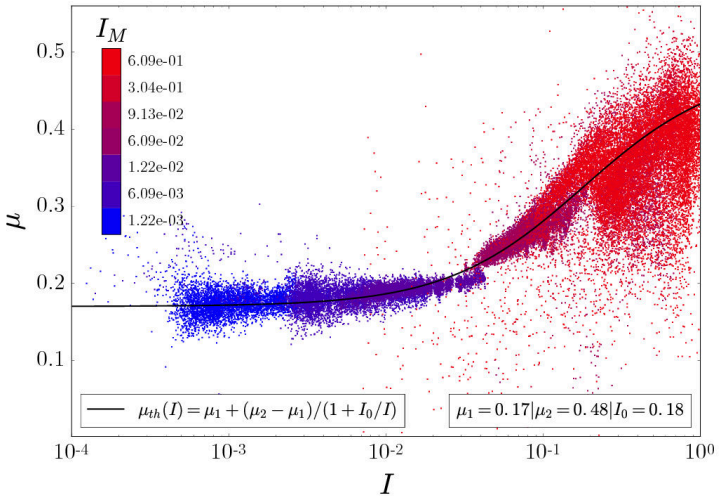

FIGURE 4.5 – The local $\mu(I)-$rheology for this study, extracted from all simulations. The points come from a region of the granular flow-wall system selected to approach the conditions of a simple sheared granular sample.

more details in [59]). The pressure p within the granular medium was defined by :

$$p = \frac{1}{3}\mathrm{Tr}(\boldsymbol{\sigma}). \tag{4.7}$$

The local effective friction was calculated as :

$$\mu_{loc} = \frac{1}{3}\frac{\mathrm{Tr}(\boldsymbol{\sigma'}\boldsymbol{D'})}{p\|\boldsymbol{D'}\|}, \tag{4.8}$$

where $\boldsymbol{D'} = \boldsymbol{D} - \frac{1}{3}\mathrm{Tr}(\boldsymbol{D})\boldsymbol{I_3}$ holds for the deviatoric strain tensor and $\boldsymbol{\sigma'} = \boldsymbol{\sigma} - p\boldsymbol{I_3}$ is the deviatoric stress tensor. We define $\boldsymbol{I_3}$ as the unit tensor and $\|\boldsymbol{A}\| = \sqrt{\mathrm{Tr}(\boldsymbol{A}\boldsymbol{A}^T)/2}$ for any $\boldsymbol{A}$. Finally, the local inertial number was computed using the relation :

$$I = d\sqrt{\frac{\rho_P}{p}}\|\boldsymbol{D'}\|. \tag{4.9}$$

Then, for each position (x, y), the measured μ_{loc} was compared to a $\mu_{th}(I)$ derived from the relation proposed by Jop et al. [52], which reads as follows :

$$\mu_{th} = \mu_1 + (\mu_2 - \mu_1)\frac{1}{1 + I_0/I}, \tag{4.10}$$

where μ_1, μ_2 and I_0 are parameters dependent on the mechanical grain properties. In our study, we found that the best fitting parameters for μ_{th} were $\mu_1 = 0.17$, $\mu_2 = 0.48$ and $I_0 = 0.18$, as shown in Fig. 4.5.

Figure 4.6 displays the spatial maps of $|\mu_{loc} - \mu_{th}|$ for three values of I_M. First, it is generally observed that the granular sample obeys the local $\mu(I)-$rheology in most of the volume of the granular system, except in the regions close to the sidewalls in the two

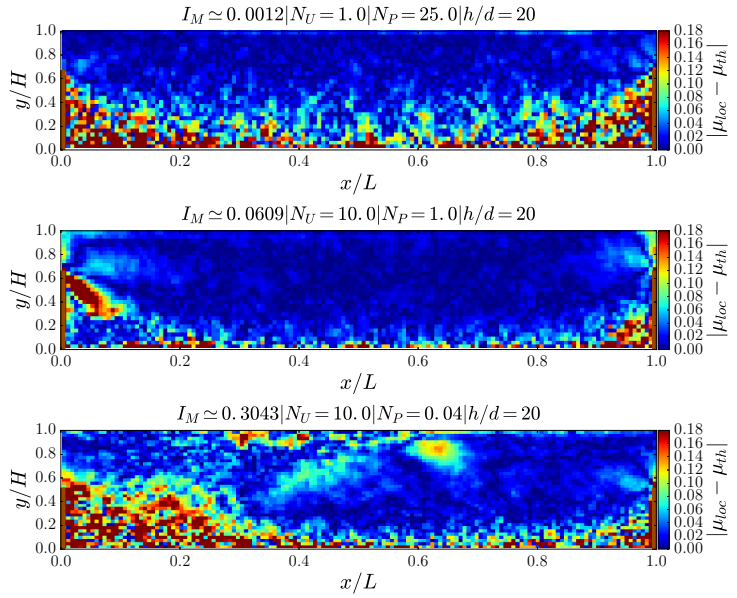

FIGURE 4.6 – Spatial maps of $|\mu_{loc} - \mu_{th}|$ for three values of I_M : $I_M = 1.2\ 10^{-3}$ (top panel), $I_M = 6.09\ 10^{-2}$ (middle) and $I_M = 0.3$ (bottom). See text for the definition of μ_{loc} and μ_{th}.

corners at the bottom of the system. Second, at low I_M the patterns resulting from this $|\mu_{loc} - \mu_{th}|$ mapping is symmetric, while it becomes asymmetric at the highest I_M. At the highest I_M, the region in the left corner at the bottom, in which the measured μ_{loc} discards from the μ_{th} derived from the $\mu(I)-$rheology, grows in size and tends to extend in the middle of the granular system. Those observations are fully consistent with the streamlines shown in Fig. 4.2. The regions with a dead zone (whatever I_M) correspond to regions where the granular material does not obey the $\mu(I)-$rheology.

Back to the analogy with gravity-driven free-surface flows passing over a wall (as studied in [40, 20]), our study reveals that the incoming flowing grains able to overtop the wall would obey the $\mu(I)-$rheology, while the grains trapped inside the dead zone (upstream of the wall) would not. The deviation from the $\mu(I)-$rheology can thus help to demarcate the dead zone from the coexisting (more inertial) flowing zone above.

The region (in the left corner at the bottom), where a vortex-like structure forms at high I_M, grows in size with I_M and also corresponds to a region where the granular medium does not obey a $\mu(I)-$rheology.

From now on, the paper tackles the force fluctuations on the obstacle, through analysing the autocorrelation of force time-series (Sec. 4.4) and the distributions of grain-wall contact forces (Sec. 4.5). All data obtained for the next analysis was extracted from numerical simulations with an obstacle height $h = 20d$. Keeping the obstacle high enough to catch collective effects of the grains (in order to avoid discretization issues), while the height available for the grains to overflow is one third of the total height H of the sample, made the results clearer. The results extracted from the simulation with $h/d = 5$, 10 or

15 (not shown here) were very similar overall.

4.4 Force time-series autocorrelation

In this section, the force fluctuations are investigated by analysing the autocorrelation of force time-series on portions i of the wall. Information about the *memory of the system* (we will define below what we call memory of the system) is then extracted through a critical autocorrelation time Δt_c^i.

The force signal record frequency is set to 10 kHz, this value being high enough to capture short-time events so that the results do not depend on this parameter (see more detail in [59]). To study the potential heterogeneity of the force signals along the obstacle height, the sidewall is split into five portions $i \in \{1, 2, 3, 4, 5\}$ from bottom to top, of identical size $h/5$. Each slice has its associated force time-series from which the autocorrelation function $\mathcal{C}^i(F(t), F(t + \Delta t))$ is then computed, where Δt is the lag between two system states. The critical correlation time Δt_c^i is extracted from each slice. It can be interpreted as the delay after which the system has forgotten a certain value of force on the wall. In other words, it reflects the typical time during which a future state of the system keeps history of its past state regarding the force transmitted to the wall. The critical correlation time Δt_c^i is defined with an arbitrary low correlation threshold :

$$\mathcal{C}^i \left(F(t), F(t + \Delta t_c^i) \right) = 0.15. \tag{4.11}$$

As the local autocorrelation function $\mathcal{C}^i$ may be a non-monotonic function, it is possible that the threshold value is reached many times. In this case the lowest value of Δt_c is kept, avoiding the noise to have an influence on the results.

The top panel of Fig. 4.7 shows the autocorrelation of force time-series for each of the five identical portions of the wall, for a low value of the macroscopic inertial number ($1.2\ 10^{-3}$). For this granular regime, the autocorrelations decrease slowly to reach a vanishing value between approximatively 0.2 s to 1.5 s, depending on the wall portion considered. Although an observable trend suggests that bottom portions are correlated for longer times (lower slopes) than top portions (higher slopes), no general rule could be deduced, because this behaviour is not strictly monotonic.

The values of autocorrelation times Δt_c^i for each portions of the wall, as well as their mean over i—called $<\Delta t_c>$, are displayed on Fig.4.7. A scattering of the Δt_c^i-values around $<\Delta t_c>$ is observed, showing that autocorrelation times are inhomogeneous along the height of the sidewall height. However, the average value $<\Delta t_c>$ shows a remarkable decreasing trend with I_M. This behaviour may be interpreted as a decrease of the system memory while increasing the inertial number, which is in accordance with a collisional regime where short-life contacts are dominant compared to long-lasting enduring frictional

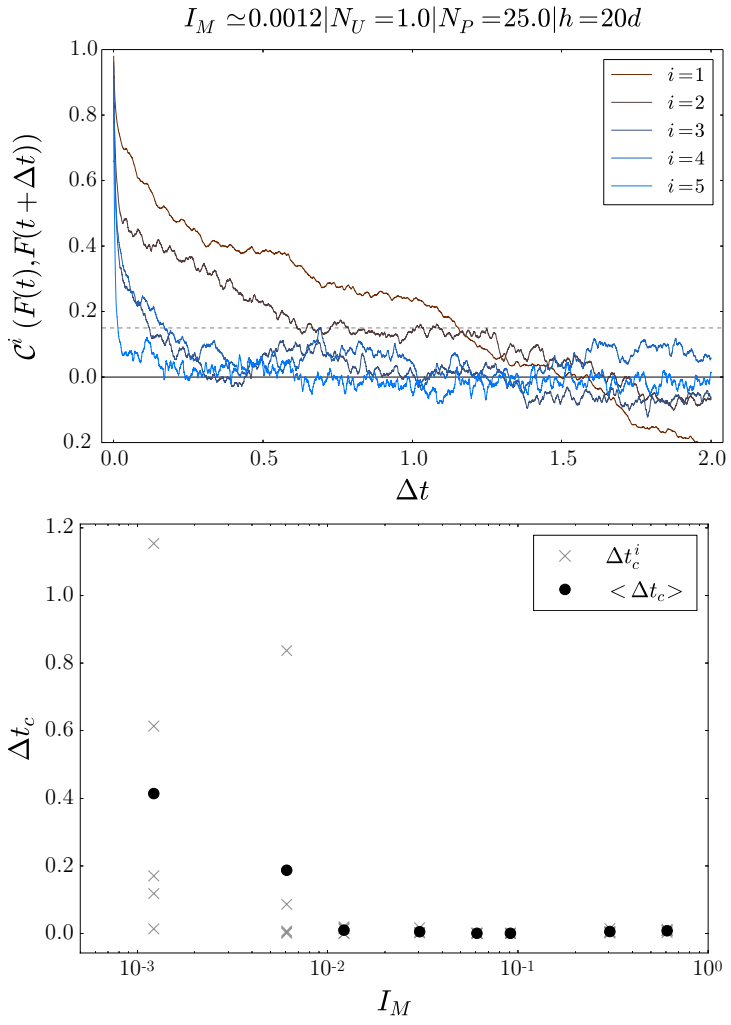

FIGURE 4.7 – Top panel : evolution of $\mathcal{C}^i(F(t), F(t+\Delta t))$ over time for five identical portions of the wall height $i \in \{1, 2, 3, 4, 5\}$ from bottom to top, and $I_M = 1.2\ 10^{-3}$. The grey dashed line is the threshold used to obtain Δt_c^i. Bottom panel : critical time Δt_c beyond which the force time series become weakly correlated ($\Delta t_c < 0.15$) for the five portions of the wall, as a function of I_M. $<\Delta t_c>$ is the mean over the five Δt_c^i values of a simulation.

contacts. Near $I_M = 1.2\ 10^{-2}$ the mean autocorrelation time nearly vanishes, thus showing that the system is unable to keep memory of a past state. The granular medium, which is at the origin of the force transmission from the boundary conditions to the sidewall, handles here the signature of a remarkable cross- over from quasistatic to dense inertial regime. It is important to note that what we call the *memory of the system* is not an intrinsic memory of the granular material, but is rather system-dependent. This becomes obvious when those Δt_c^i (and $<\Delta t_c>$) are shown to be influenced by the length of the system, as it will be discussed in Sec. 4.6.

4.5 Force distributions

In the following, we analyze how the distributions of force time-series evolve with the boundary macroscopic inertial number, at macroscale (the entire wall ; Sec 4.5.1) as well as at mesoscale (portions of wall ; Sec 4.5.2) .

4.5.1 Force distributions on the entire obstacle

This section investigates the distribution of the total force experienced by the sidewall, on the whole surface facing the granular flow. This measurement gives information about the collective effect of the granular bulk on the obstacle. This analysis is crucial for real-world applications, while for instance designing civil engineering structures—in the case of main anchors that hold the whole obstacle, or for technical reasons when the installation of local force sensors is not possible (see a discussion in Sec. 4.7.3). The total force time-series F is obtained by summing all grain-wall contributions at each recording time. This force scaled by the mean force $\overline{F}$ is noted $\widetilde{F} = F/\overline{F}$, and its probability distribution density is computed.

The top panel of Fig.4.8 shows the distributions of $\widetilde{F}$, for seven values of I_M ranging from $1.2\ 10^{-3}$ to 0.6. The distribution shapes follow a nearly Gaussian law at low I_M ($= 1.2\ 10^{-3}$). A slight asymmetry appears while increasing I_M : the decreasing tail at high forces becomes more and more important. At the same time, from $I_M \geq 1.2\ 10^{-2}$, the probability to have weak or vanishing force signals on the sidewall increases. A systematic fit of the distributions—actually measured in DEM—using a shifted (and truncated) log-normal function, called $\mathcal{P}(\widetilde{F})$, provides very good results over the whole range of I_M tested, as depicted by the dashed lines on top of Fig. 4.8 :

$$\mathcal{P}(\widetilde{F}) = \frac{1}{\mathcal{S}} \frac{1}{\widetilde{F_\sigma}\sqrt{2\pi}(\widetilde{F}+1)} \exp\left(-\frac{[\ln(\widetilde{F}+1) - \widetilde{F_\mu}]^2}{2\widetilde{F_\sigma}^2}\right), \tag{4.12}$$

where $\widetilde{F_\mu}$ is the scale parameter, $\widetilde{F_\sigma}$ is the shape parameter, and the shift (truncation) is 1. $\mathcal{S}$ is the normalization factor corresponding to the value at 1 of the survival function of the

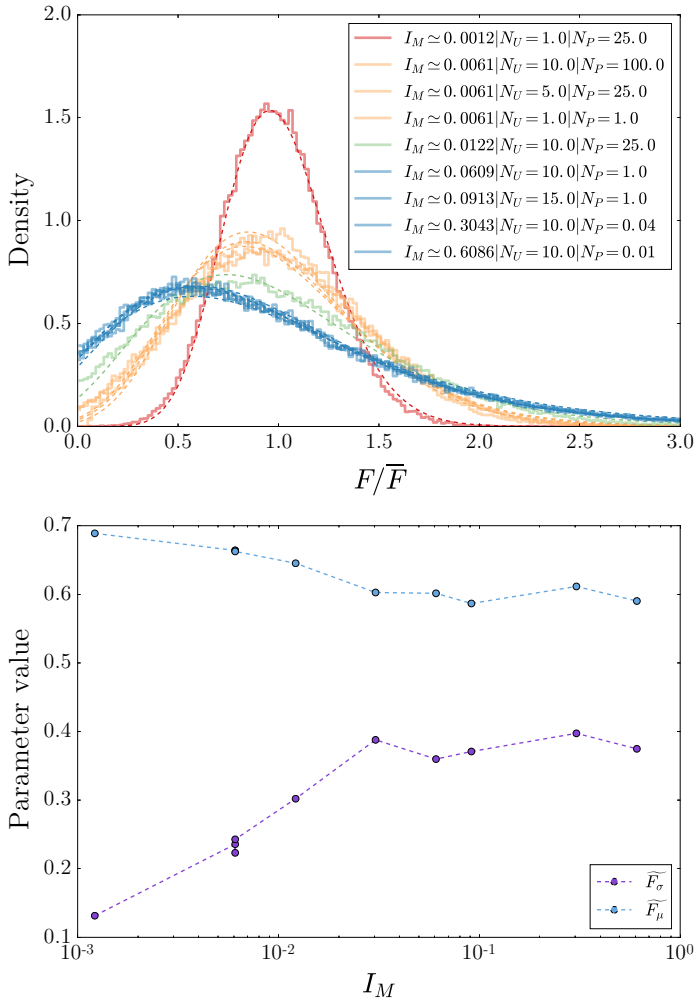

FIGURE 4.8 – Top panel : distribution of the total force on the right sidewall for seven values of I_M ranging from 1.2 10^{-3} to 0.6. The dashed lines show fits using a (truncated) log-normal PDF given by Eq. (4.12). Bottom panel : variation of f_μ and f_σ, the two parameters of Eq (4.12), as function of I_M.

(untruncated) log-normal PDF. The evolution of these parameters with I_M is displayed on the bottom panel of Fig.4.8.

Three distinct simulations, done for different macroscopic shear rates and confinement pressures $\{U, P\}$ but keeping the inertial number constant ($I_M = 6.1\ 10^{-3}$), give identical distributions, as shown in the top panel of Fig.4.8 (orange-colored curves). This reveals that the boundary macroscopic inertial number is the only parameter which controls the distribution of the total force on the wall. Such a key result is further confirmed by the two fitting parameters $\widetilde{F_\mu}$ and $\widetilde{F_\sigma}$, displayed at the bottom of Fig.4.8, that evolve monotonically with I_M—whatever $\{U, P\}$. It can be concluded that Eq. (4.12), fed with the parameters controlled by I_M (bottom of Fig.4.8), provides an empirical model capable of predicting the total force distribution for the granular flow-wall interaction system studied here.

Moreover, the DEM simulations show that all distributions of $\widetilde{F}$ collapse when $I_M \geq 6.1\ 10^{-2}$, as shown in the top of Fig.4.8 (blue curves). This observation becomes clearer in the bottom of Fig.4.8, as both $\widetilde{F_\mu}$ and $\widetilde{F_\sigma}$ reach a plateau from $I_M = 6.1\ 10^{-2}$ up to the highest value of the inertial number achieved in this study. This saturation of the total force distribution is likely to reflect a fast flow state largely influenced by inertial effects. It occurs above a certain value of I_M between $1.2\ 10^{-2}$ and $6.1\ 10^{-2}$, which closely matches the value of I_M at which the loss of system memory was identified in Sec. 4.4.

In order to analyse the distributions of the force at mesoscopic spatial scale, thus taking into account the potential heterogeneity over the system height, the next section tackles the distributions of force time-series recorded on portions of the obstacle height.

4.5.2 Force distributions on portions of the obstacle

In the same manner as in Sec. 4.4, the sidewall is split into five portions $i \in \{1, 2, 3, 4, 5\}$ of same height. We note F_i the force time-series associated with the portion i and $\overline{F_i}$ its mean. The upper panel of Fig.4.9 shows the distribution of $F_i/\overline{F_i}$, the force arising from each portion scaled by the corresponding mean, for $I_M = 6.1\ 10^{-2}$. The distributions of the force time-series from the three portions located in the center of the sidewall are equivalent (orange lines), unlike the two located at the top and bottom (red and blue lines, respectively). This difference between the portions $i \in \{2, 3, 4\}$ on the one side, and the portions $i = 1$ and $i = 5$ on the other side, is observed for any I_M (not shown here). This result reveals that the mesoscopic force distributions are homogeneous along a large area at the center—along the $y-$axis (vertical) direction—of the obstacle, whereas some modifications near the weak forces appear at the top and the bottom. In the bottom corner, at the interface with the bottom rough wall, few grains can be trapped and exert enduring forces on the obstacle, thus decreasing the probability of weak forces on the time-series. Near the top of the obstacle, the increasing probability of small forces can be explained by the shortening of the thickness of the dead zone, thus causing the obstacle

to experience directly the force of the flowing grains.

Because of the collapse of the distributions for portions $i \in \{2, 3, 4\}$ is observed for all values of I_M, the mean (called $<F_i/\overline{F_i}>_i$) of the distributions over these three central portions of the sidewall was computed, and its variation with the macroscopic inertial number was computed. The results are shown on the bottom panel of Fig.4.9. Similarly to the distributions on the entire height of the obstacle (see Sec. 4.5.1), the resulting curves depict log-normal-like shapes. Near $I_M \simeq 10^{-3}$, the distribution displays a small amount of low forces and a repartition which approaches a Gaussian-like shape. The number of weak forces increases with I_M, shifting the maximum probability density toward the low forces. This behaviour can be explained by a finite-size effect. At low inertial numbers the force signal may arise from the summation of several enduring contact forces, which is known to produce a Gaussian-like shape. By contrast, at higher inertial numbers the force signal arises from a lower number of contacts, thus increasing the probability of weak (or null) forces. Finally, all the force distributions on wall portions collapse for $I_M \geq 6.1\ 10^{-2}$. The latter observation reveals that—excluding the effects related to the top and bottom ends—the force distributions at mesoscale become independent of I_M as soon as a certain I_M is reached. This further confirms the result presented in Sec. 4.5.1 for the entire height of the obstacle, where the collapse of distributions was interpreted as a signature of the transition from quasistatic to dense inertial regime.

4.6 Effect of the system length

The results that have been presented up to now were extracted from simulations with a constant length of the system ($L/H = 5$ and $H = 30d$, where $d = 1$ mm). This section compares those results to additional ones from simulations where the length of the system was doubled ($L/H = 10$, while keeping $H = 30d$ and $d = 1$ mm).

The simulations at $L/H = 10$ did not allow to produce a plateau at high I_M around zero in the curves of V_y/U versus x/L (not shown here), the results being similar to the ones shown in Fig. 4.3. Doubling the length of the system did not allow to reduce the effect of the vortex-like structure (generated by the duplicate obstacle on the left side), which starts disturbing a lot the entire volume of the system for I_M larger than 0.3. This proves to be a signature of the transition toward the collisional regime, thus making questionable—beyond that $I_M \sim 0.3$—the analogy between the periodic system studied here and a free-surface gravity-driven granular flow passing over a rigid wall.

Figure 4.10 shows the scaled mean force, $\overline{F}/(Phd)$, as a function of I_M^* for $L/H = 5$ and $L/H = 10$. The empirical scaling given by Eq. (4.6) is slightly influenced by the ratio L/H. Doubling the length of the system yields a slight increase of the scaled mean force, but the empirical scaling that relates $\overline{F}/(Phd)$ to I_M^* is still robust, provided that r_1^* and

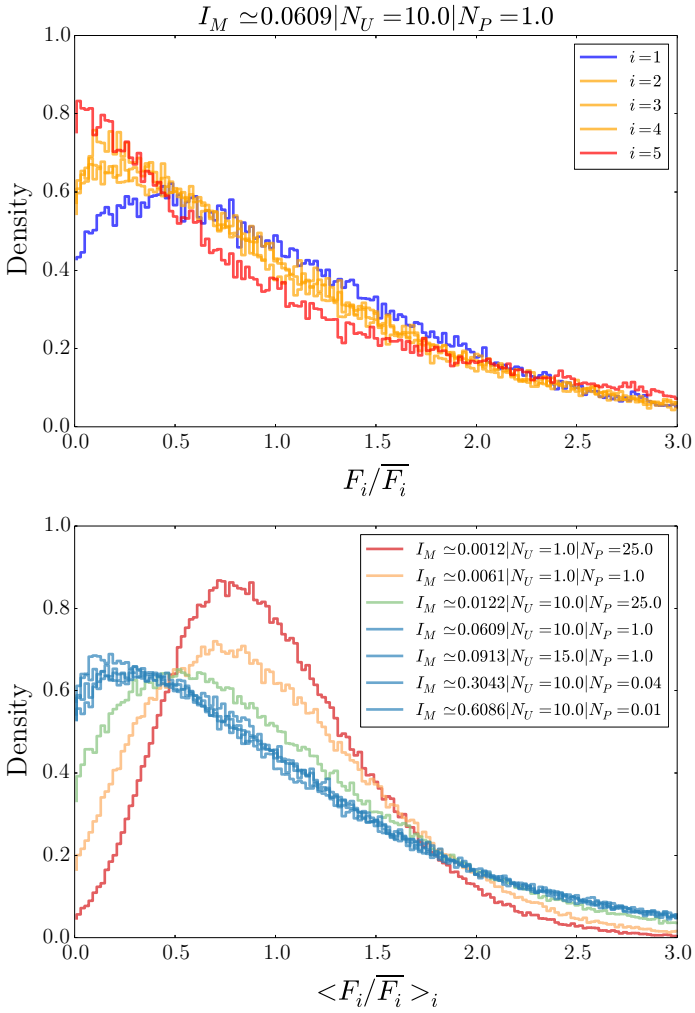

FIGURE 4.9 – Top panel : distribution of force time-series experienced by five equal portions i of the sidewall for $N_U = 10$ and $N_P = 1$ (each portion time-series is scaled by its corresponding time-averaged force). The blue, orange and red curves correspond respectively to $i = 1$, $i \in \{2, 3, 4\}$ and $i = 5$. Bottom panel : mean distribution over i for $i \in \{2, 3, 4\}$ (orange curves of top panel) for seven values of I_M.

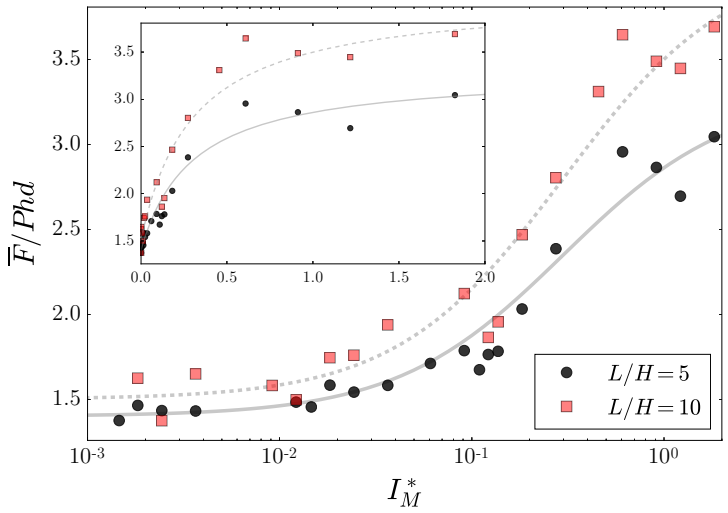

FIGURE 4.10 – Scaled mean force $\overline{F}/(Phd)$ versus I_M^* for $L/H = 5$ and $L/H = 10$. Although they are not discriminable in this plot, data from each L/H result from four values of h/d : 5, 10, 15 and 20. Grey solid line : same fit as in Sec. 4.3.2 ; grey dashed line : fit for $L/H = 10$, with $r_1^* = 1.5$, $r_2^* = 4.1$ and $I_M^{*0} = 0.3$.

r_2^*, in Eq. (4.6), become slightly dependent on L/H.

The top and bottom panels of Fig. 4.11 compare two extremes distributions of grain-wall forces at macroscale (entire height of the obstacle) and mesoscale (portions of obstacle) respectively, for $L/H = 5$ and $L/H = 10$. The distributions, besides at macroscale for very low I_M, are weakly influenced by the system length, and even totally independent on this parameter when the saturation occurs at intermediate to high I_M.

Overall, doubling the length of the system does small changes to the main results regarding the time-averaged dynamics and the distributions of grain-wall forces. However, moving from $L/H = 5$ to $L/H = 10$ has a significant effect on the variation of $<\Delta t_c>$ with I_M. As shown in Fig. 4.12, while $<\Delta t_c>$ is largely positive at small I_M for $L/H = 5$, it tends to approach zero for $L/H = 10$ at the same I_M. This put emphasis on the fact that the positive value of $<\Delta t_c>$ at small I_M can be interpreted as a signature of a memory activated by the system (*memory of the system*) in terms of the force transmission toward the wall, but not of a memory that would be intrinsic to the granular material itself.

4.7 Discussion and conclusion

The present paper described periodic numerical simulations based on DEM of a granular flow passing over a wall-like obstacle, over a wide range of confinement pressure and shearing velocity imposed at the top of the granular flow. The main results concerning the time-averaged dynamics and the force fluctuations are summarized and further discussed in this concluding section. We end the paper by exploring the potential implications of this

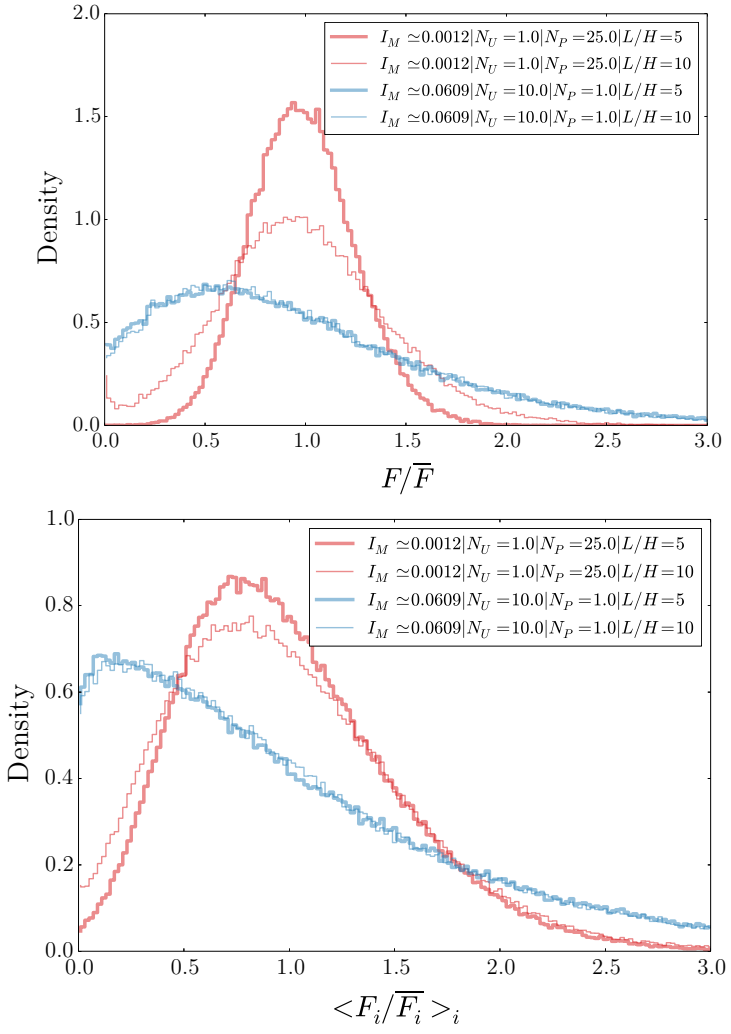

FIGURE 4.11 – Distributions of the total force on the entire height of the obstacle (top panel) and mean, over i for $i \in \{2, 3, 4\}$, of the distributions on portions of obstacle (bottom panel), for $L/H = 5$ (thick lines) and $L/H = 10$ (thin lines). In each panel, we present the results for $I_M = 1.2\,10^{-3}$ (the lowest I_M tested) and $I_M = 6.09\,10^{-2}$ (I_M beyond which the distributions collapse).

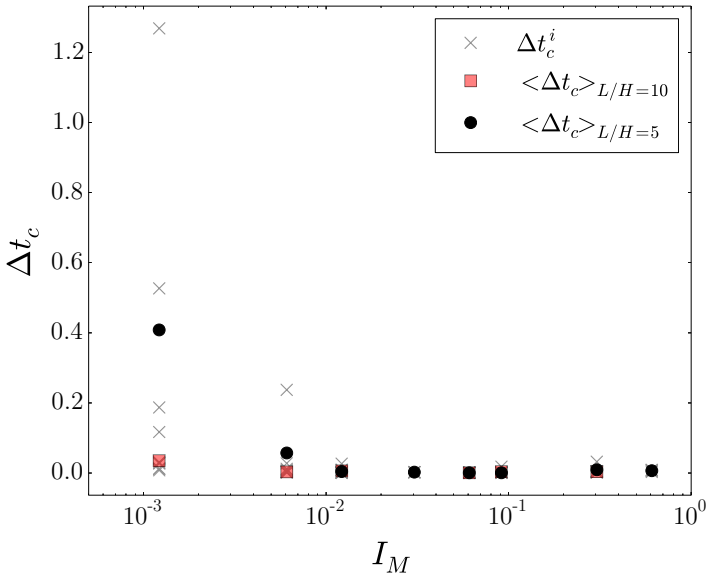

FIGURE 4.12 – Critical times Δt_c^i (and their mean $<\Delta t_c>$) beyond which the force time series become weakly correlated ($\Delta t_c < 0.15$), for $L/H = 5$ and $L/H = 10$.

basic knowledge for a real-world problem that is the interaction of full-scale granular flows in nature, such as avalanches, in interaction with civil engineering structures (Sec. 4.7.3).

4.7.1 Time-averaged dynamics

The mean force experienced by a wall (of height h) in contact with a dead zone subjected to a granular flow (of incoming height H) passing over the wall obeys the following scaling : $\overline{F} = f(I_M^*)Phd$, where I_M^* is a macroscopic inertial number built on the boundary confinement pressure P and the shearing velocity U over the height difference $H - h$, and f is a function which saturated at both low and high I_M^*. It was found that the bulk of the granular flow was controlled by the local $\mu(I)-$rheology, while the dead zone formed upstream of the wall was not. At very high I_M^*, the $\mu(I)-$rheology became, however, much less relevant. A vortex-like structure, inside which the local $\mu(I)-$rheology was not verified, formed downstream of the duplicate obstacle (on the left side of the periodic system simulated) and grew in size, thus producing a disturbance that propagated over the entire volume of the system. This was interpreted as the transition towards the collisional regime.

Figure 4.13 shows how the mean volume fraction Φ_* of the system, actually measured in the DEM simulations, varies with the macroscopic inertial number I_M^*. The curve has the typical shape of the $\Phi(I)-$constitutive law generally observed in a number of other systems, such as plane shear flows [29], inclined flows down a slope [41, 40], or annular shear cell flows [36]. Note that those curves result from simulations at different obstacle

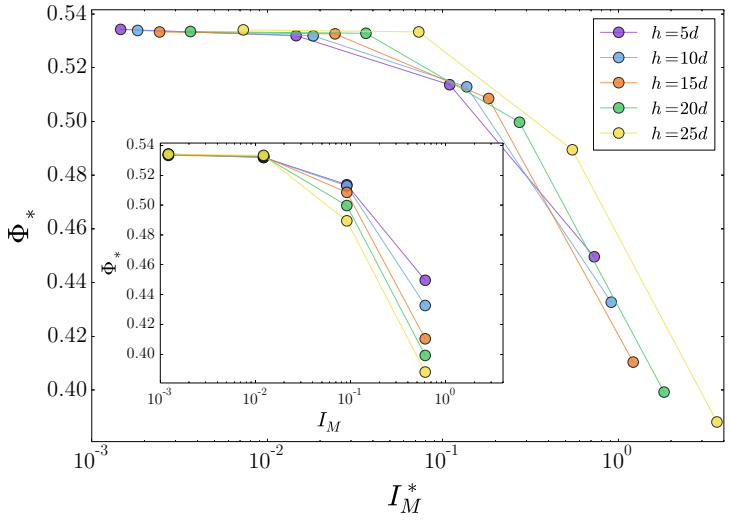

FIGURE 4.13 – Volume fraction Φ_* actually measured in the DEM simulations, as a function of I_M^*. Inset : Φ_* versus I_M.

heights. The inset of Fig. 4.13 that shows Φ_* versus I_M with a noticeable scattering at high I_M, further confirms that the inertial number I_M^* defined on the shearing height $H - h$ above the obstacle is the relevant parameter for this system (by contrast to the lid-driven cavity problem, as investigated in [58]). Note that the relation $\Phi_*(I_M^*)$ was found to be slightly dependent on L/H for very high I_M^* (not shown here).

4.7.2 Force fluctuations

In the present study, the analysis of the force fluctuations was performed through two main measurements. Firstly, the autocorrelations of force time series were computed at a spatial mesoscopic scale, intermediate between the grain size and the entire wall height (considering five portions of the wall, identical in size). Those temporal autocorrelations were found to be inhomogeneous through the wall height. A criterion based on the mean of an autocorrelation threshold through the wall height ($<\Delta t_c>$) was however able to reflect the system memory. Secondly, the distributions of force signals were computed at both macroscale (wall height) and mesoscale (considering the same portions of the wall as used for the autocorrelations). The boundary macroscopic inertial number I_M imparted to the granular system was found to be the control parameter of both types of measurements, thus highlighting remarkable trends that are summarized below.

For the lowest values of I_M tested, the system exhibited a significant memory, and narrowed distributions from normal-like to log-normal-like shapes—depending on the spatial scale considered—were observed. This result typically reflects the quasistatic flow regime : the wall experiences a constant and large number of enduring contacts with the grains. This increases the time needed for a force value to be forgotten by the system on the one

hand, and restricts the range of actual force values on the wall on the other hand.

While increasing I_M, the overall memory of the system decreased and the distributions widened. The inertial effect started to come into play, with faster motions of particles causing shorter contact times with the wall. In comparison with the quasistatic regime, the broadening of the statistical range of force values is thus interpreted as the consequence of (i) shorter and scarcer contacts with the wall near the weak force values on the one hand and (ii) more intense interactions near the highest forces on the other hand. The measurements of force fluctuations showed a saturation near $10^{-2} \leq I_M \leq 6\ 10^{-2}$, materialized by the collapse of force distributions and the vanishing of the system memory. In accordance with the well-established time-averaged dynamics of dense granular flows, as reviewed for instance in [41, 53], this saturation was interpreted as a clear signature of the transition from quasistatic to dense inertial regime.

4.7.3 Impact for a real-world application

The periodic immersed wall system studied in the present paper was motivated by the understanding of force fluctuations experienced by walls impacted by full-scale granular flows in nature, such as snow avalanches. Though the system is still a simplified model (planar and gravity-free in particular) of that geophysical problem, there are important outcomes regarding potential applications and perspectives.

First, the analysis of the mean dynamics of the system suggests that there exists a relatively wide range of flow regimes under which the mean force of a full-scale granular flow on a rigid wall of surface S_w should be controlled to first order by the confinement pressure ($\overline{F}/S_w \sim P$). However, the ratio of the impact pressure to the confinement pressure is not constant. It is controlled by the inertial number I_M^*, increasing from a value higher than 1 at low I_M^* up to a value around $3-4$ when I_M^* approaches unity. It is worthwhile to note that, in their simulations of a wall impacted by a free-surface granular flow down an incline (see [40]), Faug et al. found a ratio of the mean force on the wall to the pressure-dependent force of the incoming flow (associated to flow-depth) around 4 at similar inertial numbers close to unity, namely below a value for which velocity-square inertial force would become dominant. This suggests a strong analogy between the periodic immersed wall system studied here and the more complicated problem of a gravity-driven free-surface flow overflowing a wall, and shows that the value of $\overline{F}/S_w$ to P (namely $\overline{F}/(Phd)$ in the present study) appears to be robust.

Second, it is interesting to stress that the force distributions on the entire wall height were found to be much more narrow at low I^M*, thus indicating that slow flows can exert a relatively steady thrust on the wall (mainly centered over time on the mean value), while the wall immersed in a faster flow will experience highly time-varying levels of force. This robust result at the scale of the entire height of the wall put emphasis on two types

of force fluctuations in the pressure-dependent force regime. Any structure impacted by avalanches should be designed against both types of force fluctuations as a given avalanche track can produce either fast or slow dense flows, depending on the quality of the snow involved.

The present study paves the path for short-term research that will analyse, with the help of a similar approach, the force fluctuations for more complicated systems consisting of a rigid wall impacted by a gravity-driven free-surface avalanche-flow down an incline (as studied in [20] for the mean force). Finally, long-term research will tackle the problem of deformable walls impacted by granular flows.

Acknowledgments This work has been partially supported by the LabEx Tec21 (Investissements d'Avenir : grant agreement No. ANR11-LABX-0030). Thierry Faug and Mohamed Naaim are grateful to the financial support by the People Programme (Marie Curie Actions) of the EU 7th FP under REA Grant Agreement No. 622899 (FP7-PEOPLE-2013-IOF, GRAINPACT).

Chapitre 5

Conclusion

5.1 Contexte et méthode

Le risque naturel que représentent les avalanches de neige fait l'objet d'importantes recherches depuis quelques dizaines d'années. Afin de mieux dimensionner les structures de génie civil soumises à cet aléa, la compréhension de l'interaction complexe entre un milieu granulaire et un obstacle est nécessaire. À l'heure actuelle, des modèles avancés permettent de prévoir la force moyenne subie par un mur soumis à une avalanche. Cependant, les fluctuations de force de fréquence et d'amplitude élevées, systématiquement relevées sur l'obstacle, restent peu documentées. Ce travail de thèse s'intéresse au problème des fluctuations de force : il établit un cadre d'expérimentations adapté à leur étude, et fournit des éléments qui permettent de les caractériser en fonction des grandeurs macroscopiques qui gouvernent l'écoulement granulaire.

Les écoulements granulaires secs ont été mis en œuvre numériquement par la méthode des éléments discrets. Deux systèmes modèles ont été développés dans le but de focaliser la zone d'étude en amont de l'obstacle, et de permettre le contrôle des variables macroscopiques de l'écoulement (vitesse de cisaillement, pression de confinement, taille du système). Le premier a été l'objet des chapitres 2 et 3 : les grains sont confinés par quatre parois, dont l'une impose un cisaillement à vitesse constante. Les signaux de force ont été mesurés sur la paroi faisant face au cisaillement. Le chapitre 4 s'est focalise sur le second système : le cisaillement est toujours imposé par la différence de vitesse entre deux parois opposées, mais la condition aux limites périodique dans l'axe du cisaillement permet aux grains de surverser un unique mur immergé sur lequel sont réalisées les mesures. Chacun des systèmes a été dans un premier temps analysé par une approche moyennée dans le temps, puis les fluctuations ont été caractérisées à partir des signaux de force instantanés.

5.2 Synthèse des résultats

Un nombre conséquent de mesures a été effectué lors de l'étude des systèmes modèles ; elles visent à caractériser la dynamique moyenne ou les fluctuations lors de l'interaction du milieu granulaire avec l'obstacle.

— **Dynamique moyenne** : lignes de courant, profils de force aux parois, force moyenne sur l'obstacle, fraction volumique, tenseur des contraintes et taux de déformation locaux, nombre inertiel.

— **Fluctuations** : autocorrélation et distribution des signaux de force sur l'obstacle, à trois échelles spatiales différentes.

L'objet de cette partie est de synthétiser les résultats mentionnés précédemment dans les articles de cette thèse, en distinguant d'abord les deux systèmes. Une analyse comparative des deux systèmes est présentée par la suite, sous forme d'un article de conférence.

5.2.1 Cavité granulaire entraînée par cisaillement

Nombre inertiel I_M

Le nombre inertiel macroscopique $I_M \propto U/H\sqrt{P}$ unit les conditions aux bords régissant l'écoulement : vitesse de cisaillement U, pression de confinement P et hauteur du système H. Il s'est avéré fondamental dans la compréhension du système de cavité, en tant que variable de contrôle de la plupart des mesures. Il gouverne en particulier l'influence de l'inertie des grains sur la force moyenne ressentie par l'obstacle, mais également toutes les mesures caractérisant les fluctuations. De plus, la variation du nombre inertiel macroscopique a souvent révélé que les transitions de régimes d'écoulement ont des incidences marquées sur l'interaction avalanche–obstacle.

Dynamique moyenne

Une étude poussée de la dynamique moyenne du système a été menée dans un premier temps afin d'en comprendre les comportements vis-à-vis des conditions aux limites (pression de confinement, vitesse, taille).

L'étude des lignes de courant et des profils de forces aux parois pour la cavité ont révélé la complexité et l'hétérogénéité spatiale de la cavité. Un vortex unique se forme dans tout l'espace de la cavité, mettant en mouvement la grande majorité des grains. La position du centre de ce vortex sur l'axe horizontal dépend du régime d'écoulement : il est centré aux régimes quasistatiques et se rapproche de l'obstacle avec l'augmentation de I_M. Sur le mur faisant face au cisaillement, la force moyenne est répartie de façon non régulière : elle est quasiment nulle proche de la paroi inférieure, très élevée dans les couches supérieures, et à peu près homogène dans les couches intermédiaires.

La pression de confinement P et la longueur du système L gouvernent au premier ordre la force moyenne sur l'obstacle $\overline{F}$, mais une composante dépendante de la vitesse de cisaillement doit également être prise en compte pour une description totale. Une loi de saturation permettant de prédire $\overline{F}$ en fonction de I_M et de L a été établie, suggérant que $\overline{F}$ porte la signature de la loi rhéologique locale $\mu(I)$ des écoulements granulaires. Ce résultat a été confirmé par des mesures rhéologiques locales dans les écoulements, révélant que la loi rhéologique $\mu(I)$ est respectée quasiment partout dans le système. Les régions où cette loi n'est pas respectée correspondent principalement aux zones proches des murs verticaux et également à une fine bande horizontale centrée verticalement aux régimes lents. L'évolution de la fraction volumique macroscopique moyenne Φ_* avec I_M suit la même forme classique que les écoulements à volume libre, confirmant le rôle de la rhéologie $\mu(I)$ dans la force subie par l'obstacle.

Fluctuations

Les fluctuations de force sur le mur faisant face au cisaillement ont été étudiées via

l'utilisation d'outils statistiques à des échelles spatiales variables. L'autocorrélation des signaux de forces à l'échelle mésoscopique a mis en avant une propriété importante de la cavité : la fréquence liée à la rugosité de la paroi supérieure est directement observable, sauf dans les régimes très inertiels. Ce phénomène lié au blocage des grains dans le coin supérieur droit se transmet dans toute l'épaisseur du système jusqu'à la paroi inférieure aux régimes intermédiaires, alors qu'aux régimes lents elle n'est observable qu'en surface. La mesure de l'autocorrélation a également permis d'observer le phénomène de mémoire temporelle du système, existant pour les cisaillements à faible inertie mais disparaissant lors de la transition vers le régime dense inertiel.

L'investigation des distributions de forces sur l'obstacle est un élément majeur de la caractérisation des fluctuations. Quelle que soit l'échelle spatiale considérée, le nombre inertiel I_M s'est révélé être le paramètre de contrôle de ces mesures. Les distributions de forces évoluent entre des formes Gaussiennes aux régimes les plus lents et des formes exponentielles aux régimes les plus rapides. La transition entre ces deux types de densités de probabilités n'est pas triviale, mais les distributions ont pu être approchées numériquement par des fonctions log-normales tronquées dont les paramètres sont des fonctions monotones de I_M. En concordance avec la littérature, l'échelle spatiale de la mesure a également une influence sur les distributions. Il a donc été relevé que les échelles plus larges (macroscopique, à l'échelle de l'obstacle entier) ont tendance à resserrer les distributions, tandis qu'en diminuant l'échelle des mesures (jusqu'à l'échelle microscopique des grains), les distributions ont tendance à s'élargir.

5.2.2 Mur immergé dans un écoulement granulaire cisaillé

Nombre inertiel I_M

Ce système dispose d'une grandeur géométrique supplémentaire par rapport à la cavité : la hauteur du mur h. De ce fait, le nombre inertiel I_M a été complété par une définition correspondant au cisaillement des grains au droit de l'obstacle : $I_M^* \propto U/(H-h)\sqrt{P}$. La définition de I_M^* considère alors que tout le cisaillement au niveau de l'obstacle est concentré dans la région qui le surplombe $(H-h)$. Tandis que I_M s'est révélé être la grandeur de contrôle des fluctuations, l'introduction de I_M^* a été fondamentale dans la compréhension de la dynamique moyenne du système.

Dynamique moyenne

L'étude de la dynamique moyenne de ce système a permis de révéler sa réponse à la variation des conditions aux limites d'écoulement (pression de confinement, vitesse, longueur, hauteur de la paroi).

Les lignes de courant et les profils de vitesse verticale le long de l'axe horizontal fournissent un premier aperçu de la phénoménologie moyenne du système à mur immergé.

Dans les régimes lents à intermédiaires, des conditions proches du cisaillement simple sont observées dans la majeure partie du système. Lorsque l'inertie augmente, on constate cependant une recirculation locale dans la zone inférieure au point de réinjection des grains (partie gauche du système). Dans ce cas, une forte composante verticale de la vitesse perturbe la situation de cisaillement simple.

La hauteur de la paroi h et la pression de confinement P sont les variables qui entrent en jeu au premier ordre dans la force moyenne subie par l'obstacle $\overline{F}$. Cependant, la description précise de $\overline{F}$ nécessite d'intégrer une composante d'inertie de l'écoulement via I_M^*. Une loi de saturation permet de prédire $\overline{F}/Phd$ en fonction de I_M^*, suggérant la présence de la loi rhéologique locale $\mu(I)$ dans le système. Ce résultat est confirmé par les mesures locales de déformation et de contrainte ainsi que par le comportement de la fraction volumique Φ_* avec I_M^*. La loi $\mu(I)$ est respectée localement dans le système sauf au droit de l'obstacle pour les cisaillements lents et le comportement classique de Φ_* des écoulements à volume libre est vérifié.

Fluctuations

Les mêmes mesures statistiques que pour la cavité ont été utilisées pour le mur immergé. Le phénomène de mémoire temporelle du système a été observé via l'autocorrélation de signaux de forces à l'échelle mésoscopique. Les cisaillements à régimes faibles provoquent un effet de mémoire, signifiant qu'une valeur de force met un temps non négligeable à être "oubliée" par le système. En revanche, ce comportement disparaît totalement avec l'augmentation de l'inertie et le passage dans le régime d'écoulement dense inertiel.

À l'échelle macroscopique (intégration sur tout l'obstacle), le comportement des distributions de force évolue de façon univoque avec le nombre inertiel macroscopique I_M. Les formes sont Gaussiennes aux régimes lents et s'élargissent de manière asymétrique lorsque I_M augmente. Une saturation de cette évolution (superposition des distributions) est observée à partir d'une valeur de I_M proche de celle à laquelle la mémoire du système disparaît, traduisant la transition du régime quasistatique vers le régime dense inertiel. Les distributions ont pu être approchées par une loi empirique de forme log-normale tronquée dont les paramètres sont fonction de I_M. La réduction de la dimension spatiale d'intégration des mesures produit un effet sur les distributions qui est en accord avec la littérature. Ainsi, les distributions à l'échelle mésoscopique présentent des formes plus larges et moins symétriques qu'à l'échelle macroscopique, s'éloignant de la forme Gaussienne quel que soit le régime.

5.3 Analyse comparative

L'article de conférence figurant ci-après reprend les résultats clés de cette thèse, en proposant une analyse comparative des deux systèmes vis-à-vis du large panel de mesures effectuées.

Force fluctuations experienced by a boundary wall subjected to a granular flow in two distinct systems

Kneib F., Faug T., Dufour F., Naaim M.

Conference paper accepted for *Powder and Grains 2017*.

Abstract The present paper describes a numerical study of force fluctuations experienced by a boundary wall subjected to a granular flow on two distinct systems, namely a lid-driven cavity and an immersed wall system. Though the two systems exhibit different time-averaged dynamics, the force fluctuations experienced by the boundary wall show robust features in terms of the shapes of the probability density distributions and autocorrelation functions, under a wide range of boundary confinement pressure and shearing velocity imparted to the granular flow at the top of the system. This study identifies the key link between the grain-wall force fluctuations and the $\mu(I)-$rheology while moving from quasistatic to inertial regime.

5.3.1 Introduction

The problem of an assembly of grains in interaction with a boundary wall is relevant for a number of real-world applications involving granular materials, such as the transport of particle in food processing or mining industry, the impact of large-scale avalanche-flows with civil engineering structures in geophysics, the design of technological earthmoving equipments used to work with the soils in agriculture, etc. Understanding the force experienced by a boundary wall in interaction with a granular flow is crucial but little is known about the fluctuating part of the granular force under slow to fast flow regimes. The distributions of grain-grain or grain-wall contact forces (noted f) in static or quasistatic systems received a great attention, as reported in [4, 78] and a number of references therein. A salient feature in static granular media is a relatively robust exponential decrease at large forces, while the distributions at small forces may show very different behaviours (absence or presence of a plateau—even a peak, non-zero probability at $f = 0$), depending on many parameters associated with the shear history of the system. By contrast, only a few studies were devoted to force fluctuations at stake in flows of granular materials (see for instance [42]).

The present study investigates the distributions of grain-wall forces, as well as force time-series autocorrelation, when a granular flow interacts with a rigid boundary wall, under a wide range of macroscopic boundary shearing velocity U and confinement pressure P imparted to the granular bulk. The approach is based on the cross-comparison between two distinct granular flow systems simulated by discrete element method (DEM). The two

systems and their time-averaged dynamics are briefly described in section 5.3.2. Section 5.3.3 is devoted to the grain-wall force distributions on the entire height of the wall and on portions of wall. The analysis of force time-series autocorrelation is addressed in section 5.3.4. Finally, a conclusion is given in section 5.3.5.

5.3.2 Two distinct granular systems studied

Flow-wall geometries and methods

This section gives a brief summary of the two systems studied, both involving a boundary wall that is subjected to a planar and gravity-free granular flow. The first system, namely the granular *lid-driven cavity*, is a closed system for which the grains are forced to stay inside the cavity, thus producing a perpetual recirculation of the grains in the whole volume. The second system, namely the *immersed wall* granular system, is an opened system which enables the grains to escape by passing over an immersed wall, while other grains are trapped behind the wall-like obstacle. Both systems are simulated thanks to DEM, using the open-source YADE software [105].

The contact forces between the spherical particles of diameter d were modelled using a damped linear spring law for the normal direction and a linear spring with a static Coulomb threshold law for the tangential direction. Four microscopic parameters were required for the simulations presented here : the normal stiffness k_n, the tangential stiffness k_t, the interparticle friction coefficient μ and the normal restitution coefficient e. All simulations were conducted in the limit of rigid grains, varying k_n and k_t accordingly, with respect to the macroscopic pressure imparted by the top wall to the system. We considered $\mu = 0.5$ and $e = 0.5$. Full information on how the values of those parameters were implemented is given in our initial study of the lid-driven cavity system [58].

For both systems, we defined the two dimensionless following parameters : $N_U = U/\sqrt{gd}$ and $N_P = P/(\Phi\rho_P gH)$ where H is the height of the system (equal to $30d$ with $d = 1$ mm in the simulations presented here), and ρ_P was the particle density taken equal to 2500 kg m^{-3} (corresponding to the density of glass beads generally used in small-scale laboratory experiments). The systems lengths L were set to five times the height of grains : $L/H = 5$. A polydispersity of $\pm 15\%$ was given to the grains in order to avoid crystallization. Note that we considered typical pressures $\Phi\rho_P gH$ (where Φ was a typical volume fraction taken equal to 0.6 for a dense three-dimensional packing) and typical velocities $\sqrt{gd}$ in order to define N_P and N_U, though the systems simulated by DEM were gravity-free in the present study. This choice was made for convenience if laboratory experiments under gravity are developed in the future and compared to the DEM simulations presented in the paper. For both systems, N_U and N_P were typically varied in the ranges $[1; 20]$ and $[0.01; 100]$, respectively.

Based on the boundary conditions imposed at the top in terms of shearing velocity U

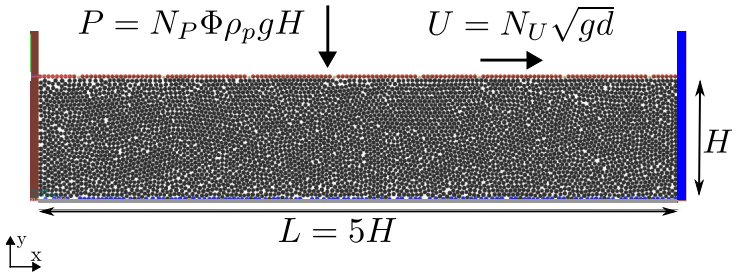

FIGURE 5.1 – Geometry and boundary conditions for the granular lid-driven cavity simulated by DEM

and confinement pressure P, a macroscopic inertial number can be defined as the ratio between the typical time $t_P = d\sqrt{\rho/P}$, associated with the top confinement pressure P, and the typical time $t_U = H/U$, equal to the inverse of the macroscopic shear rate over the height of the sample : $I_M = \frac{U}{H} d\sqrt{\rho/P}$.

The granular lid-driven cavity

The two-dimensional granular lid-driven cavity simulated by DEM consists of a planar assembly of spheres trapped into a box made of four walls, as sketched in Fig. 5.1. The perpetual recirculation of the grains within the cavity (closed system) produced streamlines showing the formation of a vortex in the whole volume of the cavity. The mean force on the right sidewall (see Fig. 5.1) was found to fit the empirical following scaling :

$$\overline{F} = \left(r + \frac{\Delta r}{1 + I_M^0 / I_M} \right) PLd, \tag{5.1}$$

where $r = 0.53$, $\Delta r = 0.33$ and $I_M^0 = 0.2$ in this study (see detail in [58, 59]). The values of r and Δr depend on the mechanical properties of the grains, for instance the interparticle friction, as reported in [59] where results from DEM simulations with $\mu = 0.27$ are presented too.

The immersed wall granular system

The immersed wall granular system consists of a horizontal flow of spheres passing over a wall of height $h = 20d$, as sketched in Fig. 5.2. This system was simulated by DEM using periodic conditions. The immersed wall-like obstacle led to the formation of a dead zone behind the wall, this dead zone co-existing with a sheared granular flow over it. As a result, the mean force on the wall was found to obey the empirical following relation :

$$\overline{F} = \left(r^* + \frac{\Delta r^*}{1 + I_M^{*0} / I_M^*} \right) Phd, \tag{5.2}$$

where $r^* = 1.4$, $\Delta r^* = 1.9$ and $I_M^{*0} = 0.3$ in the present study (see detail in [60]). The values of r^* and Δr^* depend on the mechanical properties of grains. I_M^* is the macroscopic

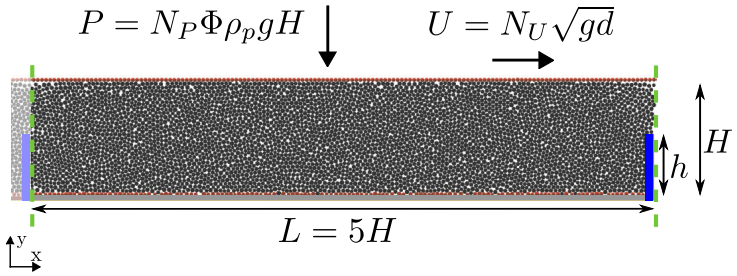

FIGURE 5.2 – Geometry and boundary conditions for the immersed wall granular system simulated by DEM. Periodic conditions were used, thus explaining the presence of a wall on the left side (lighter-colored area), which is a duplicate of the wall (of interest in our study) on the right side

inertial number defined with the difference between the height of the system (the height of grains) and the immersed wall height : $I_M^* = \frac{U}{H-h} d\sqrt{\rho/P}$.

Distinct time-averaged dynamics

Because the two systems presented above are by construction different, they show two different time-averaged dynamics. First, a standing vortex-like structure is formed inside the cavity volume [58, 59], while longitudinal streamlines with a curvature in the vicinity of the wall take place in the immersed wall system [60]. Second, the mean force scalings allowed us to identify different relevant spatial scales specific to each system. The relevant pressure force is PLd for the cavity (see Eq. (5.1)), while it is Phd for the immersed wall system (see Eq. (5.2)). The relevant spatial scale for the macroscopic inertial number is the system height H for the cavity (see Eq. (5.1)), while it is the height difference $H - h$, namely the height of the granular layer overflowing the wall, for the second system (see Eq. (5.2)). Much more details about the specific features of the lid-driven cavity and the immersed wall system can be found in [58, 59] and [60], respectively.

However, we show in the following how these two distinct systems exhibit very similar—not to say, for some aspects, identical—key features in terms of the force distributions and the force time-series autocorrelations on the boundary wall, and we will identify a robust signature of the transition from quasistatic to dense inertial granular flow regime.

5.3.3 Grain-wall force distributions

At the scale of the entire wall

Figure 5.3 shows the distributions of total force on the boundary wall for the lid-driven cavity (top panel) and the immersed wall system (bottom panel) for different values of I_M. First, it is worthwhile to note that the distributions are entirely controlled by the value of I_M, whatever the pair (U, P) (see the curves for $I_M = 6.1\ 10^{-3}$ obtained with

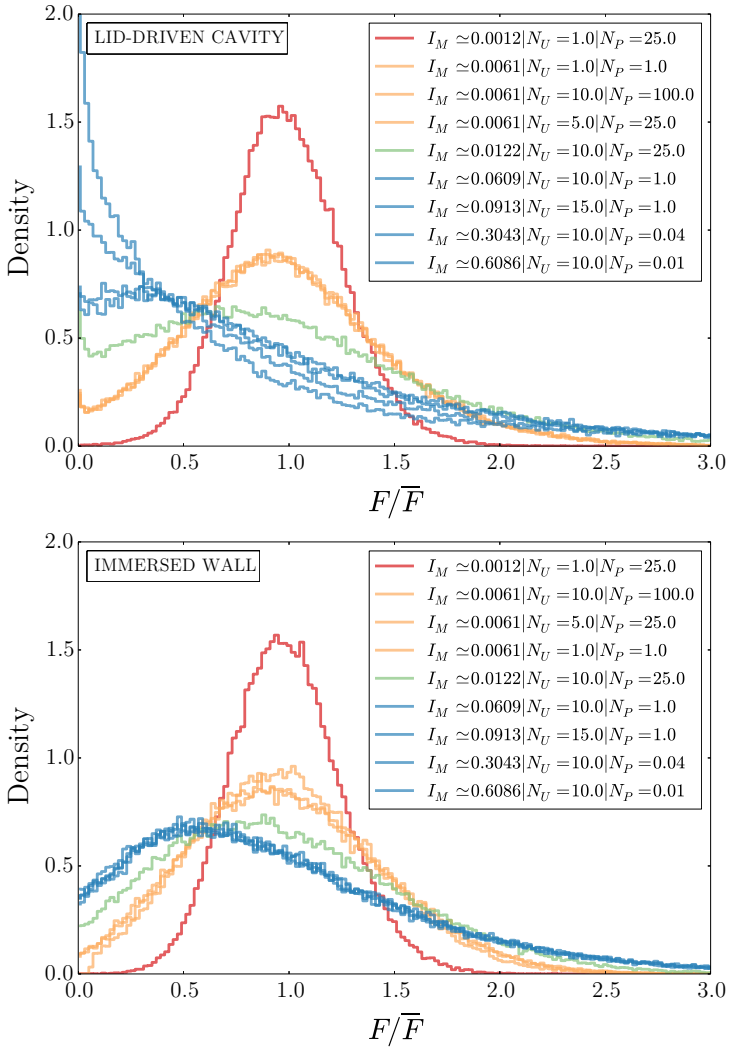

FIGURE 5.3 – Distributions of total force experienced by the boundary wall for the lid-driven cavity (top panel) and the immersed wall system (bottom panel), for different values of I_M

three different pairs (U, P) for the two systems). Second, it is found that they generally evolves from an exponential-like form at high forces (much larger than the mean) with the presence of a plateau/peak at small forces for high I_M, toward a Gaussian-like form at the lowest I_M. We observe a difference between the cavity and the immersed wall at the highest I_M : the cavity exhibit purely exponential shapes without any peak, while the peak at small forces is still present in the immersed wall system.

At the scale of a portion of wall

For both systems and a given I_M, our simulations showed that the distribution of the force F_i on each portion i of the boundary wall was independent of the vertical location along the boundary wall, excluding the extreme locations at the top and the foot of the wall (not shown here : details can be found in [59] for the cavity and [60] for the immersed

wall). As a result, we could average the distributions and extract robust mean values of distributions as functions of I_M, as depicted in Fig. 5.4. The top panel shows the results for the lid-driven cavity, while the bottom panel holds for the immersed wall system.

The force distributions shown in Fig. 5.4 collapse nicely into one single master curve, independent of I_M, once I_M becomes greater than 10^{-2}, whatever the granular system considered. This remarkable result, showing that there exists a threshold value of I_M which is independent of the system geometry, suggests that the distributions on portions of wall are robust to identify the transition between quasistatic and dense inertial granular flow regimes.

5.3.4 Force time-series autocorrelation

The autocorrelation function $\mathcal{C}(t, t + \Delta t)$ of force time-series on the wall was analysed for the cavity and the immersed wall system. It was generally observed that $\mathcal{C}(t, t + \Delta t)$ dropped quickly (exponentially) to zero over a time scale Δt_c and could fluctuate around zero (see details in [59, 60]). Note that very similar $\mathcal{C}(t, t + \Delta t)$ functions were extracted from an experimental study on the force experienced by an intruder dragged into a granular medium in an annular geometry [45].

Well-defined fluctuations associated with the transmission of the frequency U/d associated with the roughness of the wall at the top shearing the granular sample could sometimes be identified in the case of the cavity, as detailed in [59]. By contrast, this effect was never detected for the immersed wall. This observation illustrates the fact that the cavity can produce high confinement pressure on the right top corner (see [58] for much more discussion).

We could not find any clear relation between the critical time Δt_c beyond which the force time-series became weakly correlated, and the inertial number I_M, considering the entire height of the boundary wall subjected to the granular flow. However, by considering the autocorrelation function for portions of wall (as done for the distributions in section 5.3.3), we found that each ${\Delta t_c}^i$ (the critical time corresponding to a vertical location i along the boundary wall) had systematically a non-zero value for I_M below 10^{-2}, while it was nil beyond $I_M = 10^{-2}$. This result being robust whatever the system considered, we defined the critical time $\langle \Delta t_c \rangle$ averaged over all the locations i considered along the boundary wall. The latter is plotted in Fig. 5.5 as a function of I_M for the two granular systems. It is remarkable that both curves display very similar behaviours.

The autocorrelation function $\mathcal{C}(t, t + \Delta t)$ can be seen as a measure of the memory of the system through time Δt. High values of $\mathcal{C}$ indicate that a future state of the system (in terms of force applied to the wall) depends on the past state of this system, while it does not when $\mathcal{C}$ tends toward zero. As such, we can conclude from Fig. 5.5 that a future state of the system may strongly depend on the past state below $I_M \simeq 10^{-2}$ while it does

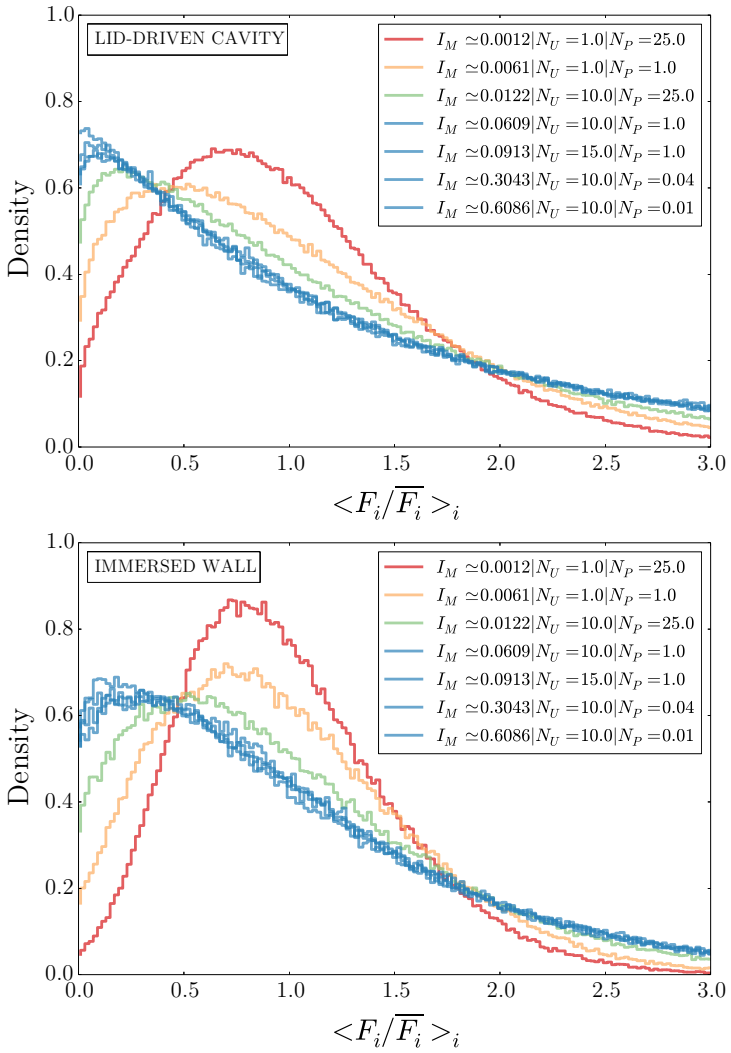

FIGURE 5.4 – Distributions of the force experienced by a portion of the boundary wall for the lid-driven cavity (top panel, H split into 10 portions) and the immersed wall system (bottom panel, h split into 5 portions). The curves drawn in both graphs correspond to the mean value obtained from all the vertical locations i along the wall, excluding the extreme locations at the top and the foot of the boundary wall

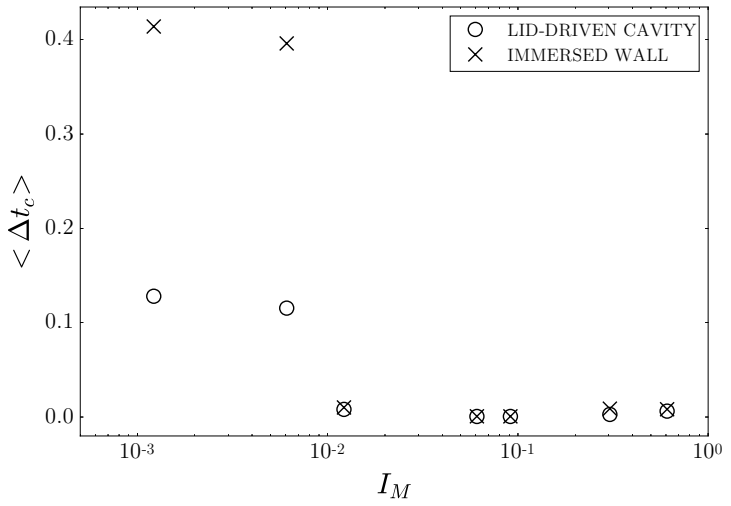

FIGURE 5.5 – Critical time $\langle \Delta t_c \rangle$ beyond which the force time-series become weakly correlated, as a function of I_M. We report the mean over the ${\Delta t_c}^i$ values for $i \in [1; 10]$ in the case of the lid-driven cavity (cross symbols) and for $i \in [1; 5]$ in the case of the immersed wall system (circle symbols)

not beyond this critical I_M. The latter result being robust whatever the granular system considered, this reveals another clear signature of the transition from the quasistatic regime (system with a memory) to the dense inertial regime (full loss of memory).

Note that the non-zero value of $\langle \Delta t_c \rangle$ below $I_M \simeq 10^{-2}$ is higher for the immersed wall than for the cavity. This difference may be explained by the fact that the grains against the boundary wall are moving along the cavity wall (perpetual recirculation), while they are not in the immersed wall system because they are trapped in the stagnant zone formed against the immersed wall. Therefore, memory effects may be more pronounced in the immersed wall system.

5.3.5 Conclusion

The present paper paid a particular attention to the force fluctuations experienced by the boundary wall, considering a wide range of macroscopic boundary conditions in terms of shearing velocity and confinement pressure imposed to each system. By comparing the results between the two distinct systems, we could extract some key features which appeared to be independent of the system at stake. In particular, our study showed that the distributions measured on portions of wall (of size around $3d$) moved from an exponential decrease at large forces with a shoulder at small forces, which were independent of I_M for I_M greater than 10^{-2}, toward I_M-dependent Gaussian-like distributions while I_M was decreased. Moreover, we could detect a system memory for the lowest I_M, which disappeared while increasing I_M beyond 10^{-2}. Those features were obtained from two distinct granular flow systems, characterized by a different time-averaged dynamics in terms of

streamlines and mean force scalings on the boundary wall. Those results then appear as a robust signature of the transition between quasistatic and dense inertial granular flow regimes, revealing and quantifying the link between the $\mu(I)-$rheology proposed by [52] and the force fluctuations experienced by a boundary wall.

Acknowledgments This work has been partially supported by the LabEx Tec21 (Investissements d'Avenir : grant agreement No. ANR11-LABX-0030). Thierry Faug and Mohamed Naaim acknowledge the financial support by the People Programme (Marie Curie Actions) of the EU 7th FP under REA Grant Agreement No. 622899 (FP7-PEOPLE-2013-IOF, GRAINPACT).

5.4 Discussions et perspectives

La comparaison des fluctuations de force au sein des deux configurations étudiées dans cette thèse a mis en valeur certains résultats communs, qui ne semblent donc pas dépendre du système étudié. Les comportements des distributions à l'échelle mésoscopique ($\simeq 3$ grains) sont similaires : elles sont de forme log-normales et dépendent de I_M aux régimes lents, alors qu'elles sont de forme quasi-exponentielles et indépendantes de I_M aux régimes rapides. Du régime quasistatique au régime dense inertiel, les distributions à l'échelle macroscopique (tout l'obstacle) sont très proches entre les deux systèmes. Enfin, l'effet mémoire des systèmes est présent au régime quasistatique, s'effaçant totalement lors de la transition vers le régime dense inertiel. L'ensemble de ces similitudes dans des systèmes où la dynamique moyenne est pourtant totalement différente, confirme l'importance de la loi rhéologique locale $\mu(I)$ dans les fluctuations de force sur un obstacle soumis à un écoulement granulaire (voir partie 1.1.2).

Un certain nombre de perspectives émergent alors, avec comme objectif d'appliquer les résultats de cette thèse à des systèmes se rapprochant progressivement de la situation réelle d'un obstacle surversé par un écoulement granulaire. Une description non exhaustive de ces perspectives est présentée ci-après.

Longueur des systèmes

Parmi les paramètres étudiés dans ce travail, la réponse des systèmes à la variation de la longueur L est particulièrement intéressante. La motivation première de l'utilisation de la cavité (LDC) par rapport à un système gravitaire a été la maîtrise de la zone d'influence de l'obstacle sur l'écoulement. Les résultats montrent bien dans ce cas que L, bien qu'intervenant par construction dans la force moyenne subie par l'obstacle, n'a pas d'influence sur les fluctuations de forces. L'introduction du système périodique à mur immergé (IW) modifie ce comportement car L a un effet sur la force moyenne comme sur les fluctuations : modification légère du comportement $\overline{F}/Phd = f(I_M^*)$ et des distributions ; modification radicale de l'effet mémoire. Dès lors, L apparaît comme une limite de ce système de laquelle il sera difficile de s'affranchir, tel que le montrent les lignes de courant dans la partie 4.2.

Il serait alors intéressant d'étudier la réponse d'un système qui ferait un pas de plus vers l'application finale, c'est-à-dire où l'écoulement des grains est induit par la gravité. On pourrait s'intéresser dans un premier temps aux fluctuations dans le régime permanent, en imaginant un débit de grains constant (condition périodique ou réservoir alimenté continuellement). Dans un second temps, le caractère transitoire des écoulements granulaires naturels (pic de force suivi d'un plateau puis d'une résiduelle, voir partie 1.1.3) pourrait être pris en compte en réalisant des lâchers de masses de grains en amont. Les résultats apportés par le présent travail seraient alors un bon point de comparaison. Le problème

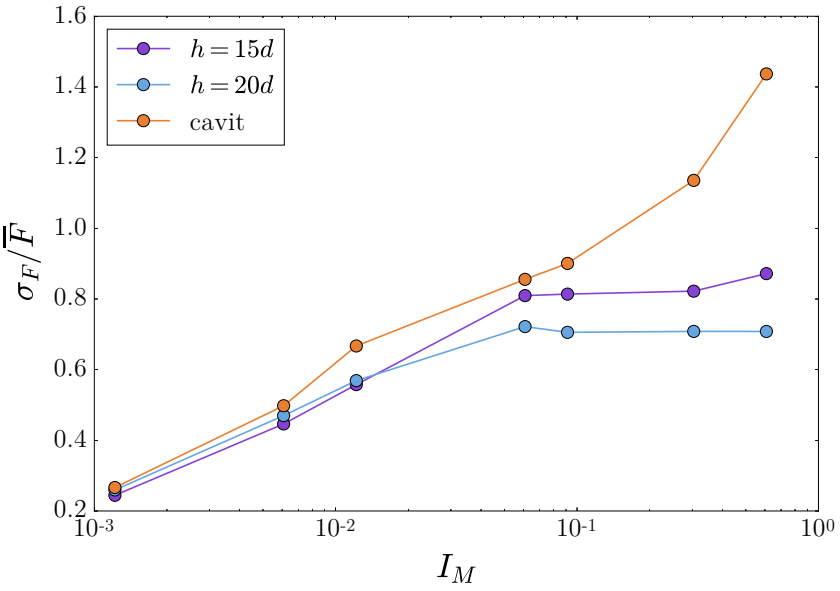

FIGURE 5.6 – Ratio de l'écart type des signaux de force σ_F aux forces moyennes $\overline{F}$ en fonction du nombre inertiel macroscopique I_M. Les résultats sont représentés pour la cavité ainsi que deux hauteurs de murs immergés.

de la non-maîtrise des grandeurs macroscopiques se poserait (et notamment la constitution d'un nombre inertiel macroscopique I_M), mais les outils amenés par cette thèse permettent de relever des grandeurs locales (dont le nombre inertiel local), et pourraient donc répondre à cette problématique.

Rapport entre fluctuations et force moyenne

Dans la démarche de prise en compte des fluctuations pour de meilleurs dimensionnements des structures de génie-civil, la mesure du rapport entre l'amplitude typique des fluctuations (l'écart type des signaux) et la valeur de la composante moyenne de la force est un élément essentiel. Ce coefficient de variation est tracé dans la figure 5.6 pour toute la gamme de régimes d'écoulements étudiée dans ce travail.

Aux régimes lents, l'amplitude des fluctuations représente 25% de la valeur moyenne de la force, et ce rapport augmente logarithmiquement avec le nombre inertiel. Aux régimes rapides, l'amplitude des fluctuations prend alors une forte importance, jusqu'à des rapports de l'ordre de 80% pour les murs immergés et 150% pour la cavité. Dans les régimes d'écoulements dense inertiel et collisionnel, les fluctuations jouent donc un rôle majeur dans la force sur l'obstacle, et sont par conséquent un ingrédient essentiel au dimensionnement des structures. En particulier, alors qu'une saturation du coefficient de variation est observée pour les murs immergés aux forts I_M, l'amplitude typique des fluctuations peut dépasser la valeur moyenne du signal pour les situations très confinées localement (cas de la cavité avec recirculation). Les fluctuations représentent alors la majeure partie de la

composante du signal et leur prise en compte dans les dimensionnements est primordiale.

Les modélisations réalisées dans cette thèse et les coefficient de variation présentés dans la figure 5.6 portent toutefois sur des écoulements plans. La généralisation à trois dimensions pour se rapprocher de la plupart des écoulements réels est discutée ci-après.

Dimensionnalité

Les écoulements in-situ sont de toute évidence en trois dimensions spatiales, et la réalisation d'expérimentations de laboratoire dans des conditions planes n'est pas aisée. Le passage des systèmes numériques plans décrits dans ce travail à des systèmes pleinement tridimensionnels est donc une évolution majeure à envisager pour permettre les ponts vers l'ingénierie. Dans ce cas, et si les effets de bords ne sont pas dominants, on peut s'attendre à des résultats moyens qualitativement semblables car ils sont lissés par nature. Les résultats concernant les fluctuations sont toutefois susceptibles d'être modifiés quantitativement voire qualitativement pour deux raisons :

— le nombre de grains en contact avec l'obstacle changerait drastiquement avec une influence sur les distributions ;

— les contraintes stériques inter-particules sont plus fortes en trois dimensions, augmentant le frottement effectif par phénomène de blocage et modifiant donc la rhéologie du milieu granulaire.

Il faudrait alors analyser l'influence du passage de 2 à 3 dimensions sur les résultats, et en particulier comment sont modifiées les relations posées par cette thèse entre les grandeurs macroscopiques moyennes et les fluctuations.

Géométrie et dynamique de l'obstacle

L'objet de cette thèse concerne l'étude de systèmes où l'obstacle est un mur dont la surface efficace fait face à l'écoulement. Dans les configurations étudiées, l'obstacle est un objet adjacent au fond fixe et rugueux exerçant un frottement basal à l'écoulement. Une zone morte de taille variable se forme alors naturellement à proximité du coin formé par l'intersection du fond et de l'obstacle. Les risques naturels mettant en jeu des écoulements granulaires concernent cependant des obstacles de toutes formes qui, en plus d'être surversés, sont potentiellement contournés par l'écoulement. L'étude d'obstacles de géométries différentes serait une évolution intéressante de cette thèse, s'appliquant par exemple aux cas de pylônes ancrés dans le sol ou à des ouvrages de déflexion des écoulements granulaires. Le système de mur présenté ici pourrait alors être modifié en immergeant des obstacles de formes diverses qui ne seraient pas en contact avec le fond, laissant passer les grains de part et d'autre. La comparaison des résultats avec ceux obtenus dans cette thèse pourrait mettre en relief le rôle joué par le blocage strict des grains dans le coin inférieur par rapport à des écoulements déviés par l'obstacle.

Dans ce travail, l'obstacle est considéré comme un élément fixe et parfaitement indéformable avec lequel les grains interagissent. Cependant, le passage à des problèmes in-situ implique l'utilisation de structures aux propriétés mécaniques qui leur sont propres. Il serait alors utile par la suite de modéliser l'obstacle en prenant en compte des comportements réalistes (modules d'élasticité, endommagement, modes de vibration ...), et d'analyser l'influence réciproque de l'obstacle avec le milieu granulaire. Dans cette optique, l'analyse de la rupture des structures en fonction des conditions d'écoulement est un point sensible particulièrement intéressant à étudier. Dans un premier temps, des obstacles plus réalistes pourraient intégrer les systèmes en régime permanent couverts par cette thèse pour étudier l'effet des fluctuations sur les vibrations mécaniques naturelles de l'obstacle. Des systèmes gravitaires pourraient être envisagés dans un second temps afin de prendre en compte le caractère transitoire des écoulements et l'effet successif des différentes phases des signaux de force (pic, plateau, résiduelle) sur la résistance de l'obstacle.

Bibliographie

[1] I. Albert, P. Tegzes, R. Albert, J.G. Sample, A.L. Barabasi, T. Vicsek, B. Kahng, and P. Schiffer. "Stick-slip fluctuations in granular drag". In: *Physical Review E* 64.3 (2001), p. 031307.

[2] R. Albert, M.A. Pfeifer, A.L. Barabasi, and P. Schiffer. "Slow drag in granular medium". In: *Physical Review Letters* 82.1 (1999), pp. 205–208.

[3] C. Ancey. "Dynamique des Avalanches". In: ed. by C. Ancey. Presses Polytechniques Universitaires Romandes – Cemagref Editions, Lausanne, Switzerland., 2006. Chap. Calcul des pressions.

[4] S. Joseph Antony. "Evolution of force distribution in three-dimensional granular media". In: *Phys. Rev. E* 63 (2000), p. 011302.

[5] D. Baroudi and E. Thibert. "An instrumented structure to measure avalanche impact pressure : Error analysis from Monte Carlo simulations". In: *Cold Regions Science and Technology* 59 (2009), pp. 242–250.

[6] P. Bartelt and B.W. McArdell. "Instruments and Methods : Granulometric investigations of snow avalanches". In: *Journal of Glaciology* 55.193 (2009), pp. 829–833.

[7] P. Berthet-Rambaud, A. Limam, D. Baroudi, E. Thibert, and J.M. Taillandier. "Characterization of avalanche loading on impacted structures : a new approach based on inverse analysis". In: *Journal of Glaciology* 54.185 (2008), pp. 324–332.

[8] R. Bharadwaj, R. Zenit, and C. Wassgren. "The unsteady drag force on a cylinder immersed in a dilute granular flow". In: *Physics of Fluids* 18 (2006), p. 043301.

[9] D. L. Blair, N. W. Mueggenburg, A. H. Marshall, H. M. Jaeger, and S. R. Nagel. "Force distributions in three-dimensional granular assemblies : Effects of packing order and interparticle friction". In: *Physical Review E* 63 (2001), p. 041304.

[10] Tamás Börzsönyi, Robert E. Ecke, and Jim N. McElwaine. "Patterns in Flowing Sand : Understanding the Physics of Granular Flow". In: *Phys. Rev. Lett.* 103 (2009), p. 178302.

[11] A. Bouchet, M. Naaim, F. Ousset, H. Bellot, and D. Cauvard. "Experimental determination of constitutive equations for dense and dry avalanches : presentation of the set-up and first results". In: *Surveys in Geophysics* 24 (2003), pp. 525–541.

[12] A. Bouchet, M. Naaim, H. Bellot, and F. Ousset. "Experimental study of dense snow avalanches : velocity profiles in quasi-permanent and fully-developed flows". In: *Annals of Glaciology* 38 (2004), pp. 30–34.

[13] J.F. Boudet and H. Kellay. "Drag Coefficient for a Circular Obstacle in a Quasi-Two-Dimensional Dilute Supersonic Granular Flow". In: *Physical Review Letters* 105 (2010), p. 104501.

[14] Mehdi Bouzid, Martin Trulsson, Philippe Claudin, Eric Clément, and Bruno Andreotti. "Nonlocal Rheology of Granular Flows across Yield Conditions". In: *Phys. Rev. Lett.* 111 (2013), p. 238301.

[15] T. A. Brzinski, P. Mayor, and D. J. Durian. "Depth-Dependent Resistance of Granular Media to Vertical Penetration". In: *Phys. Rev. Lett.* 111 (2013), p. 168002.

[16] Theodore A. Brzinski III and Douglas J. Durian. "Characterization of the drag force in an air-moderated granular bed". In: *Soft Matter* 6 (2010), pp. 3038–3043.

[17] V. Buchholtz and T. Pöschel. "Interaction of a granular stream with an obstacle". In: *Granular Matter* 1 (1998), pp. 33–41.

[18] Paolo Caccamo. "Etude expérimentale de l'influence des ouvrages de protection sur les avalanches et des pressions d'impact". PhD thesis. University of Grenoble, 2012.

[19] Emanuele Catalano, Bruno Chareyre, and Eric Barthélemy. "Pore-scale modeling of fluid-particles interaction and emerging poromechanical effects". In: *International Journal for Numerical and Analytical Methods in Geomechanics* 38.1 (2014), pp. 51–71.

[20] B. Chanut, T. Faug, and M. Naaim. "Time-varying force from dense granular avalanches on a wall". In: *Physical Review E* 82.4 (2010), p. 041302.

[21] Benoit Chanut. "Force exercée par une avalanche granulaire sur un obstacle. Application aux digues de protection paravalanche". PhD thesis. University of Grenoble, 2010.

[22] D. Chehata, R. Zenit, and C.R. Wassgren. "Dense granular flow around an immersed cylinder". In: *Physics of Fluids* 15.6 (2003), p. 1622.

[23] P. Claudin, J.-P. Bouchaud, M. E. Cates, and J. P. Wittmer. In: *Physical Review E* 57 (1998), p. 4441.

[24] S. N. Coppersmith, C. Liu, S. Majumdar, O. Narayan, and T. A. Witten. "Model for force fluctuations in bead packs". In: *Physical Review E* 53 (1996), p. 4673.

[25] Eric I. Corwin, Heinrich M. Jaeger, and Sidney R. Nagel. "Structural signature of jamming in granular media". In: *Nature* 435 (2005), pp. 1075–1078.

[26] Eric I. Corwin, Eric T. Hoke, Heinrich M. Jaeger, and Sidney R. Nagel. "Temporal force fluctuations measured by tracking individual particles in granular materials under shear". In: *Phys. Rev. E* 77 (2008), p. 061308.

[27] Frédéric da Cruz, Sacha Emam, Michaël Prochnow, Jean-Noël Roux, and François Chevoir. "Rheophysics of dense granular materials : Discrete simulation of plane shear flows". In: *Phys. Rev. E* 72 (2005), p. 021309.

[28] P.A. Cundall and O.D.L. Strack. "A discrete numerical model for granular assemblies". In: *Geotechnique* 29 (1979), pp. 47–65.

[29] F. da Cruz, S. Emam, M. Prochnow, J-N. Roux, and F. Chevoir. "Rheophysics of dense granular flows : discrete simulation of plane shear flows". In: *Physical Review E* 72 (2005), p. 021309.

[30] F. Dalton, F. Farrelly, A. Petri, L. Pietronero, L. Pitolli, and G. Pontuale. "Shear Stress Fluctuations in the Granular Liquid and Solid Phases". In: *Phys. Rev. Lett.* 95 (2005), p. 138001.

[31] J. D. Dent. "The dynamic friction characteristics of a rapidly sheared granular material applied to the motion of snow avalanches". In: *Annals of Glaciology* 18 (1993).

[32] J. D. Dent, K. J. Burrell, D. S. Schmidt, M. Y. Louge, E. E. Adams, and T. G. Jazbutis. "Density, velocity and friction measurements in a dry-snow avalanche". In: *Annals of Glaciology* 26 (1998), pp. 247–252.

[33] J. D. Dent and T. E. Lang. "Experiments on mechanics of flowing snow". In: *Cold Regions Science and Technology* 5 (1982), pp. 253–258.

[34] F. S. Edwards and V. D. Grinev. "Statistical mechanics of granular materials : stress propagation and distribution of contact forces". In: *Granular Matter* 4.4 (2003), pp. 147–153. ISSN: 1434-5021.

[35] J. Michael Erikson, Nathan W. Mueggenburg, Heinrich M. Jaeger, and Sidney R. Nagel. "Force distributions in three-dimensional compressible granular packs". In: *Phys. Rev. E* 66 (2002), p. 040301.

[36] A. Fall, G. Ovarlez, D. Hautemayou, C. Mézière, J.-N. Roux, and F. Chevoir. "Dry granular flows : Rheological measurements of the (I)-rheology". In: *Journal of Rheology* 59.4 (2015), pp. 1065–1080.

[37] T Faug. "Macroscopic force experienced by extended objects in granular flows over a very broad Froude-number range". In: *Eur. Phys. J. E* 38.5 (2015), p. 34.

[38] T. Faug, P. Caccamo, and B. Chanut. "A scaling law for impact force of a granular avalanche flowing past a wall". In: *Geophysical Research Letters* 39 (2012), p. L23401.

[39] T. Faug, P. Caccamo, and B. Chanut. "Equation for the force experienced by a wall overflowed by a granular avalanche : experimental verification". In: *Physical Review E* 84 (2011), p. 051301.

[40] T. Faug, R. Beguin, and B. Chanut. "Mean steady granular force on a wall overflowed by free-surface gravity-driven dense flows". In: *Physical Review E* 80.2 (2009), p. 021305.

[41] Y. Forterre and O. Pouliquen. "Flows of Dense Granular Media". In: *Annual Review of Fluid Mechanics* 40.1 (2008).

[42] Emily Gardel, E. Sitaridou, Kevin Facto, E. Keene, K. Hattam, Nalini Easwar, and Narayanan Menon. "Dynamical fluctuations in dense granular flows". In: *Philosophical Transactions of the Royal Society of London A : Mathematical, Physical and Engineering Sciences* 367.1909 (2009), pp. 5109–5121. ISSN: 1364-503X.

[43] Johan Gaume, Guillaume Chambon, and Mohamed Naaim. "Quasistatic to inertial transition in granular materials and the role of fluctuations". In: *Phys. Rev. E* 84 (2011), p. 051304.

[44] GDR-MiDi. "On dense granular flows". In: *European Physical Journal E* 14 (2004), pp. 341–365.

[45] J. Geng and R.P. Behringer. "Slow drag in two-dimensional granular media". In: *Physical Review E* 71.1 (2005), p. 011302.

[46] Isaac Goldhirsch. "Scales and kinetics of granular flows". In: *Chaos : An Interdisciplinary Journal of Nonlinear Science* 9.3 (1999), pp. 659–672.

[47] H. Gubler, M. Hiller, G. Klausseger, and U. Suter. *Messungen an Fliesslawinen.* Tech. rep. 41. EISLF Davos, Mitteilung, 1986.

[48] François Guillard, Yoël Forterre, and Olivier Pouliquen. "Depth-Independent Drag Force Induced by Stirring in Granular Media". In: *Phys. Rev. Lett.* 110 (2013), p. 138303.

[49] François Guillard, Yoël Forterre, and Olivier Pouliquen. "Origin of a depth-independent drag force induced by stirring in granular media". In: *Phys. Rev. E* 91 (2015), p. 022201.

[50] Daniel Howell, R. P. Behringer, and Christian Veje. "Stress Fluctuations in a 2D Granular Couette Experiment : A Continuous Transition". In: *Phys. Rev. Lett.* 82 (1999), pp. 5241–5244.

[51] J. T. Jenkins and M. W. Richman. "Kinetic theory for plane flows of a dense gas of identical, rough, inelastic, circular disks". In: *Physics of Fluids* 28.12 (1985), pp. 3485–3494.

[52] P. Jop, O. Pouliquen, and Y. Forterre. "A constitutive law for dense granular flows". In: *Nature* 441 (2006), pp. 727–730.

[53] Pierre Jop. "Rheological properties of dense granular flows". In: *Comptes Rendus Physique* 16.1 (2015). Granular physics / Physique des milieux granulaires, pp. 62 –72. ISSN: 1631-0705.

[54] Ken Kamrin and Georg Koval. "Nonlocal Constitutive Relation for Steady Granular Flow". In: *Phys. Rev. Lett.* 108 (2012), p. 178301.

[55] Hiroaki Katsuragi and Douglas J. Durian. "Unified force law for granular impact cratering". In: *Nature Physics* 3 (2007), pp. 420–423.

[56] M. Kern, P. Bartelt, B. Sovilla, and O. Buser. "Measured shear rates in large dry and wet snow avalanches". In: *Journal of Glaciology* 55.190 (2009), pp. 327–338.

[57] M. Kern., F. Tiefenbacher, and J.N. McElwaine. "The rheology of snow in large chute flows". In: *Cold Regions Science and Technology* 39 (2004), pp. 181–192.

[58] François Kneib, Thierry Faug, Frédéric Dufour, and Mohamed Naaim. "Numerical investigations of the force experienced by a wall subject to granular lid-driven flows : regimes and scaling of the mean force". In: *Computational Particle Mechanics* 3.3 (2016), pp. 293–302. ISSN: 2196-4386.

[59] François Kneib, Thierry Faug, Gilles Nicolet, Nicolas Eckert, Frédéric Dufour, and Mohamed Naaim. "Force fluctuations on a wall in interaction with a granular lid-driven cavity flow". In: *Phys. Rev. E* (Submitted).

[60] François Kneib, Thierry Faug, Frédéric Dufour, and Mohamed Naaim. "Mean force and fluctuations on a wall immersed in a sheared granular flow". In: *Phys. Rev. E* (Submitted).

[61] C. h. Liu, S. R. Nagel, D. A. Schecter, S. N. Coppersmith, S. Majumdar, O. Narayan, and T. A. Witten. "Force Fluctuations in Bead Packs". In: *Science* 269.5223 (1995), pp. 513–515. ISSN: 0036-8075. eprint: http://science.sciencemag.org/content/269/5223/513.full.pdf.

[62] Emily Longhi, Nalini Easwar, and Narayanan Menon. "Large Force Fluctuations in a Flowing Granular Medium". In: *Phys. Rev. Lett.* 89 (2002), p. 045501.

[63] Grunde Løvoll, Knut Jørgen Måløy, and Eirik G. Flekkøy. "Force measurements on static granular materials". In: *Phys. Rev. E* 60 (1999), pp. 5872–5878.

[64] Stefan Luding. "Cohesive, frictional powders : contact models for tension". English. In: *Granular Matter* 10.4 (2008), pp. 235–246. ISSN: 1434-5021.

[65] T. S. Majmudar and R. P. Behringer. "Contact force measurements and stress-induced anisotropy in granular materials". In: *Nature* 435 (2005), pp. 1079–1082.

[66] H. A. Makse, D. L. Johnson, and L. M. Schwartz. In: *Physical Review Letters* 84 (2000), p. 4160.

[67] Brian Miller, Corey O'Hern, and R. P. Behringer. "Stress Fluctuations for Continuously Sheared Granular Materials". In: *Phys. Rev. Lett.* 77 (1996), pp. 3110–3113.

[68] T. Miller, P. Rognon, B. Metzger, and I. Einav. "Eddy Viscosity in Dense Granular Flows". In: *Phys. Rev. Lett.* 111 (2013), p. 058002.

[69] Daniel M. Mueth, Heinrich M. Jaeger, and Sidney R. Nagel. "Force distribution in a granular medium". In: *Phys. Rev. E* 57 (1998), pp. 3164–3169.

[70] M. Naaim, F. Naaim-Bouvet, T. Faug, and A. Bouchet. "Dense snow avalanche modeling : flow, erosion, deposition and obstacle effects". In: *Cold Regions Science and Technology* 39.2-3 (2004), pp. 193–204.

[71] M. Naaim, T. Faug, and F. Naaim-Bouvet. "Dry granular flow modelling including erosion and deposition". In: *Surveys in Geophysics* 24 (2003), pp. 569–585.

[72] K. Nishimura and N. Maeno. "Contribution to viscous forces to avalanche dynamics". In: *Annals of Glaciology* 13 (1989), pp. 202–206.

[73] H. Norem, F. Irgens, and B. Schieldrop. "A continuum model for calculating snow avalanche velocities". In: *Avalanche Formation, Movement and Effects, Proceedings of the Davos Symposium, September 1986*. Vol. 162. IAHS Publ., 1987.

[74] H. Norem, F. Irgens, and B. Schieldrop. "Simulation of snow-avalanche flow in run-out zones". In: *Annals of Glaciology* 13 (1989), pp. 218–225.

[75] Corey S. O'Hern, Stephen A. Langer, Andrea J. Liu, and Sidney R. Nagel. "Force Distributions near Jamming and Glass Transitions". In: *Phys. Rev. Lett.* 86 (2001), pp. 111–114.

[76] A. Petri, A. Baldassarri, F. Dalton, G. Pontuale, L. Pietronero, and S. Zapperi. "Stochastic dynamics of a sheared granular medium". In: *The European Physical Journal B* 64.3 (2008), pp. 531–535. ISSN: 1434-6036.

[77] O. Pouliquen. "Scaling laws in granular flows down rough inclined planes". In: *Phys. Fluids* 11 (1999), pp. 542–548.

[78] Farhang Radjai. "Modeling force transmission in granular materials". In: *Comptes Rendus Physique* 16.1 (2015). Granular physics / Physique des milieux granulaires, pp. 3 –9. ISSN: 1631-0705.

[79] Farhang Radjai, Dietrich E. Wolf, Michel Jean, and Jean-Jacques Moreau. "Bimodal Character of Stress Transmission in Granular Packings". In: *Phys. Rev. Lett.* 80 (1998), pp. 61–64.

[80] Farhang Radjai, Stéphane Roux, and Jean Jacques Moreau. "Contact forces in a granular packing". In: *Chaos* 9.3 (1999), pp. 544–550.

[81] Farhang Radjai, Michel Jean, Jean-Jacques Moreau, and Stéphane Roux. "Force Distributions in Dense Two-Dimensional Granular Systems". In: *Phys. Rev. Lett.* 77 (1996), pp. 274–277.

[82] Pierre Rognon, Thomas Miller, and Itai Einav. "A circulation-based method for detecting vortices in granular materials". English. In: *Granular Matter* 17.2 (2015), pp. 177–188. ISSN: 1434-5021.

[83] P.J. Rognon, F. Chevoir, H. Bellot, F. Ousset, M. Naaim, and P. Coussot. "Rheology of dense snow flows : Inferences from steady state chute-flow experiments". In: *Journal of Rheology* 52 (2008), pp. 729–748.

[84] Jean-Noël Roux and Gaël Combe. "Quasistatic rheology and the origins of strain". In: *Comptes Rendus Physique* 3.2 (2002), pp. 131–140.

[85] B. Salm. "Flow, flow transition and runout distances of flowing avalanches". In: *Annals of Glaciology* 18 (1993).

[86] M. Schaeffer, T. Rösgen, and M. Kern. "High-speed video recording of basal shear layers in snow chute flows". In: *Cold Regions Science and Technology* 64.2 (2010), pp. 182–189.

[87] M. Schaer and D. Issler. "Particle densities, velocities and size distributions in large avalanches from impact-sensor measurements". In: *Annals of Glaciology* 32 (2001), pp. 321–327.

[88] Thomas Schwager and Thorsten Pöschel. "Coefficient of restitution and linear–dashpot model revisited". English. In: *Granular Matter* 9.6 (2007), pp. 465–469. ISSN: 1434-5021.

[89] A. Seguin, Y. Bertho, P. Gondret, and J. Crassous. "Dense Granular Flow around a Penetrating Object : Experiment and Hydrodynamic Model". In: *Phys. Rev. Lett.* 107 (2011), p. 048001.

[90] A. Seguin, Y. Bertho, F. Martinez, J. Crassous, and P. Gondret. "Experimental velocity fields and forces for a cylinder penetrating into a granular medium". In: *Phys. Rev. E* 87 (2013), p. 012201.

[91] PN Shankar and MD Deshpande. "Fluid mechanics in the driven cavity". English. In: *ANNUAL REVIEW OF FLUID MECHANICS* 32 (2000), 93–136. ISSN: 0066-4189.

[92] Leonardo E. Silbert, Deniz Erta ş, Gary S. Grest, Thomas C. Halsey, and Dov Levine. "Analogies between granular jamming and the liquid-glass transition". In: *Phys. Rev. E* 65 (2002), p. 051307.

[93] Abhinendra Singh, Vanessa Magnanimo, Kuniyasu Saitoh, and Stefan Luding. "Effect of cohesion on shear banding in quasistatic granular materials". In: *Phys. Rev. E* 90 (2014), p. 022202.

[94] Abhinendra Singh, Vanessa Magnanimo, Kuniyasu Saitoh, and Stefan Luding. "The role of gravity or pressure and contact stiffness in granular rheology". In: *New Journal of Physics* 17.4 (2015), p. 043028.

[95] Jacco H. Snoeijer, Martin van Hecke, Ellák Somfai, and Wim van Saarloos. "Force and weight distributions in granular media : Effects of contact geometry". In: *Phys. Rev. E* 67 (2003), p. 030302.

[96] Jacco H. Snoeijer, Thijs J. H. Vlugt, Martin van Hecke, and Wim van Saarloos. "Force Network Ensemble : A New Approach to Static Granular Matter". In: *Phys. Rev. Lett.* 92 (2004), p. 054302.

[97] R. Soller and S. A. Koehler. "Random fluctuations and oscillatory variations of drag forces on vanes rotating in granular beds". In: *EPL (Europhysics Letters)* 80.1 (2007), p. 14004.

[98] B. Sovilla, J.N. Mc Elwaine, M. Schaer, and Vallet J. "Variation of deposition depth with slope angle in snow avalanches : Measurements from Vallée de la Sionne". In: *Journal of Geophysical Research* 115 (2010), F02016.

[99] Yuka Takehara, Sachika Fujimoto, and Ko Okumura. "High-velocity drag friction in dense granular media". In: *EPL (Europhysics Letters)* 92.4 (2010), p. 44003.

[100] E. Thibert, D. Baroudi, A. Limam, and P. Berthet-Rambaud. "Avalanche impact on an instrumented structure". In: *Cold Regions Science and Technology* 54.3 (2008), pp. 206–215.

[101] C. Thornton. In: *KONA Powder and Particle 15* 15 (1997), p. 81.

[102] C. Thornton and S. J. Antony. In: *Philos. Trans. R. Soc. London, Ser. A* 356 (1998), p. 2763.

[103] F. Tiefenbacher and M. Kern. "Experimental devices to determine snow avalanche basal friction and velocity profiles". In: *Cold Regions Science and Technology* 38 (2004), pp. 17–30.

[104] Brian P. Tighe, Joshua E. S. Socolar, David G. Schaeffer, W. Garrett Mitchener, and Mark L. Huber. "Force distributions in a triangular lattice of rigid bars". In: *Phys. Rev. E* 72 (2005), p. 031306.

[105] V. Šmilauer, A. Gladky, J. Kozicki, C. Modenese, and J. Stránskỳ. "Yade Using and Programming". In: *Yade Documentation*. Ed. by V. Šmilauer. 1st. http ://yade-dem.org/doc/. The Yade Project, 2010.

[106] C.R. Wassgren, J.A. Cordova, R. Zenit, and A. Karion. "Dilute granular flow around an immersed cylinder". In: *Physics of Fluids* 15.11 (2003), p. 3318.

[107] Thomas Weinhart, Remco Hartkamp, Anthony R. Thornton, and Stefan Luding. "Coarse-grained local and objective continuum description of three-dimensional granular flows down an inclined surface". In: *Physics of Fluids* 25.7, 070605 (2013), p. 070605.

[108] K. Wieghardt. "Experiments in granular flow". In: *Annual Review of Fluid Mechanics* 7 (1975), pp. 89–114.